

**Verification of Real-time Hybrid Simulation
with Shake Table Tests for a Three Story Structure
Equipped with MR Damper**

Ali I. Ozdagli, Wang Xi, Ge Ou, Shirley J. Dyke, Jian Zhang, and Bin Wu

Report IISL – 006, August 2014



VERIFICATION OF REAL-TIME HYBRID
SIMULATION WITH SHAKE TABLE TESTS
FOR A THREE STORY STRUCTURE
EQUIPPED WITH MR DAMPER

Ali I Ozdagli¹, Wang Xi², Ge Ou¹,
Dr. Shirley J Dyke¹, Dr. Jian Zhang², and Dr. Bin Wu³

¹Purdue University

²University of California at Los Angeles

³Harbin Institute of Technology

IISL Report Series-06



This document is compiled with L^AT_EX 2_ε using MiK_TE_X's distro
and T_EXStudio editor on January 22, 2015.

Source is available at bitbucket.org/aliirmak/report-repo/.

Acknowledgments

This report contains project results conducted under the China-US Collaboration Research Project. The work herein is supported in part by the U.S. National Science Foundation under Grant CMMI-1011534 (NEESR), the National Natural Science Foundation of China under Grant-90715036 and Purdue International Programs under the Sohmen Fund.

Firstly, the authors want to acknowledge invaluable help of Bo Li, Dr. Yong Ding, Dr. Guoshan Xu and laboratory personal of Harbin Institute of Technology. Without their help, this project would not have happened. The authors are also grateful for the help of Dr. Hui Li at Harbin Institute of Technology in allowing the use of structural specimen for the experiments. Authors appreciate help of Christian Eduardo Silva, a fellow student of IISL in designing the loading frame for RTHS. Finally, authors want to thank to Dr. Tao Wang at Institute of Engineering Mechanics of China for his part and support in solidifying US-China academic collaboration and this research project.

Abstract

In the last few decades, Real-time hybrid simulation (RTHS) has become a recognized testing methodology for evaluating performance of structural components under potentially catastrophic events such as earthquakes. Although RTHS is cost- and time-effective compared to other existing test methods such as shake table or pseudo-dynamic testing, it is a relatively new concept. Accordingly, there is a pressing need to assure growing interest from civil engineering community seeking for validation of RTHS. To meet community's expectations, a comprehensive verification of the RTHS methodology is needed. This work presented herein is the summary of an international multi-university collaboration research project. Efforts toward demonstrating reliability and feasibility of RTHS are focused on three phases: (i) analytical simulations, (ii) physical full-scale tests and (iii) RTHS of a three story prototype structure equipped with a controllable MR damper under various earthquake inputs. Integrity of numerical models and performance of RTHS are evaluated through the comparisons with shake table tests to verify RTHS.

Contents

Acknowledgments	i
Abstract	ii
Contents	v
List of Figures	ix
List of Tables	x
1 INTRODUCTION	1
1.1 Literature Review	5
1.1.1 Linear Applications	5
1.1.2 Nonlinear Applications	7
1.1.3 Remaining Challenges	9
1.2 Objective and Scope	11
1.3 Overview	12
2 EXPERIMENTAL SETUP FOR SHAKE TABLE AND RTHS TESTS	14
2.1 HIT Test Structure	15
2.2 System Identification Test Equipment	18
2.3 Shake Table Test Configuration	20
2.3.1 Shake Table	21
2.3.2 Test Equipment	23
2.3.3 Ground Excitation	27
2.4 Loading Frame at HIT	29
2.4.1 Test Equipment	30
2.5 Real-time Hybrid Simulation Setup at Purdue	31
2.5.1 Test Equipment	31
2.6 Summary	34

3	MODELING, SYSTEM IDENTIFICATION AND MODEL UP-DATING OF THE TEST STRUCTURE	36
3.1	Baseline Model	37
3.2	System Identification	41
3.2.1	Procedure	41
3.2.2	Application	45
3.3	Model Updating	53
3.4	Limitations of the Proposed Method	56
3.5	Evaluation Criteria	57
3.6	Results	58
3.6.1	Initial Model	58
3.6.2	System Identification: Identified Parameters	60
3.6.3	Comparison of Model Updating Methods	66
3.6.4	Model Verification	67
3.7	Conclusion	73
4	MAGNETO-RHEOLOGICAL DAMPER CHARACTERIZATION AND SEMI-ACTIVE VIBRATION CONTROL DESIGN	74
4.1	Introduction	75
4.2	Damper Identification and Modeling	78
4.2.1	Modeling of the MR Damper	78
4.2.2	Identification Process	81
4.2.3	Damper Characterization Results	82
4.3	Semi-active Control Algorithm	85
4.3.1	Implementation of Clipped-optimal Control Algorithm	87
4.3.2	Implementation of H_2/LQG Control	88
4.4	Summary	91
5	VERIFICATION OF SHAKE TABLE TESTS WITH ANALYTICAL SIMULATIONS	92
5.1	Design of MR Damper Controllers	93
5.2	Post-processing of Data	94
5.2.1	Time Windowing	94
5.2.2	Filtering	94
5.2.3	Frequency-Domain Calculations	96
5.3	Comparison of Shake Table Test Responses with Pure Simulation Results	97
5.3.1	El Centro	98
5.3.2	Kobe	102
5.3.3	Morgan Hill	105
5.3.4	Discussions	126
5.4	Conclusions	128

6	VERIFICATION OF RTHS WITH SHAKE TABLE TESTS	130
6.1	Design of Tracking Controller to Compensate Actuator Dynamics	131
6.1.1	Modeling of Servo-hydraulic Actuator	132
6.1.2	Control Scheme for Actuator Tracking	136
6.1.3	Verification of Controller	138
6.2	RTHS Implementation	138
6.3	Comparison of Shake Table Test Responses with RTHS Results .	142
6.3.1	El Centro	142
6.3.2	Kobe	143
6.3.3	Morgan Hill	149
6.3.4	Discussions	170
6.4	Conclusions	172
7	CONCLUSIONS	173
	Bibliography	175

List of Figures

1.1	Literature Review on RTHS	6
1.2	Schematic of Validation Scenarios	12
2.1	Original experimental structure	16
2.2	Additional details for modified test structure	17
2.3	NI USB-6259	18
2.4	DeweSoft Start-up screen	19
2.5	Bröel & Kjør model #4368 with its Base Magnet	20
2.6	Jiangsu Lianneng made Impact Hammer	20
2.7	Sinocera Signal Conditioners	21
2.8	Shake table located at HIT	22
2.9	250 kN capacity Schenck Actuator	22
2.10	MTS FlexTest GT Controller	23
2.11	TestSuite Multipurpose Software Layout	23
2.12	Dong-Hua Universal Dynamic Signal Test System	24
2.13	dSpace DS1104 System Terminal Board	25
2.14	dSpace ControlDesk Software Layout	25
2.15	Ke Dong KD 5018 Signal Conditioner	26
2.16	Keyence Laser Displacement Sensor and Controller	27
2.17	#DA-50 LVDT	27
2.18	MR Damper Amplifier	28
2.19	MTS Load Cell	28
2.20	MR Damper Fixture	29
2.21	El Centro Earthquake Comparison	30
2.22	Kobe Earthquake Comparison	31
2.23	Morgan Hill Earthquake Comparison	32
2.24	MTS Loading Frame with MR damper and Load Cell attached at HIT	33
2.25	Shore Western Actuator, MR Damper and Load Cell attached to Loading Frame	34
2.26	Shore Western SC6000 Controller	34
2.27	Speedgoat Performance Real-time Target Machine	35

3.1	Lumped mass model idealization of the test structure	38
3.2	Effect of Eq. (3.16a) on the complex mode shapes	45
3.3	Impact Data Parser Script Workflow	48
3.4	Tapered boxcar window	50
3.5	An Idealization of a Linear System in Time Domain	52
3.6	Block Diagram of the Structure to be Identified	60
3.7	Sensor and Hit Location Layout	61
3.8	Transfer Function Comparison between Experimental Data vs ERA Data	63
3.9	Phase Diagram Comparison between Experimental Data vs ERA Data	64
3.10	Identified Mode Shapes of the First Three Identified Modes . . .	65
3.11	Transfer Function Comparison between Experimental Data and Updated Models	68
3.12	El Centro Earthquake Comparison	70
3.13	Kobe Earthquake Comparison	71
3.14	Morgan Hill Earthquake Comparison	72
4.1	Particulate Alignment in MR fluid	77
4.2	MR Damper Internals	78
4.3	MR Damper Models	79
4.4	Phenomenological Bouc-Wen Hysteresis Model of the MR Damper	80
4.5	HIT MR Damper Experimental Data for 0 V and 1.7 V Constant Voltage Levels	83
4.6	Comparisons for HIT MR Damper Experimental Data vs Identif- ied Model	84
4.7	Comparisons for HIT vs Purdue Dampers	86
4.8	An Idealization of Structural Control with MR Damper	88
5.1	Application of Time Windowing to First Floor Displacement Re- sponse for Morgan Hill Semi-Active Control Case	95
5.2	Effect of Butterworth Filtering to Third Floor Acceleration Re- sponse for Morgan Hill Semi-Active Control Case	96
5.3	A Representative Simulink Model of the Analytical Simulation .	98
5.4	El Centro Earthquake Comparison in Time Domain for POFF Case	100
5.5	El Centro Earthquake Comparison in Frequency Domain for POFF Case	101
5.6	Moving RMS Error for El Centro Earthquake POFF Case	102
5.7	El Centro Earthquake Comparison in Time Domain for PON Case	103
5.8	El Centro Earthquake Comparison in Frequency Domain for PON Case	104
5.9	Moving RMS Error for El Centro Earthquake PON Case	105
5.10	El Centro Earthquake Comparison in Time Domain for SA Case	106
5.11	El Centro Earthquake Comparison in Frequency Domain for SA Case	107
5.12	Moving RMS Error for El Centro Earthquake SA Case	108

5.13	Kobe Earthquake Comparison in Time Domain for POFF Case . . .	109
5.14	Kobe Earthquake Comparison in Frequency Domain for POFF Case	110
5.15	Moving RMS Error for Kobe Earthquake POFF Case	111
5.16	Kobe Earthquake Comparison in Time Domain for PON Case . . .	112
5.17	Kobe Earthquake Comparison in Frequency Domain for PON Case	113
5.18	Moving RMS Error for Kobe Earthquake PON Case	114
5.19	Kobe Earthquake Comparison in Time Domain for SA Case . . .	115
5.20	Kobe Earthquake Comparison in Frequency Domain for SA Case	116
5.21	Moving RMS Error for Kobe Earthquake SA Case	117
5.22	Morgan Hill Earthquake Comparison in Time Domain for POFF Case	118
5.23	Morgan Hill Earthquake Comparison in Frequency Domain for POFF Case	119
5.24	Moving RMS Error for Morgan Hill Earthquake POFF Case . . .	120
5.25	Morgan Hill Earthquake Comparison in Time Domain for PON Case	121
5.26	Morgan Hill Earthquake Comparison in Frequency Domain for PON Case	122
5.27	Moving RMS Error for Morgan Hill Earthquake PON Case . . .	123
5.28	Morgan Hill Earthquake Comparison in Time Domain for SA Case	124
5.29	Morgan Hill Earthquake Comparison in Frequency Domain for SA Case	125
5.30	Moving RMS Error for Morgan Hill Earthquake POFF Case . . .	126
6.1	Servo-Hydraulic System Diagram	132
6.2	Introduction of Outer Loop Control	132
6.3	Open Loop System Input and Output in Time Domain for HIT Setup	133
6.4	Frequency Response and Identified Model of the Open Loop Sys- tem for HIT Setup	134
6.5	Open Loop System Input and Output in Time Domain for Purdue Setup	135
6.6	Frequency Response and Identified Model of the Open Loop Sys- tem for Purdue Setup	136
6.7	RIAC Control Block Diagram	137
6.8	Performance of RIAC for HIT Actuator	139
6.9	Performance of RIAC for Purdue Actuator	140
6.10	Communication between Physical and Analytical Substructure in a RTHS Frame	140
6.11	A Representative Simulink Model of the RTHS Simulation	141
6.12	El Centro Earthquake Comparison in Time Domain for POFF Case	144
6.13	El Centro Earthquake Comparison in Frequency Domain for POFF Case	145
6.14	Moving RMS Error for El Centro Earthquake POFF Case	146
6.15	El Centro Earthquake Comparison in Time Domain for PON Case	147

6.16	El Centro Earthquake Comparison in Frequency Domain for PON Case	148
6.17	Moving RMS Error for El Centro Earthquake PON Case	149
6.18	El Centro Earthquake Comparison in Time Domain for SA Case	150
6.19	El Centro Earthquake Comparison in Frequency Domain for SA Case	151
6.20	Moving RMS Error for El Centro Earthquake SA Case	152
6.21	Kobe Earthquake Comparison in Time Domain for POFF Case	153
6.22	Kobe Earthquake Comparison in Frequency Domain for POFF Case	154
6.23	Moving RMS Error for Kobe Earthquake POFF Case	155
6.24	Kobe Earthquake Comparison in Time Domain for PON Case	156
6.25	Kobe Earthquake Comparison in Frequency Domain for PON Case	157
6.26	Moving RMS Error for Kobe Earthquake PON Case	158
6.27	Kobe Earthquake Comparison in Time Domain for SA Case	159
6.28	Kobe Earthquake Comparison in Frequency Domain for SA Case	160
6.29	Moving RMS Error for Kobe Earthquake SA Case	161
6.30	Morgan Hill Earthquake Comparison in Time Domain for POFF Case	162
6.31	Morgan Hill Earthquake Comparison in Frequency Domain for POFF Case	163
6.32	Moving RMS Error for Morgan Hill Earthquake POFF Case	164
6.33	Morgan Hill Earthquake Comparison in Time Domain for PON Case	165
6.34	Morgan Hill Earthquake Comparison in Frequency Domain for PON Case	166
6.35	Moving RMS Error for Morgan Hill Earthquake PON Case	167
6.36	Morgan Hill Earthquake Comparison in Time Domain for SA Case	168
6.37	Morgan Hill Earthquake Comparison in Frequency Domain for SA Case	169
6.38	Moving RMS Error for Morgan Hill Earthquake POFF Case	170

List of Tables

2.1	Section Properties of the Prototype Structure	15
3.1	List of Evaluation Criteria	59
3.2	Evaluation Criteria for Model Verification	73
4.1	Identified Bouc-Wen Model Parameters	85
5.1	Evaluation Criteria for Pure Simulation Verification	127
6.1	Evaluation Criteria for RTHS Verification	171

CHAPTER 1

INTRODUCTION

Designing civil engineering structures that can withstand the test of time has always been a major challenge. As a part of this challenge, the earthquake engineers have aimed to create redundant environments resisting destructive forces of nature such as unforgiving earthquakes, harsh winds and giant tsunamis. However, the Great Sichuan Earthquake that occurred at 14:28 CST on May, 12 2008 tried the traditional structural engineering practices once more. Despite of all engineering efforts, the toll of the earthquake was 69,226 deaths and a direct economic cost of 124.2 billion US Dollars ([United Nations Centre for Regional Development, 2009](#)). The overly large amount of damage in recent events such as this earthquake demonstrated that current practices are not sufficient. Innovation is needed in civil engineering to overcome our limitations. In the last two decades, structural vibration control systems have received growing attention in the civil engineering community. To date, many varieties of control devices including passive, active and semi-active types have been developed. The Great East Japan Earthquake occurred in 2011 demonstrated that such devices provided effective damage control ([Taylor et al., 2012](#)).

Among vibration control devices currently available on the market, the MR damper is known for its reliability and adaptability. Principally, MR dampers provide a novel and attractive semi-active control mechanism. By using small amount of external power source, system's stiffness and damping characteristics can be modified based on the feedback of structural responses and the supplemental MR damper can consume the motion of the structure to develop necessary restoring forces. Many experimental studies have already demonstrated the effectiveness of the MR damper in mitigating earthquake hazards for various structural configurations. For example, [Dyke et al. \(1996b\)](#) and [Jiang and Christenson \(2011\)](#) demonstrated that MR dampers can reduce structural responses in small-scale models. [Friedman \(2012\)](#) showed that large scale MR dampers are very effective in controlling structural vibrations. As a different approach, [Ramallo et al. \(2002\)](#) integrated an MR damper to a base isolation system to increase efficiency of passive base isolators. Finally, [Lynch et al. \(2008\)](#) studied structural control in a wireless sensor network setting using a MR damper device.

When it comes to understanding the effects of vibration control devices on the global performance on the structures, RTHS technique is often used, in particular, for evaluating performance of rate dependent devices such as base isolation systems ([Erkus and Johnson, 2006](#)), MR dampers ([Christenson et al., 2008](#)) or nonlinear elastomeric dampers ([Chen et al., 2009](#)). Because RTHS provides an efficient way to isolate and physically test only the more complex or critical components when available resources do not allow researchers to test the full-scale structure, the RTHS technique has become a significant research area in earthquake engineering in recent years. Numerous studies have verified effectiveness of RTHS by comparing hybrid test results to numerical simulations of semi-actively controlled structures equipped with MR damper ([Christenson et al., 2008](#); [Carrion et al., 2009](#); [Castaneda et al., 2013](#); [Gao et al., 2013b](#))

Although RTHS is cost- and time-effective compared to other existing test methods such as shake table or pseudo-dynamic testing, it is a relatively new concept. With the expectation that RTHS will become more standard and acceptable in the future, there is a pressing need to demonstrate and validate the RTHS method ([Dyke et al., 2010](#)).

To this date, little research has been reported on the comparison of RTHS results with those from a large scale structure tested on the shake table. [Lin \(2009\)](#) demonstrated that there is a close correlation between responses in shake table tests of a small scale 3-DOF shear building model with an MR damper, and responses in the real-time hybrid simulation where the MR damper is the only physical substructure. However the results also show discrepancies due to actuator dynamics and modeling errors.

A more recent study conducted by [Shao and Enyart \(2012\)](#) investigated the feasibility the real-time hybrid simulation methodology by comparing a full small-scale 3-DOF shear building model on shake table with pure analytical simulation and RTHS tests where third story of the structure being as only the physical substructure. In both configurations, the third floor was also equipped with a viscous damper designed for radio controlled toy cars to add nonlinearity to the system. Several imperfections in the comparisons were reported, that are related to limited displacement tracking performance of the actuator driving the shake table. The researchers also noticed that when measured shake table accelerations were used for the pure simulations and RTHS, the discrepancies became larger.

Finally, an up-to-date study researched by [Saouma et al. \(2014\)](#) focused on validating RTHS using a nonductile reinforced concrete frame tested on a shake table. For RTHS, this three story structure is modeled with nonlinear elements and over 400 degrees of freedoms, while one of its base columns is

tested physically. Overall, the test is another major step in validating RTHS, however the comparisons between shake table and RTHS responses also indicate discrepancies.

Even though comparisons between experimental tests, analytical simulations and RTHS tests have validated the results to some extent, we are aware of no research considering large-scaled structures with larger damper forces. In addition, the accuracy of the comparisons is based on the tracking performance of the actuator in RTHS scheme. However, there is no research conducted on how performance of same-family controllers are affected by different actuator configurations. To advance these research areas, an international multi-university collaboration research project has been proposed which focuses on the following tasks: (i) identification and modeling of the test structure, (ii) development of control algorithms for efficient vibration control, (iii) testing of the structure on the shake table, (iv) development of tracking algorithms to compensate dynamics of different actuator, (v) conducting RTHS tests where MR damper is integrated to the platform as physical substructure and (vi) verification of the RTHS method by comparing the results.

The aforementioned tasks are partitioned into three large phases. In the first phase of this study, system identification tests of the medium-scale prototype test structure built at Harbin Institute of Technology (HIT) in China are discussed and several numerical models are proposed. Preliminary semi-active control designs are developed based on the numerical model. Also, the behavior of MR dampers used at HIT for the shake table tests and at Purdue for the RTHS are characterized and numerical models have been generated.

In the second phase of this study, the structure is excited on the shake table located at HIT under various earthquake inputs when damper is on and off the structure. Subsequently, using the proposed numerical models of the structure

and the MR damper, the preliminary performance achieved with various control algorithms is compared under several earthquake excitations.

Finally, in the last phase, H-inf based tracking algorithm, RIAC is developed for the large-slow and small-fast actuators located at HIT and Purdue, respectively. After the performance and reliability of this algorithm is evaluated, responses from RTHS conducted at Purdue using the analytical model as the numerical substructure and the MR damper as the physical substructure are compared to the shake tables test results.

1.1 Literature Review

To date, only a few researchers have investigated the validation of RTHS using different structures and configurations. The validation efforts are categorized in two groups: (1) linear applications and (2) nonlinear applications. A summary of the previous research is tabulated in Fig. 1.1. This section will summarize these research efforts.

1.1.1 Linear Applications

The first validation of RTHS for a linear structure was performed by [Wang et al. \(2011\)](#), where a two story shear frame was tested at Tsinghua University. Since the final goal of this research was to investigate soil-structure interaction using RTHS, validation was not the ultimate focus. For the preliminary RTHS configuration, the reference structure was partitioned into two substructures: (i) second floor as physical structure, i.e. the substructure on the shake table and (ii) first floor as the numerical substructure. Acceleration responses to 2 and 3 Hz sine wave excitation at roof level were compared between RTHS, shake table and numerical analysis schemes. No further analysis were conducted on the quality of the data for the verification of RTHS.

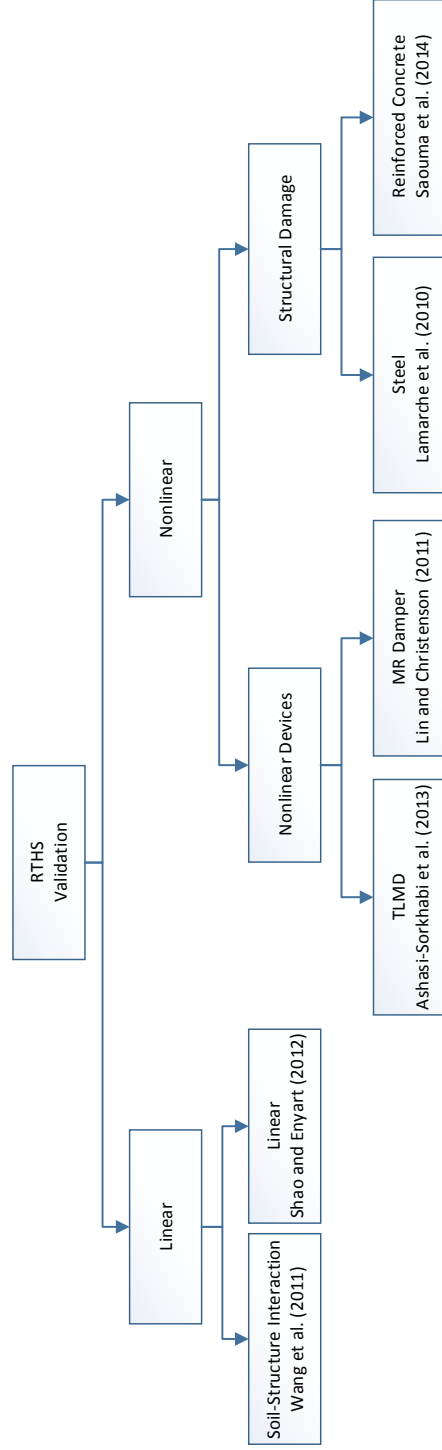


Figure 1.1: Literature Review on RTHS

A setup similar to the previous study was proposed by [Shao and Enyart \(2012\)](#). In this study, the development of the RTHS framework at Western Michigan University is described. To demonstrate the feasibility of the framework, responses of a three story benchmark structure tested on the shake table is compared to those of the proposed substructuring configuration for linear cases. According to the comparisons, response of RTHS scheme matches pure numerical simulation and shake table results for the 1940 El Centro earthquake motion. A maximum peak-to-peak error by about 20% is reported for this comparison. Nevertheless, the results show that RTHS can be used to obtain reasonable seismic responses of the testing structure.

1.1.2 Nonlinear Applications

Validation of RTHS for nonlinear seismic applications is first explored by [Lin and Christenson \(2009, 2011\)](#) and [Lin \(2009\)](#). The aim of this study series was to compare shake table responses of a two story structure, controlled with an MR damper attached between ground floor and its first floor, with corresponding RTHS results in the RTHS facility at the University of Connecticut. For the shake table tests, the physical two story structure was excited with various ground accelerations. For RTHS tests, the MR damper was isolated and tested as the physical substructure, where the two story structure was modeled as the numerical substructure. The mass of the structure was estimated to be 100 kg and the MR damper fixture on the structure was designed to sustain forces up to 500 N. Thus, damper was always utilized at passive-off control mode where a constant 0 A was sent to the current driver feeding the damper. Reported root mean square (RMS) acceleration error between the shake table test and RTHS varied from 1% to 30%, while peak accelerations differed between 4-18% for various earthquakes.

One additional validation of RTHS using a nonlinear device was conducted by [Ashasi-Sorkhabi et al. \(2013\)](#). This particular study investigated the dynamic performance of a single degree of freedom (SDOF) system with a tuned liquid damper (TLD) using RTHS and shake table testing techniques. The RTHS setup partitioned the system into TLD as the physical substructure due to its complex and difficult-to-model nonlinear nature and linear SDOF structure as the numerical substructure. Although good agreement was observed between the responses from the real-time hybrid simulation and shake table tests, the comparison can be roughly reduced to tracking of the desired displacement. The error indicator was given in terms of phase error index (PEI) and amplitude error index (AEI). These indicators promise versatility in understanding RTHS configuration performance, albeit they are not commonly used.

Another comparison study was performed for a two story structure by [Lamarche et al. \(2010\)](#), both in linear and nonlinear regimes. The RTHS configuration comprises the first story as the physical substructure, whereas the rest of the structure was simulated with a nonlinear numerical model using Rosenbrock integration method. RTHS, shake table and numerical analysis results were examined to demonstrate proposed RTHS and compensation methods can estimate responses of the test structure. Three linear and five non-linear cases were analyzed. For some nonlinear cases, yielding of steel in tension and buckling in compression was considered, by introducing additional structural members. For all of the comparisons, errors were reported similar to the work of [Lin and Christenson \(2011\)](#). This study is unique since it is one of the first projects that was able to run complex nonlinear structural models and also to estimate strain hardening of steel with Giuffré-Menegotto–Pinto hysteresis model in RTHS configuration.

Finally, [Saouma et al. \(2014\)](#) investigated a three story, three bay reinforced

concrete structure that was tested previously by [Ghannoum and Moehle \(2012\)](#) on a shake table. To conduct RTHS, the structure is partitioned into one of the base columns as the physical substructure, and rest of the structure as the numerical substructure. Since the shake table test focused on axial failure of the columns, gravity as well as lateral forces were simulated using three actuators in RTHS. The numerical substructure consisting over 400 degrees of freedom is modeled using nonlinear elements. The model computation was performed using Mercury, a hard and soft real-time simulation program developed by [Kang \(2010\)](#). Due to high nonlinearity in the elements and large number of DOFs, the nonlinear solution algorithm was only able to run at 50 Hz. For the actuator command displacement tracking, a simple PID control is used. However, to minimize instability due to time lag between the measurement and the command furthermore, α coefficient is adjusted in the numerical integrator, to a modified version of α - Operator Splitting Method with constrained iteration number. Another action taken to improve tracking was increasing the damping corresponding to rotational DOF of the beam adjacent to the physically tested column. A peak error of about 27 % has been reported for the comparisons. Considering the fact that the specimen was tested to the failure and Mercury, as most of the integrators do, was not able to converge correctly, hence, the error margin is acceptable. Other issues such as low sampling rate and poor optimization of numerical substructure may contribute to the error, as indicated by the authors.

1.1.3 Remaining Challenges

Although results of the comparisons obtained from linear and nonlinear experiments are encouraging, there are several challenges that need to be addressed here. Only a few of the previous efforts in the literature investigate medium and

full scale structures. Most of the test structures addressed to previous reported research are constrained to maximum values of 100 kg in mass and three meters in height (Wang et al., 2011; Shao and Enyart, 2012; Lin and Christenson, 2011; Ashasi-Sorkhabi et al., 2013).

The exceptions to the aforementioned physical limitation are the studies conducted by Lamarche et al. (2010) and Saouma et al. (2014). Both studies focus on large scale structures made of nonlinear materials such as either non-rate dependent steel (Lamarche et al., 2010) or rate dependent reinforced concrete Saouma et al. (2014). Numerical models developed to explain basic nonlinear steel behavior is well documented and can be simulated effectively to estimate shake table responses without integration of RTHS. On the other hand, RTHS can be utilized as a viable option to predict concrete structures having a hysteresis behavior difficult to model. Nevertheless, modeling of reinforced concrete materials demands substantial computational power, hence, RTHS is conducted at sampling rates as low as 50 Hz.

Other studies on nonlinear systems, i.e. MR damper tests conducted by Lin and Christenson (2011) do not address passive-on or semi-active cases since the fixtures on the test structure was not able to sustain forces larger than 500 N. In addition, this particular study, by using reduced order transfer functions, lacks of more realistic modeling approach such as MCK modeling to reflect physical properties of the structure.

Although RTHS validation experiments that involve linear specimens have the potential to work with controllable devices, previous work didn't unfold this venue (Wang et al., 2011; Shao and Enyart, 2012). Tests that examine the nonlinear damping systems did not consider controllable devices (Ashasi-Sorkhabi et al., 2013).

Therefore, the remaining challenges mentioned here still discourage some

researchers to practice RTHS methodologies in their own applications.

1.2 Objective and Scope

The need for a verification of RTHS proposed in this report arises from the following requirements and objectives listed below:

1. Validation of RTHS needs to be conducted on a realistic structure where physical portion of the structure in the RTHS represents a larger percentage of the reference structure. This report intends to demonstrate such a case.
2. MR damper introduces nonlinearity into the test, even when acting on a linear structure. Considering the fact that MR damper is a rate-dependent device, it is more challenging for validation of RTHS.
3. By changing level of MR damper forces through passive-on and semi-active control strategies, the effect of physical substructure contribution on RTHS performance can be evaluated. The proposed configuration in this report also contains such an approach towards verification of RTHS.

For the validation of RTHS, numerical evaluations of pure numerical simulation, RTHS results, and experimental results are compared with each other. Fig. 1.2 shows a schematic of the scenarios that have been employed through this report.

The primary scope of the comparisons are selected as in-plane displacements and accelerations of each floor, and the force at the MR damper and first floor interface. RMS and peak errors are presented to demonstrate RTHS can be used as a reliable and robust option among many testing methodologies.

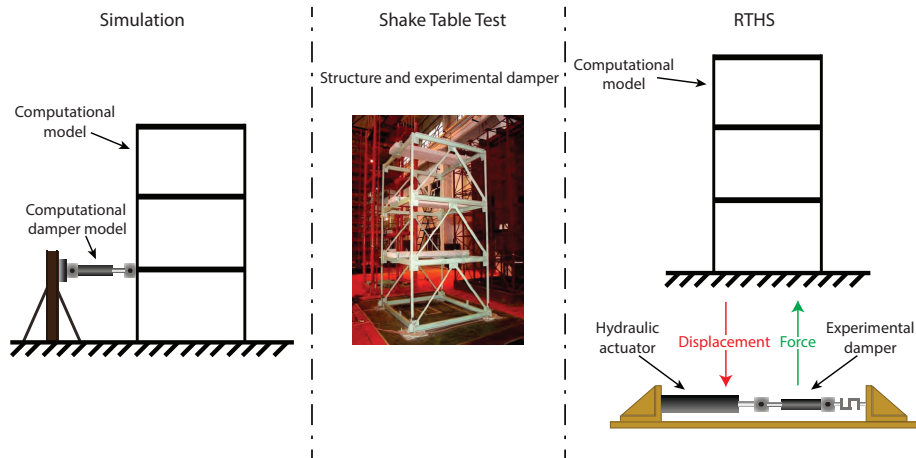


Figure 1.2: Schematic of Validation Scenarios

1.3 Overview

This report summarizes development and verification of two RTHS setups configured at HIT and Purdue. RTHS results are compared with global responses of a three story, large-scale, test structure excited with a shake table at HIT.

Chapter 2 presents an overview and purpose of the test configurations towards verification of the RTHS. Configurations described in this chapter include: (i) system identification, (ii) shake table configuration, (iii) RTHS setup at HIT, and (iv) RTHS setup at Purdue.

In Chapter 3, an improved system identification and model updating process towards structural control and model response estimation is proposed. First, a theoretical background on system identification and model updating is presented. Next, the motivation behind the proposed method along with the derivation of the methodology is explained. Finally, verification tests are conducted on the uncontrolled test structure when excited with various earthquakes using the shake table.

Chapter 4 discusses modeling of MR dampers at Purdue and at HIT through

characterization. Since shake table and RTHS tests have been performed at HIT and Purdue on different damper types, for the sake of a fair comparison, a formulation of Purdue damper in terms of HIT damper is provided in this chapter as well. In addition, fundamentals of control theory and design approaches for passive and semi-active control of MR dampers are discussed.

In Chapter 5, pure simulations using an integrated model containing numerical models of the test structure and MR damper are compared to shake table results. The errors tabulated in this chapter is considered as the baseline for RTHS comparisons.

Chapter 6 presents experimental verification by comparing shake table response of the test structure to RTHS results. In the first phase, shake table results of the structure are provided. An in-depth analysis of the comparisons is given and possible source of errors are discussed to justify the results.

Finally, Chapter 7 summarizes the important research findings throughout this report and draws general conclusions from the study presented here.

CHAPTER 2

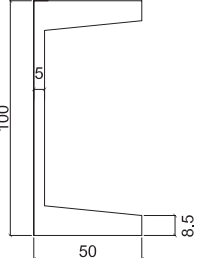
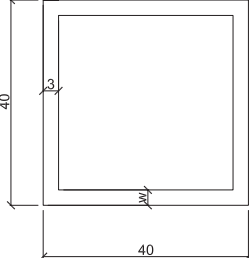
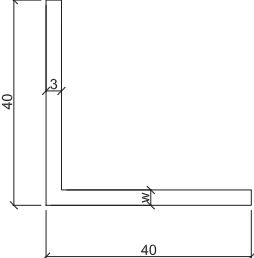
EXPERIMENTAL SETUP FOR SHAKE TABLE AND RTHS TESTS

In this chapter, an overview of experimental configurations built at Intelligent Infrastructure Systems Lab (IISL) at Purdue University and Structural Engineering Laboratory at HIT towards realizing the aims of this report is given. Section 2.1 focuses on the three story test structure and structural modifications performed on the structure. In Sections 2.2 and 2.3, configurations for system identification and shake table tests are described including instrumentation setup. Introductory information on the dampers used for shake table and RTHS tests is also explained in this section. In Section 2.4, the loading frame designed at HIT for actuator tracking evaluation, and in Section 2.5, RTHS setup developed at IISL are discussed in details. Finally, a summary of the chapter is given in Section 2.6

2.1 HIT Test Structure

The original test structure is a three-dimensional, three story frame located at Harbin Institute of Technology (HIT), China, shown in Fig. 2.1a. The structure has a base plan with dimensions 1.84 m by 2.04 m. Each story is 1.2 m tall and the total height is 3.6 m (See Fig. 2.1b). The columns, beams and girders are made of structural steel with an elastic modulus estimated to be 220 GPa. Each joint, where column and beam members are connected to each other, is welded and does not allow free rotation. The structure is braced in one direction with v-type braces such that the system is weak in the y-axis and strong along the x-axis (See Fig. 2.1c). At each story, a concrete slab weight approximately 250 kg is attached as a seismic mass. The total mass of the structure including the self-weight of the members is calculated to be 1066 kg. Section properties of the members used in the design of the PS is summarized in Table 2.1.

Table 2.1: Section Properties of the Prototype Structure

Beam and Girder					Column					Brace				
														
A	I_{X-X}	I_{Y-Y}	J	ρ	A	I_{X-X}	I_{Y-Y}	J	ρ	A	I_{X-X}	I_{Y-Y}	J	ρ
cm^2	cm^4	cm^4	cm^4	Kg/m	cm^2	cm^4	cm^4	cm^4	Kg/m	cm^2	cm^4	cm^4	cm^4	Kg/m
12.74	198.3	25.6	223.9	10.0	4.44	10.2	10.2	20.4	3.487	2.31	3.59	3.59	7.2	1.814

For passive-off, passive-on and semi-active vibration control tests, an MR damper is attached to the structure at first floor. To connect the MR damper to the first floor, a slight modification is performed at the first floor by adding a horizontal v-brace in the plan of the floor. Thus, the beam, where the MR

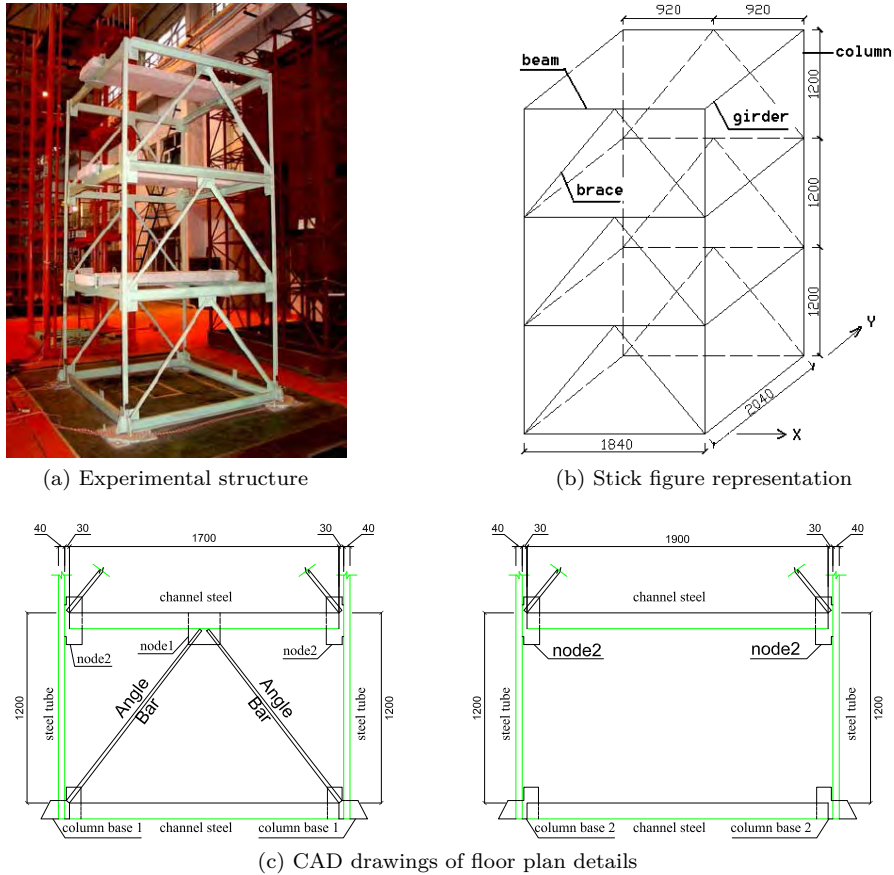
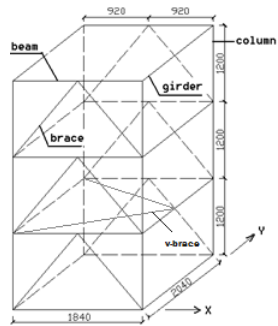


Figure 2.1: Original experimental structure

damper is attached, will have additional stiffness against deflection caused by damper force. A stick figure of the modified structure is shown in Fig. 2.2a. Top and side views of the MR damper attachment joint are presented in Figs. 2.2b and 2.2c. In addition, a detail where v-brace is welded to the beam-column joint is given in Fig. 2.2d. The cross-sectional properties of the v-braces are same as the girders/beams shown in Table 2.1. The additional first floor mass contribution to the v-braces is about 45 kg which makes the total mass of the structure about 1110 kg.



(a) Modified stick figure representation



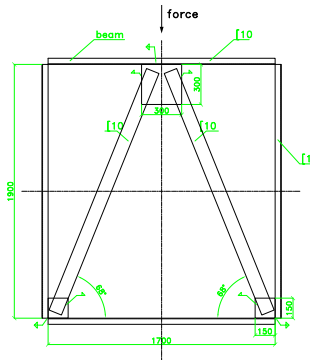
(b) Top view of MR damper attachment joint



(c) Side view of MR damper attachment joint



(d) Corner detail



(e) CAD drawings of floor plan details

Figure 2.2: Additional details for modified test structure

2.2 System Identification Test Equipment

Development of high fidelity mathematical models of the test structure is undertaken by choosing appropriate testing equipment. This section describes test instrumentation including DAQ system used for system identification.

DAQ System

To acquire system identification data of the test structure, NI USB-6259, a multi-functional data acquisition system box made by National Instruments is employed (see Fig. 2.3). The DAQ system has the capability to sample data upto 1.25 MHz rate from 16 differential analog input channels at 16 bit analog-to-digital conversion resolution. The data acquired online from DAQ system is transmitted over USB 2.0 to a Dell Inspiron 1720 notebook to be processed by DeweSoft Dynamic Signal Analyzer v6.6 developed by DeweSoft (see Fig. 2.4) The raw data is later exported **.mat* to be processed in [MATLAB \(2011\)](#).



Figure 2.3: NI USB-6259

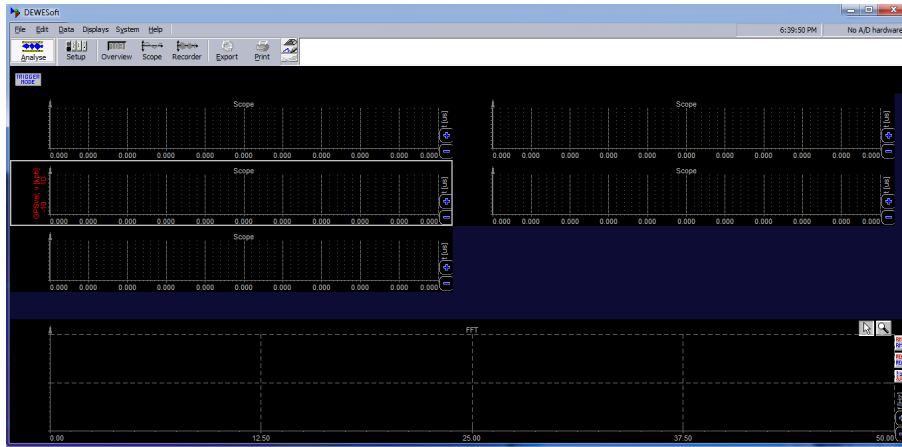


Figure 2.4: DeweSoft Start-up screen

Instrumentation

Charge-type accelerometers produced by Brüel & Kjær model #4368 with a flat frequency response between 0.2 Hz and 4800 Hz are used to measure acceleration response of the structure (see Fig. 2.5). The one-hand operatable modally tuned impact hammer used in the tests is made by Jiangsu Lianneng Electronic Technology Limited Corporation with a model #LC-01A from Sinocera Piezotronics branch (see Fig. 2.6). The hammer is equipped with a charge type load cell with model #CL-YD-303 and a rubber tip on the load cell. All together, hammer is rated to generate maximum thrust of 2 kN. The acceleration sensors and impact hammer are powered with signal conditioners capable of producing velocity and displacement by integration, belonging to Sinocera Piezotronics branch with model #YE5858A, which is based on Brüel & Kjær's model #2635 charge amplifier (see Fig. 2.7). The amplifier has selectable dial gains, high-pass filter ranging from 0.3 Hz to 10 Hz for acceleration measurements and a low pass filter from 300 Hz to 100 000 Hz (wide-band). All filters attenuate maximum 3 dB at the cutoff frequency during normal operation conditions. The decay rate for low

and high pass filters are 12 dB and 6 dB per octave, respectively.



Figure 2.5: Bröel & Kjør model #4368 with its Base Magnet

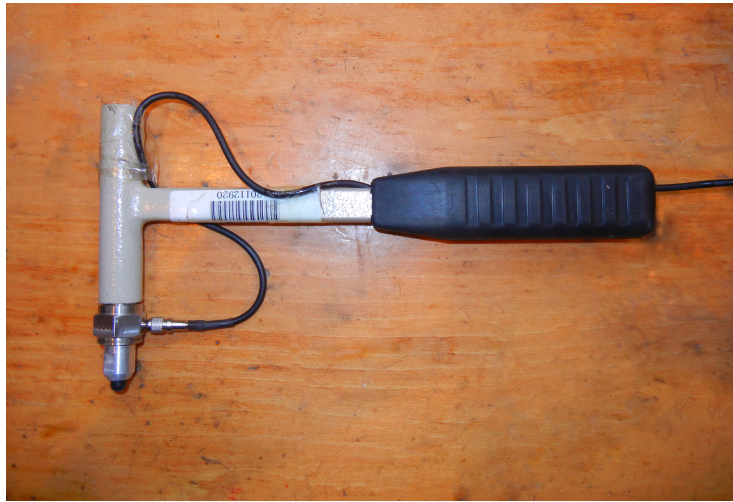


Figure 2.6: Jiangsu Lianneng made Impact Hammer

2.3 Shake Table Test Configuration

This section introduces the test structure used in the validation of RTHS along with the shake table and other test equipment including DAQs and instrumentation. Shake table test results are provided in Chapter 5.



Figure 2.7: Sinocera Signal Conditioners

2.3.1 Shake Table

The testing facility located in HIT is a unidirectional shake table and is 3 meters wide and 4 meters long in shaking direction. A photograph of the shake table is given in Fig. 2.8. The actuator attached to the shake table is manufactured by Schenck, shown in Fig. 2.9. The two column servo-hydraulic actuator with model #PM250R is rated up to 250 kN static loading or 200 kN dynamic loading and can drive the bare shake table (no payload) with a peak acceleration of ± 1.33 g, peak velocity of ± 600 mm/sec at a stroke restricted to ± 125 mm. The maximum payload and maximum overturning moment of the shake table is limited to 12 t and $30 \text{ t} \cdot \text{m}$, respectively. The hydraulic oil to the actuator is supplied by the hydraulic power unit produced by Schenck. The frequency of the excitation input is bounded between 0 Hz and 30 Hz. An #493.10 MTS FlexTest GT #100 Controller, shown in Fig. 2.10 is used to provide the control input to the shake table. The controller is capable of controlling of 8 servo-valves at the same time while sampling at a maximum rate of 6000 Hz using 16 bit resolution.

MTS #793.00 TestSuite Multipurpose software is used to drive the controller.
A screenshot of the software is given in Fig. 2.11.



Figure 2.8: Shake table located at HIT



Figure 2.9: 250 kN capacity Schenck Actuator



Figure 2.10: MTS FlexTest GT Controller

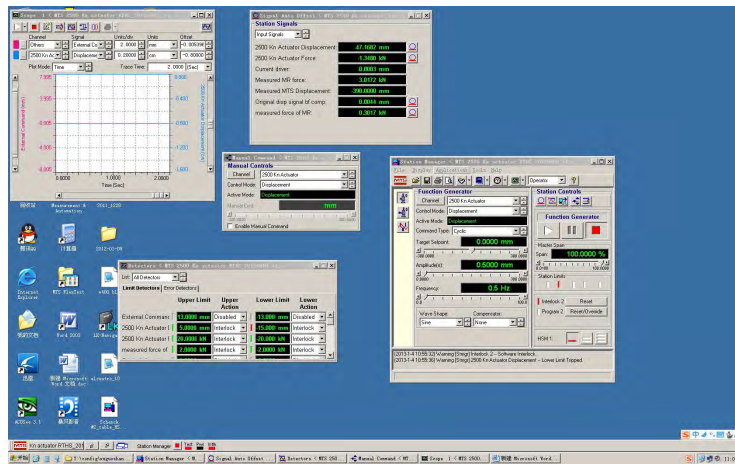


Figure 2.11: TestSuite Multipurpose Software Layout

2.3.2 Test Equipment

Equipment to measure shake table responses of the structure is categorized in two following subsections.

DAQ System

For data acquisition, Dong-Hua Universal Dynamic Signal Test System #DH5922 made by Jiangsu Donghua Testing Technology, that is capable of sampling 16 channels simultaneously up to 200 kHz at 24 bit conversion is used (see Fig. 2.12). The system is controlled with DHDAS dynamic signal test and analysis software v4.3.55 over IEEE 1394 interface also known as Firewire, and driven by Dell Inspiron 1720.



Figure 2.12: Dong-Hua Universal Dynamic Signal Test System

To acquire structural responses and to control equipments such as MR damper or current driver, DS1104 along with the terminal board CP1104 from dSPACE GmbH is selected as real-time control development platform (see Fig. 2.13). DS1104 is essentially a PCI board and can sample data at up to 250 MHz using 4 ADC input multiplex setting with 16 bit resolution and 4 ADC input sampling in parallel setting with 12 bit resolution. The system can also produce analog output using 8 DAC units with 16 bit resolution. ControlDesk Developer Version Release 6.3 software running on Dell Dimension 5150 desktop computer, which is also hosting DS1104, is used as the user interface to program and control real-time simulation that is compiled and downloaded via Simulink/Real-Time Workshop (see Fig. 2.14). Bröel & Kjør accelerometers

are paired with charge amplifier, Ke Dong KD #5018 made by Yangzhou Dynamic Electronics. KD #5018 has a configurable gain varying from 1 and 1000, high-pass filter ranging from 0.1 Hz to 10 Hz and a low pass filter from 300 Hz to 100 000 Hz (wide-band).

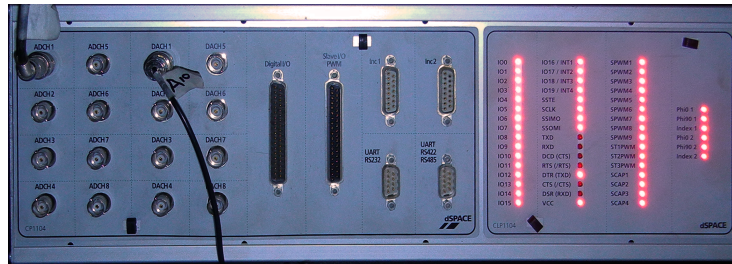


Figure 2.13: dSpace DS1104 System Terminal Board

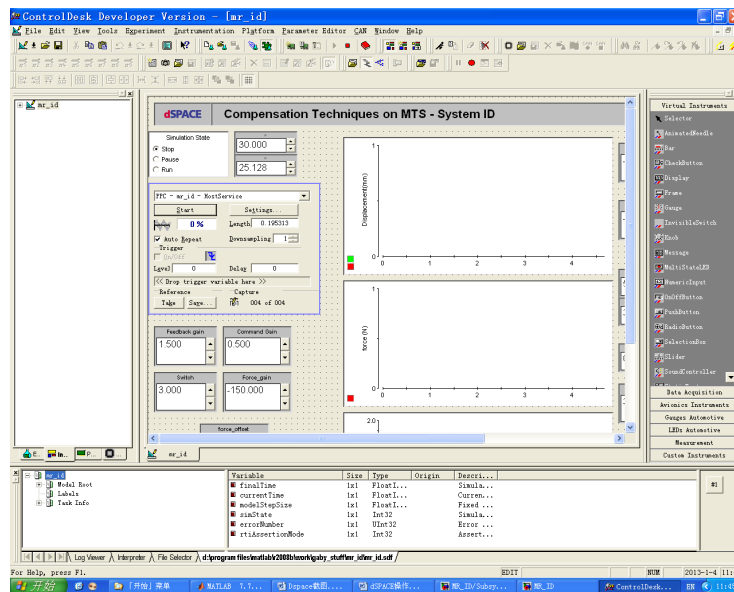


Figure 2.14: dSpace ControlDesk Software Layout

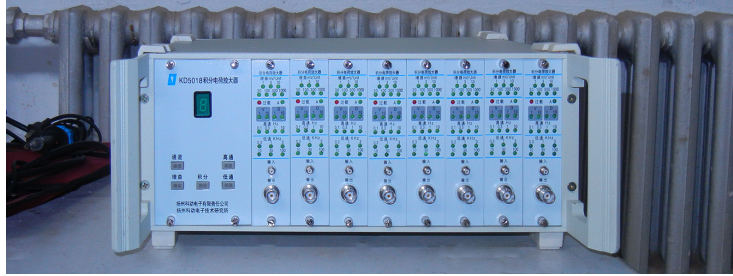


Figure 2.15: Ke Dong KD 5018 Signal Conditioner

Instrumentation

Charge-type accelometers from Bröel & Kjør explained in Section 2.2 are used to measure structural acceleration responses and ground acceleration of the shake table. For displacement measurements, LVDT and Laser sensors are used. The laser sensors made by Keyence with model LK-400 and LK-405 have ± 100 mm measurement range with extremely low linearity, $\pm 0.05\%$ over full scale (see Fig. 2.16a). The laser sensors are powered up by a LK-G3001V Controller (see Fig. 2.16b) that allows sampling rates reaching up to 50 000 Hz. In addition, Beijing Haiquan Sensor Technology made DC-type LVDTs with model #DA-50 (reengaging spring type) and #DA-150 (non-spring type) having respective strokes of ± 50 mm and ± 150 mm are used (see Fig. 2.17).

MR Damper

For passive-on/off and semi-active control tests, MR damper with model #RD-1005-3 made by LORD is used. The damper is capable of producing forces up to 2500 N when powered with an input current of 1 A. To power the damper, a voltage controllable current driver that can provide current up to 0 A to 3 A is used (see Fig. 2.18). The current driver is controlled via dSpace DS1104. To measure force generated by MR damper, force transducer #661.19F-03 produced by MTS with a load capacity of ± 15 kN is used (see Fig. 2.19). The force



Figure 2.16: Keyence Laser Displacement Sensor and Controller



Figure 2.17: #DA-50 LVDT

transducer is powered by MTS Flex GT Controller. To attach the MR damper to the first floor of the structure, a fixture rigid enough not to deflect more than ± 0.1 mm under maximum MR damper load is designed (see Fig. 2.20). For additional stiffness, tension-compression bars are welded to the rigid fixture.

2.3.3 Ground Excitation

Generally, any actuator has physical limitations in terms of realizing the desired input. The limitations can often manifest as time delay or amplitude loss. For this reason, a delay and amplitude compensation scheme needs to be implemented if the reproduction of the excitation input is a must. The actuator of the shake table at HIT is controlled on the software-hardware level with inter-



Figure 2.18: MR Damper Amplifier



Figure 2.19: MTS Load Cell

nal PID control. Since displacement is used as the feedback to the PID loop, acceleration records are double integrated with trapezoidal integration rule in MATLAB. Excitation input is selected as (i) historical El Centro earthquake recorded at El Centro Terminal Substation Building's concrete floor during Imperial Valley, CA earthquake on May 18, 1940, (ii) acceleration-dominant Kobe earthquake recorded at station Takarazuka, Japan on January 16, 1995 and (iii) velocity-dominant Morgan Hill, CA earthquake recorded at station Gilroy Array #6 on April 24, 1984. Since the existence of the MR damper fixture is

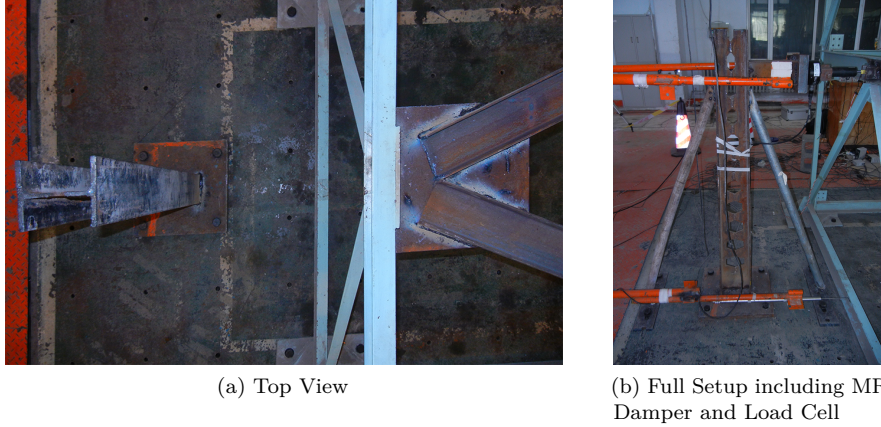


Figure 2.20: MR Damper Fixture

limiting maximum allowable stroke of the shake table to nearly ± 75 mm, El Centro and Kobe earthquakes are scaled to 50 % and 35 % of their recorded peak peak ground displacement, respectively. No time scaling is applied to any of the ground excitations. Tracking performance of the shake table with payload while simulating earthquakes is given in Fig. 2.21 for El Centro, in Fig. 2.22 for Kobe and in Fig. 2.23 for Morgan Hill earthquakes. The relative error calculated as $RMS_{Error}/RMS_{Reference}$, where $RMS_{Reference}$ is historical data, is found [86.8, 1.16] % for El Centro Earthquake acceleration and displacement, [80.5, 7.90] % for Kobe Earthquake acceleration and displacement and [81.0, 5.23] % for Morgan Hill Earthquake acceleration and displacement, respectively. Although reported errors on accelerations are relatively high, the shake table showed good performance in tracking of the intended displacement.

2.4 Loading Frame at HIT

This section introduces the test equipment including DAQs required to conduct tracking performance tests of actuator compensation algorithms at HIT. Results

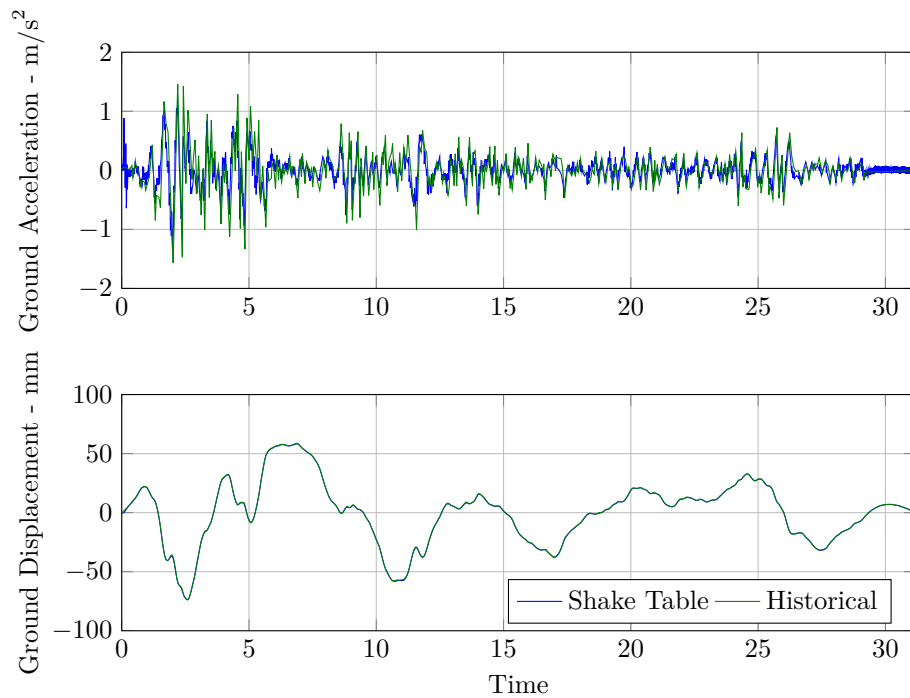


Figure 2.21: El Centro Earthquake Comparison

are provided in Section 6.1.3.

2.4.1 Test Equipment

Tracking tests conducted at HIT are performed with MR damper #RD-1005-3 attached to an uniaxial servohydraulic load frame with a model #311.41 from MTS and a capacity of ± 2500 kN (see Fig. 2.24). The hydraulic system has a saturation velocity limit of ± 90 mm/sec when six pump units are running on Model #505.180 MTS SilentFlo Hydraulic Power Unit providing up to 160 gal/min hydraulic oil flow with a pressure of 3000 psi. The force transducer and MR damper is attached to the actuator with hydraulically controlled wedge grips #641.39 that requires #685 hydraulic grip supply unit, both made by MTS. For inner-loop and outer-loop control, Flex GT Controller and DS1104 are used,

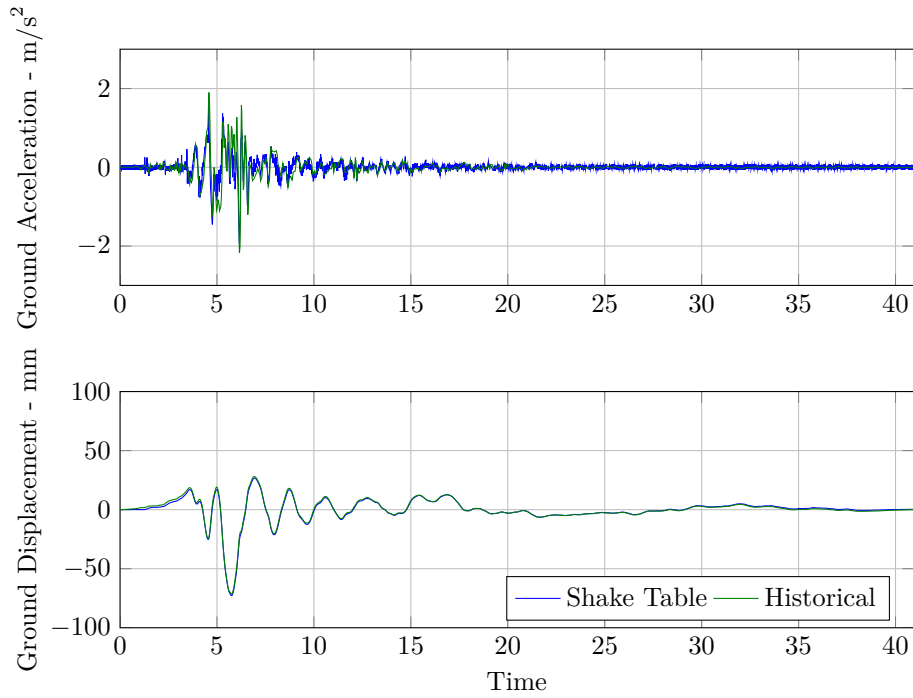


Figure 2.22: Kobe Earthquake Comparison

respectively.

2.5 Real-time Hybrid Simulation Setup at Purdue

This section introduces the test equipment including DAQs required to conduct RTHS at IISL. The results of RTHS conducted on this frame are provided in Chapter 6.

2.5.1 Test Equipment

RTHS tests conducted at IISL are performed with MR damper #RD-8041-1 made by LORD. Current in the MR damper is controlled by LORD Wonder Box

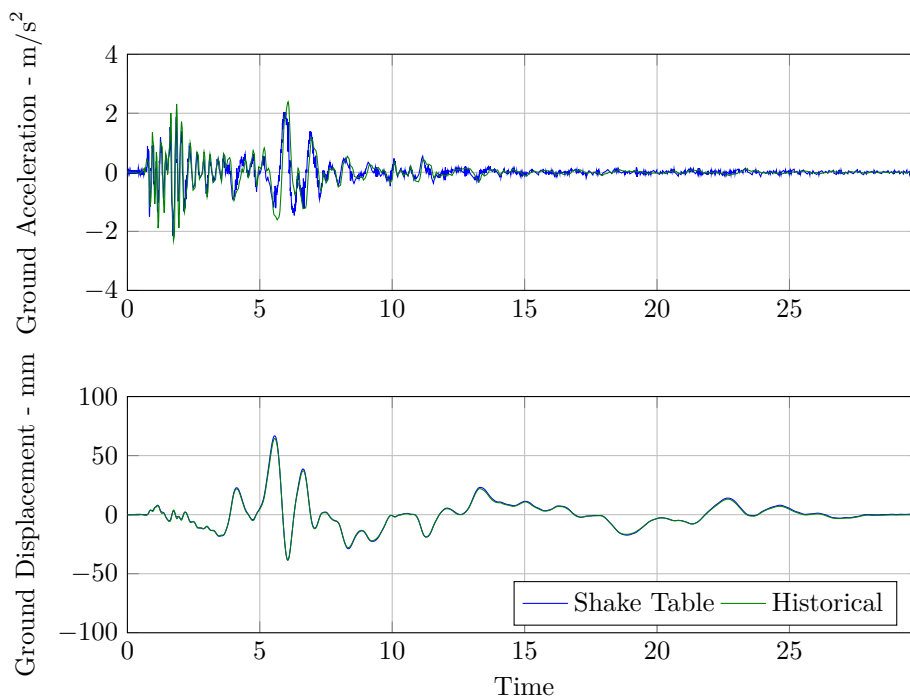


Figure 2.23: Morgan Hill Earthquake Comparison

Device Controller Kit with model #RD-3002-03 via external command. The force of MR damper is measured by Omega made model #LC101-2K S-type force transducer with a capacity of ± 9000 N (± 2000 lb). An Omega made model #DMD-465WB wide bandwidth signal conditioner module with a frequency response up to 2 kHz is used to power up the force transducer. Both damper and load cell are attached to a loading frame also containing Shore Western made actuator model #910D rated with (± 5000 N) force capacity (Fig. 2.25). A MOOG made #G761-3004B controllable servo-valve that provides a flow rate of 10 gal/min at 1000 psi valve pressure drop is used to operate actuator. The oil supply is provided by a model #505.120 MTS SilentFlo Hydraulic Power Unit providing up to 120 gal/min hydraulic oil flow with a pressure of 3000 psi, when four motor pumps are running.



Figure 2.24: MTS Loading Frame with MR damper and Load Cell attached at HIT

For the inner-loop control of the actuator, a Shore Western SC6000 analog servo-hydraulic control system is used (see Fig. 2.26). The actuator is operated through Shore Western MDOF Control System software running on a PC, embedded in SC6000.

For the outer-loop control, a performance real-time target machine made by Speedgoat is used (see Fig. 2.27). RT system has a software-level RT-kernel that is configurable using xPC/Simulink/MATLAB. High-resolution, high accuracy A/D board model #IO112 supporting up to 32 differential simultaneous A/D

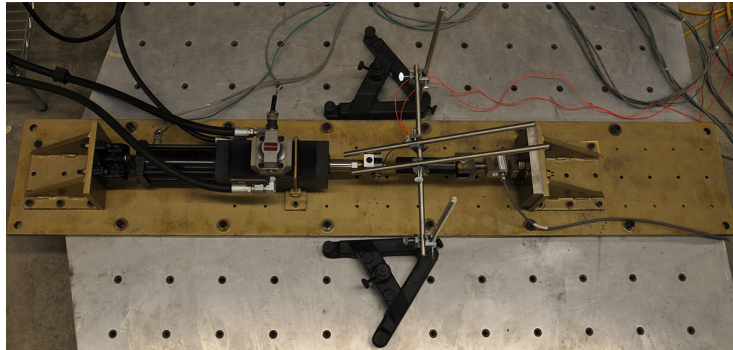


Figure 2.25: Shore Western Actuator, MR Damper and Load Cell attached to Loading Frame



Figure 2.26: Shore Western SC6000 Controller

channels with 18-bit resolution and D/A board model #IO113 supporting up to 8 differential D/A channels with 18-bit resolution are integrated into this digital control system.

2.6 Summary

In this chapter, the experimental setup for system identification and shake table tests including sensors, DAQ and actuator systems are described. Furthermore,



Figure 2.27: Speedgoat Performance Real-time Target Machine

earthquake excitations to be used for the validation of RTHS and also shake table performance for the given ground motions are briefly discussed. In addition, loading frame located at HIT and RTHS setup located at IISL are explained in detail.

CHAPTER 3

MODELING, SYSTEM IDENTIFICATION AND MODEL UPDATING OF THE TEST STRUCTURE

A proper mathematical description of the test structure is crucial for the comparisons to be performed using RTHS. Development of the system model must take the dynamic characteristics of the structure into account. Nevertheless, success of control design strategies benefits from an appropriate model.

In essence, system identification is the process of establishing a model that reproduces the input/output behavior of the target structure. By selecting a system identification procedure suitable for the experimental objectives, one can develop reliable predictions and explain system behavior ([Catbas et al., 2013](#)). As explained by [Aktan and Moon \(2005\)](#), to fully achieve potential

outcomes of system identification, six steps should be followed. Those are: (i) conceptualization of the structure based on the needs; (ii) a-priori modeling; (iii) experimentation and collection of data; (iv) feature extraction; (v) model calibration and (vi) model evaluation.

In this chapter, an overview of system modeling, identification and model updating to develop an appropriate mathematical description of the test structure is given. Section 3.1 presents a baseline model of the test structure along with the mathematical formulations in state-space representations for the numerical and RTHS evaluations. Next, Section 3.2 introduces a commonly used system identification methodology, Eigensystem Realization Algorithm (ERA) along with its theory and modification of the method for real world application. In Section 3.3, a new model updating process aggregating identified system characteristic with physical mass-damping-stiffness properties is presented with verification tests. In Section 3.4, the limitations of the proposed method are discussed. Evaluation criteria used for performance assessment of the developed model is given in Section 3.5. Section 3.6 presents the initial model based on the baseline modeling assumptions, identified results of the system, transfer function comparisons between different models and lastly comparison of simulated results of the model to experimental shake table tests of the uncontrolled structure. Finally, a summary of the chapter is given in Section 3.7

3.1 Baseline Model

For the development of the model, the structure is assumed to be a linear system and remains linear throughout the entire test plan. Thus, based on the description presented in Section 2.1, a simple mass-damper-spring system

equivalent to a shear model of the structure is developed as follows:

$$M\ddot{x} + C\dot{x} + Kx = -M\ddot{x}_g + F \quad (3.1)$$

where M , C and K are the mass, damping and stiffness matrices respectively. The right-hand-side of the equation represents earthquake excitation, \ddot{x}_g and force input, F to the structure.

The system is established to have three degrees of freedom (DOF), where each node represents a floor of the test structure. Seismic concrete masses and structural weight are lumped at floor level for each degree of freedom, as shown in Fig. 3.1. m_1 and m_3 represent first floor and top floor, respectively. This system model has the following structural properties:

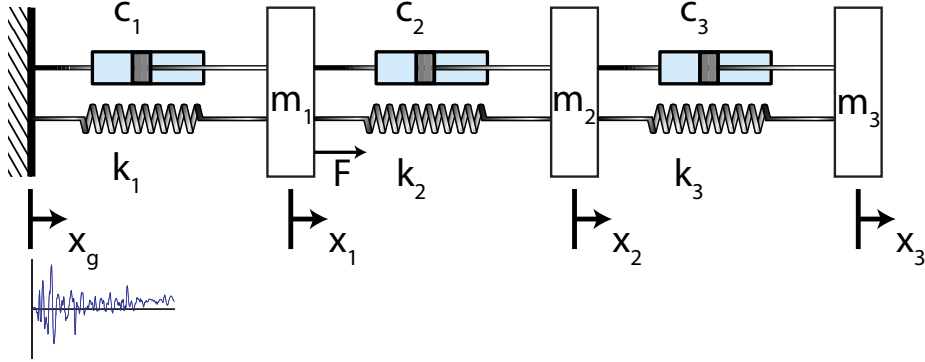


Figure 3.1: Lumped mass model idealization of the test structure

$$[M] = \begin{bmatrix} m_1 & 0 & 0 \\ 0 & m_2 & 0 \\ 0 & 0 & m_3 \end{bmatrix} \quad (3.2a)$$

$$[C] = \begin{bmatrix} c_1 + c_2 & -c_2 & 0 \\ -c_2 & c_2 + c_3 & -c_3 \\ 0 & -c_3 & c_3 \end{bmatrix} \quad (3.2b)$$

$$[K] = \begin{bmatrix} k_1 + k_2 & -k_2 & 0 \\ -k_2 & k_2 + k_3 & -k_3 \\ 0 & -k_3 & k_3 \end{bmatrix} \quad (3.2c)$$

$$[F] = \begin{bmatrix} f \\ 0 \\ 0 \end{bmatrix} \quad (3.2d)$$

The model described herein is designed to reproduce only horizontal responses in the weak axis when a disturbance is applied as means of ground motion or external force in the weak axis. Torsional and out-of-plane responses are omitted in the modeling assumptions.

Given M and K , as an alternative to the proportional damping matrix, a non-proportional type can be formed based on a specific set of damping ratios:

$$[C] = [M]\Phi(2\xi[2\pi f])\Phi^T \quad (3.3)$$

where Φ is mode shape of the system, f and ξ represent diagonal matrix of natural frequencies in Hertz and damping ratios, respectively.

(iii) State-space Formulation

For continuous linear time invariant (LTI) systems, the standard state-space representation derived either from physical properties or experimental data of the baseline model is introduced below:

$$\dot{x} = Ax + Bf + E\ddot{x}_g \quad (3.4)$$

$$y = Cx + Df + F\ddot{x}_g \quad (3.5)$$

where, x is the internal state vector, y is system response vector, f is the input force and \ddot{x}_g is the ground acceleration. The state matrix, A and input-to-state matrix, B and E of the system in Eq. (3.4) can be written as:

$$[A] = \begin{bmatrix} 0 & I \\ -M^{-1}K & -M^{-1}C \end{bmatrix}, [B] = \begin{bmatrix} 0 \\ M^{-1}P \end{bmatrix}, [E] = \begin{bmatrix} 0 \\ -I \end{bmatrix} \quad (3.6)$$

where P and G are influence matrices of applied external force and ground motion excitation. $[C]$, $[D]$ and $[F]$ matrices depend on the chosen output vectors. For a system that produces displacement and velocity responses relative to the ground and absolute acceleration responses, the state-to-output and feedthrough matrices are given as:

$$[C] = \begin{bmatrix} 1 & 0 \\ 0 & 1 \\ -M^{-1}K & -M^{-1}C \end{bmatrix}, [D] = \begin{bmatrix} 0 \\ 0 \\ M^{-1}P \end{bmatrix}, [F] = \begin{bmatrix} 0 \\ 0 \\ 0 \end{bmatrix} \quad (3.7)$$

Given the above state-space representations, P is formulated as:

$$[P] = \begin{bmatrix} 1 \\ 0 \\ 0 \end{bmatrix} \quad (3.8)$$

3.2 System Identification

To construct the state-space matrices given in Eqs. (3.4) and (3.5), M , C and K matrices can either be approximated from the lumped 3-DOF model presented in Section 3.1 or can be estimated from experimental data. Considering the fact that deficiencies and discrepancies between the estimations and experimental data are often evident, implementing a system identification method tool that reveals dynamic properties of the structure is needed.

For this study, a commonly used time-domain approach, ERA is selected. [Juang and Pappa \(1985a\)](#) proposed ERA to extract modal parameter and create a minimal realization model that replicates the output response of a linear dynamical system when it is subjected to a unit impulse. The success of this algorithm has been verified in multiple studies ([Caicedo et al., 2004](#); [Giraldo et al., 2004](#); [Caicedo, 2011](#)). The workflow for ERA can be summarized in five steps. Those are (i) Hankel matrix assembly, (ii) singular value decomposition, (iii) state-space realization, (iv) eigenvalue extraction and (v) model assurance.

3.2.1 Procedure

A discrete-time representation of Eq. (3.4) with n -dimensional state vector, x ; m -dimensional control input, u and p -dimensional output vector, y can be written

as:

$$x(k+1) = Ax(k) + Bu(k) \quad (3.9a)$$

$$y(k) = Cx(k) \quad (3.9b)$$

where A is $n \times n$ matrix, B is $n \times m$ matrix and C is $p \times n$ matrix. The matrix impulse response, known as Markov parameter sequence, can be derived from Eqs. (3.9a) and (3.9b):

$$Y(k) = CA^{k-1}B \quad (3.10)$$

where $Y(k)$ is $p \times m$ matrix. $Y_{ij}(k)$ is i th output to j th input at time step k .

(i) Hankel matrix assembly

As the first step of the ERA algorithm, Hankel matrix for a time step k is formed:

$$H(k-1) = \begin{bmatrix} Y(k) & Y(k+1) & \cdots & Y(k+s) \\ Y(k+1) & Y(k+2) & \cdots & Y(k+s+1) \\ \vdots & \vdots & \ddots & \vdots \\ Y(k+r) & Y(k+r+1) & \cdots & Y(k+r+s) \end{bmatrix} \quad (3.11)$$

For a typical application, as a rule of thumb, r , row of $H(k-1)$ matrix should be at least 10 times the modes to be identified and s , column of $H(k-1)$ should be 2-3 times of r .

(ii) Singular value decomposition

A singular value decomposition is performed using $H(0)$:

$$H(0) = PDQ^T \quad (3.12)$$

where P is $rp \times n$, Q is $ms \times n$ and D is $n \times n$ diagonal matrix.

(iii) State-space realization

By integrating P , D , Q and $H(k)$, a minimum realization of the identified system in Eqs. (3.9a) and (3.9b) can be derived in state-space form:

$$A = D^{-1/2}P^T H(1)QD^{-1/2} \quad (3.13a)$$

$$B = D^{1/2}Q^T E_m \quad (3.13b)$$

$$C = E_p^T P D^{1/2} \quad (3.13c)$$

where $E_p^T = [I_p \ 0]$ and $E_m^T = [I_m \ 0]$.

(iv) Eigenvalue extraction

Natural frequencies, damping ratios and mode shapes can be obtained by applying eigen-decomposition on the state matrix, A , as given in Eq. (3.13a). A typical way to obtain the identified parameters is prescribed below:

$$[v, \lambda] = eig(A) \quad (3.14a)$$

$$s = \ln(\lambda)f_s \quad (3.14b)$$

$$f_{dE} = \frac{\Im(s)}{2\pi} \quad (3.14c)$$

$$\zeta_E = \frac{\Re(s)}{|s|} \quad (3.14d)$$

$$\Phi_E = E_p^T P D^{1/2} v \quad (3.14e)$$

where v and λ are eigenvectors and eigenvalues of the system in z -plane since state A is in discrete-time form, f_s is the sampling rate of the system in Hz , s is the Laplace root of the system converted from the z -plane, f_{dE} , ζ_E and Φ_E are experimental damped frequency in Hz , damping ratio and complex mode shape,

respectively. The experimental natural frequency of the system can be obtained as following:

$$f_{nE} = \frac{f_{dE}}{\sqrt{1 - \zeta_E}} \quad (3.15)$$

where f_{dE} and f_{nE} are experimentally obtained damped and natural frequencies, respectively.

Most of these operations are automated through *damp* function in [MATLAB \(2011\)](#).

Although for typical ERA applications mode shapes will be complex-valued, as it will be shown later in Section 3.3, model updating process requires a real mode shape. It is expected that a transformation from real to complex mode shape should maintain the original information of the identified complex mode shape to conserve dynamic characteristic of the test structure as much as possible ([Panichacarn, 2006](#)). Thus, a rotation transformation is applied to reduce the error between real and complex mode shapes:

$$\phi_{iEr} = \phi_{iE} / \phi_{1iE} \quad (3.16a)$$

$$\phi_{iEreal} = \text{sgn}(\Re(\phi_{iEr})) \odot \|\phi_{iEr}\| \quad (3.16b)$$

where ϕ_{iE} is the *i*th column of Φ_E , ϕ_{1iE} is the first element of ϕ_{iE} , ϕ_{iEr} is rotated ϕ_{iE} , $\|\phi_{iEr}\|$ is absolute value of ϕ_{iEr} , $\text{sgn}(x)$ is the *signum* operator for x , \odot is the element-by-element vector multiplication operator, and finally ϕ_{iEreal} is real mode shape of the *i*th column of Φ_E . Right hand side of Eq. (3.16a) is basically a rotation transformation where ϕ_{iE} is normalized with respect to its first element. The procedure minimizes the imaginary part of the complex mode shape such that Eq. (3.16b) is able to produce real values with a minimal error.

To understand the effect of Eq. (3.16a) better, an example is presented. For a 3-DOF model as described in Eqs. (3.2a) to (3.2c), where system parameters

are $[m_1, m_2, m_3] = [1, 1, 1]$ kg, $[c_1, c_2, c_3] = [10, 10, 10]$ N sec/m and $[k_1, k_2, k_3] = [1000, 1000, 1000]$ N/m, initial and rotated values of the first mode shape are shown in Fig. 3.2. The reduction in the imaginary part should be noted.

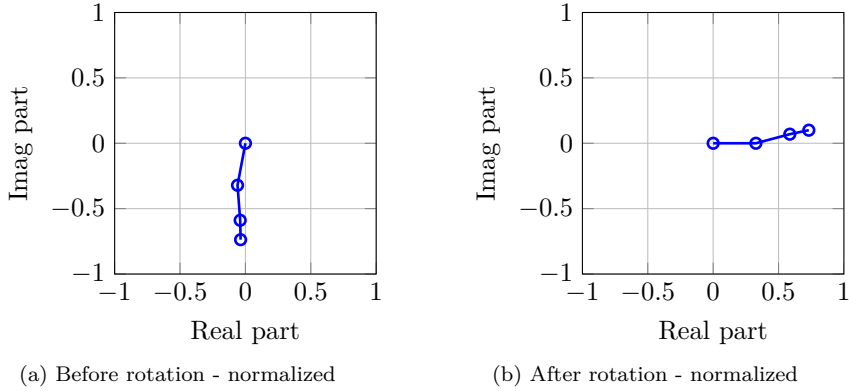


Figure 3.2: Effect of Eq. (3.16a) on the complex mode shapes

(iv) Model Assurance

Quality of the identified modal parameters is estimated through model assurance indicators. A model assurance criteria introduced by [Juang and Pappa \(1985b\)](#), known as the Model Amplitude Coherence (MAC) indicator does not always deliver the most reliable values. The flaws of MAC are resolved with Extended Modal Amplitude (EMAC). EMAC is explained in detail by [\(Pappa, 1994\)](#).

3.2.2 Application

Theory behind the ERA for system identification has been explained in the previous section. In this section, (i) collection, (ii) preparation, (iii) pre-processing, and regeneration of the data is explained.

(i) Collection

ERA is effective for identifying structural characteristics, and is intended to be applied to impulse response functions. An impulse response function can be retrieved either from any type of transfer function by applying inverse Fourier transformation or directly from structural responses to an impulse. For this study, impact hammer testing is selected as the most appropriate testing methodology.

In concept, a hammer impact, which is equipped with a load cell at its tip, can produce a broadband signal at contact time and excite each mode of the structure with equal energy. For proper testing, the structure should be instrumented at several points based on the available sensors, data channels on data acquisition system and testing plan (Trethewey and Cafeo, 1992). In typical applications, system responses are captured with accelerometers placed at critical points.

Theoretically, a single hit would suffice for ERA to capture system dynamics. However, with colored or colorless noise present, and small-scale local and global nonlinearities in the structure, some performance degradation during parametric estimations such as erroneous minimum realization or fictitious natural frequencies is expected. Performing a large number of impacts will manage the issues stated above to some extent, as it will provide more averaging for frequency domain pre-process and thus will result in higher quality data.

Lastly, between each hammer hit, system should be left in free-vibration until impact energy dies in the system substantially through structural damping.

(ii) Preparation

Data gathering of an impact test should take the least effort and time, especially if the system will be excited at multiple locations. Since setting DAQ system

for each hit is time consuming, all of the impact data and system response generated for a single contact point should be collected at one single run. After data collection, each hit and associated outputs can be manually parsed. To automate parsing with a minimal user-software interaction, a MATLAB script has been developed. Features such as automatic parsing and windowing has been added to align with project goals.

Essentially, script described herein manipulates and parses the impact and response data in `*.mat` file format based on user selections. These selections include: (i) minimum peak threshold for the impact force to be identified, (ii) order number of successful impacts, (iii) impact length, (iv) exponential decay window parameters for system response; and (v) pre- and post-impact rectangular time window parameters for the impact force data. The procedure is summarized in the flow diagram given in Fig. 3.3.

As the first step, the script identifies the peaks in the impact data according to the threshold. After user manually rejects unsuccessful hits, the remaining response data is parsed based on the window length parameter.

The second step is windowing. During impact testing, the tester should wait for some amount of time between each hammer hit until system damps out completely. For lightly damped systems, waiting time can take more than a minute. In cases where structure needs to be excited, for instance, thirty times, test may take over thirty minutes. Thus, tester may choose to shorten the impact period and hit the system before it dies out. However, when a discontinued measurement is converted to frequency domain through discrete Fourier transformation (DFT), the rectangular window applied by default is going to create spectral leakage. Although spectral leakage cannot be completely prevented, the effect of it in the measurement can be minimized by the use of exponential decay window or so-called damping window for freely vibrating

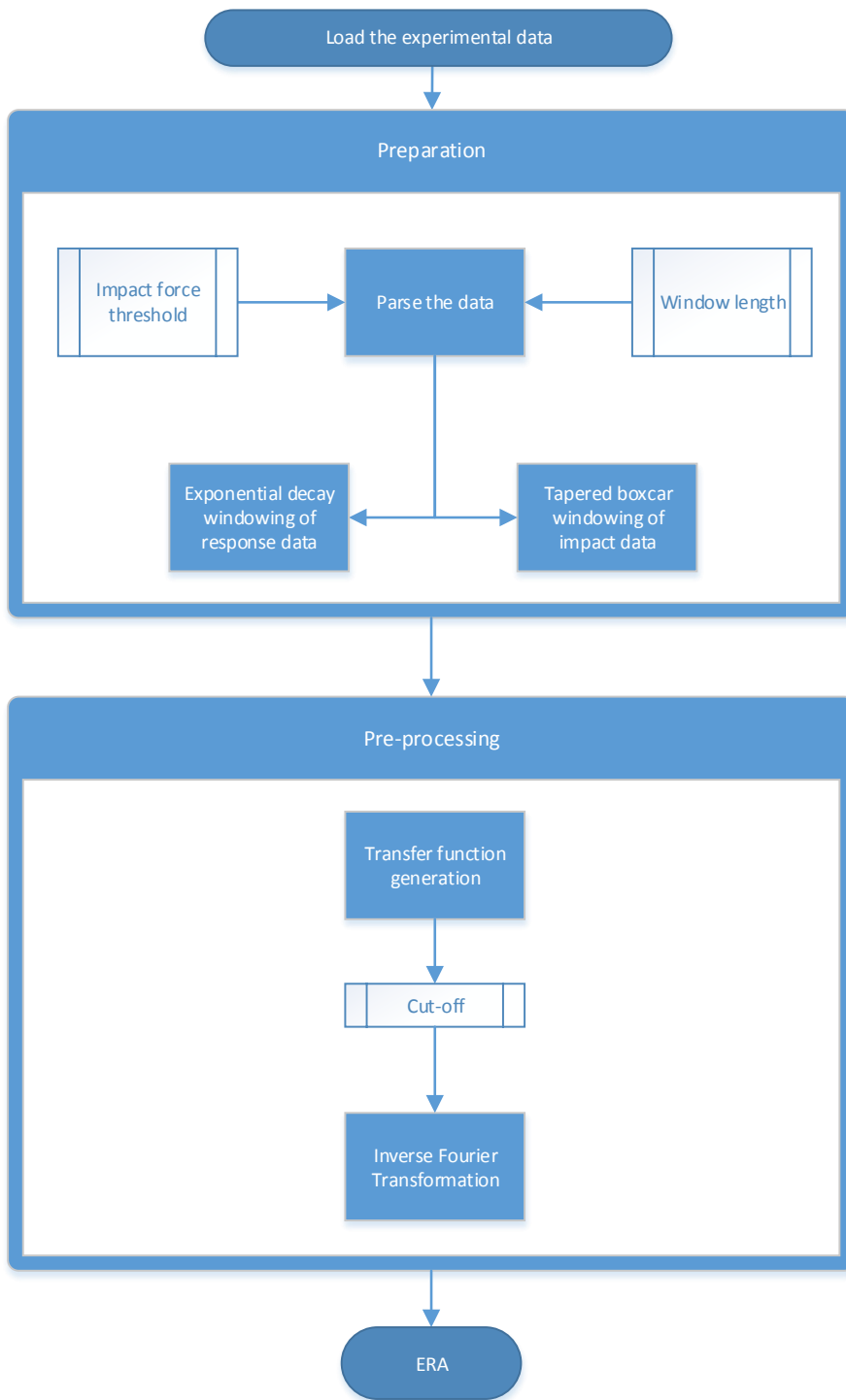


Figure 3.3: Impact Data Parser Script Workflow

systems. An exponential decay window can be represented as given by [Trethewey and Cafo \(1992\)](#):

$$w_{exp}(t) = \begin{cases} e^{-\frac{t}{\tau_w}} & 0 \leq t \leq T \\ 0 & T < t \end{cases} \quad (3.17)$$

where τ_w is time constant and T is length of window. τ_w is chosen based on desired decay ratio:

$$\tau_w = -\frac{T}{\ln(r_{decay})} \quad (3.18)$$

where r_{decay} is decay ratio in percentage. A windowed response, y_{iw} should be formulated as:

$$y_{iw} = w_{exp}y_i \quad (3.19)$$

To reject the noise in the impact force, a boxcar window is applied. A boxcar function can be described as:

$$w_{box}(t) = \begin{cases} 1 & T_{prehit} < t < T_{posthit} \\ 0 & otherwise \end{cases} \quad (3.20)$$

where T_{prehit} is the point of time before the impact, $T_{posthit}$ is the point of time after the impact that contains ringing of the sensor. Often, to minimize the spectral leakage, tapered half-sin is concatenated with box car function. A half-sin function is given below:

$$w_{sin-pre}(t) = \sin(k_{sin} * t) \quad (3.21a)$$

$$w_{cos-post}(t) = \cos(k_{cos} * t) \quad (3.21b)$$

where k is a shape modifier. Finally, the tapered boxcar window becomes:

$$w_{taper}(t) = \begin{cases} 0 & t \leq T_{start} \\ \sin(k_{sin} * t - T_{start}) & T_{start} < t \leq T_{prehit} \\ 1 & T_{prehit} < t < T_{posthit} \\ \cos(k_{cos} * t - T_{posthit}) & t \leq T_{posthit} + T_{end} \\ 0 & t > T_{posthit} + T_{end} \end{cases} \quad (3.22)$$

where T_{start} and T_{end} are the start and end of the taper window, respectively. k_{sin} and k_{cos} should be selected in such a way that $\sin(k_{sin} * t)$ and $\cos(k_{cos} * t - T_{posthit})$ should yield 1 at T_{prehit} and at T_{cos} , respectively. Tapered boxcar window based on Eq. (3.22) is shown in Fig. 3.4.

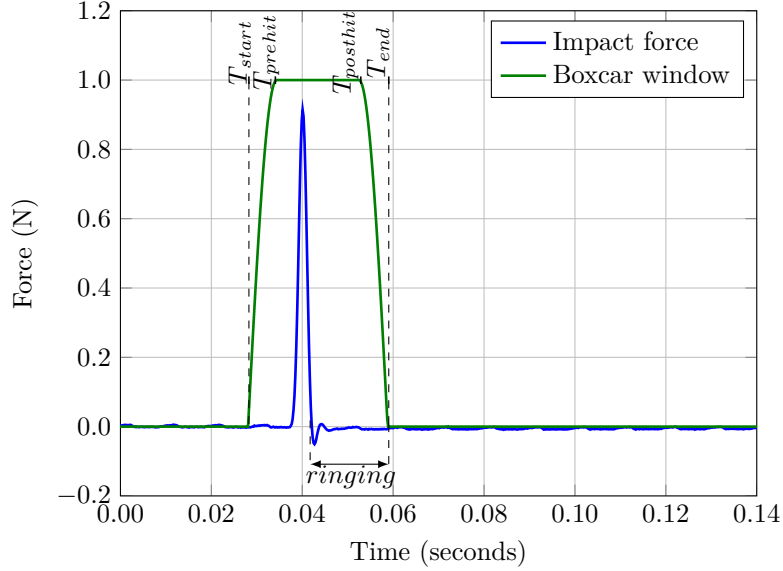


Figure 3.4: Tapered boxcar window

In conclusion, a windowed response, y_{iw} should be formulated as:

$$y_{iw} = w_{taper}y_i \quad (3.23)$$

After the windowing is performed, parsed data is ready to be pre-processed in frequency domain.

Although exponential and force window functions can reduce the leakage phenomenon, it introduces bias error on the estimated frequency response functions, hence, natural frequencies and damping ratios to be identified. Therefore, it is always a good practice to compare model estimations with experimental data after system identification and model updating. The effect of windowing has been discussed in depth by [Halvorsen and Brown \(1977\)](#) and [McConnell and Varoto \(1995\)](#).

(iii) Pre-processing

As stated before, frequency domain pre-processing of data can minimize effect of nonlinearities and noise when multiple transfer functions are averaged. Here, production and averaging of transfer functions, and reconstruction of the impulse response function (IRF) by Inverse Fourier Transformation are explained before the resulting IRF is used for ERA. Procedures involving pre-processing is summarized in Fig. 3.4.

A system can be idealized as in Fig. 3.5, where $h(t)$ is IRF, $x(t)$ and $y(t)$ are system inputs and outputs, respectively ([Craig and Kurdila, 2006](#); [Chopra, 1995](#)). The impulse function can be defined as:

$$h(t) = \frac{y(t)}{x(t)} \quad (3.24)$$

A linear relationship of the system output to its input can be described in the

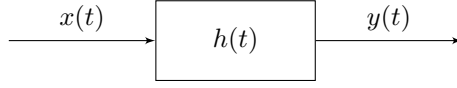


Figure 3.5: An Idealization of a Linear System in Time Domain

complex Laplace domain. Frequency response function, also known as, transfer function, $H(s)$ is defined as such:

$$H(s) = \frac{Y(s)}{X(s)} \quad (3.25)$$

where $Y(s)$ and $X(s)$ are the input and output in Laplace domain. Eq. (3.25) can be rewritten in frequency domain:

$$H(f) = \frac{Y(f)}{X(f)} \quad (3.26)$$

or

$$H(f) = \frac{S_y(f)}{S_x(f)} \quad (3.27)$$

where S_x and S_y are Fourier spectrum of $x(t)$ and $y(t)$. S_y and S_x can be easily obtained by applying Fast Fourier Transformation to input and outputs of the system. Although Eq. (3.27) is sufficient to generate a unit impulse frequency response function, for impact hammer test, system response to hammer input is more prone to noise compared to the input. To reduce the effect of noise, the frequency response function is redefined by multiplying right hand side nominator and denominator of $H(f)$ with complex conjugate of S_y :

$$\begin{aligned} H(f) &= \frac{S_y(f)}{S_x(f)} \\ &= \frac{S_y(f) \cdot S_y^T(f)}{S_x(f) \cdot S_y^T(f)} \\ &= \frac{G_{yy}(f)}{G_{xy}(f)} \end{aligned} \quad (3.28)$$

where S_y^T is complex conjugate of S_y , Gyy is the cross-spectral density of $x(y)$ and $y(x)$ and Gxy are auto-spectral density of $x(y)$. For each impact, a new transfer function can be constructed using the method explained above. Yet, transfer functions are affected by the noise and nonlinearities. Assuming the test structure is linear and noise is Gaussian, as many as observations necessary in transfer function form need to be arithmetically averaged as shown:

$$\begin{aligned} H_{avg}(f) &= \frac{1}{n} \sum_{i=1}^n (H_i(f)) \\ &= \frac{1}{n} (H_1(f) + H_2(f) + \dots + H_n(f)) \end{aligned} \quad (3.29)$$

where H_i is the transfer function from i th impact test and H_{avg} is the averaged transfer function. At this point, optionally, to increase performance of ERA in obtaining minimum realization, higher frequencies of the transfer function can be rejected by simply narrowing down the bandwidth. Consequently, the resulting transfer function will have less information, however with no more high frequency content noise and uninterested modes. Finally, a noiseless IRF based on H_{avg} can be regenerated by Inverse Fast Fourier Transformation (IFFT).

3.3 Model Updating

As explained before, using ERA, a state-space model of the structure can be generated based on measured quantities. This state-space representation also contains dynamic characteristic of the identified structure, i.e. natural frequencies, damping ratios and mode shapes. On the other hand, the ERA-obtained states do not contain any physical information of the structure that is not measured. Consequently, a feedback control algorithm relying on unmeasured structural responses cannot be developed since those remain unobservable. To overcome this disadvantage of the ERA, [Giraldo et al. \(2004\)](#) proposed a model

updating method where experimental results are combined with an analytical model. According to this approach, the stiffness and damping matrices are modified using identified natural frequencies and damping ratios as given below:

$$[K_E] = M_A \Phi_A [2\pi f_E] \Phi_A^T \quad (3.30a)$$

$$[C_E] = M_A \Phi_A (2\xi_E [2\pi f_E]) \Phi_A^T \quad (3.30b)$$

where M_A , K_E and C_E are analytical mass matrix, experimentally-modified stiffness and damping matrices, respectively. f_E and ξ_E represents diagonal matrix of ERA identified natural frequencies in Hertz and damping ratios, respectively. Analytical modal matrix, Φ_A is taken as M_A -mass normalized eigenvectors of $M_A^{-1}K_A$ where K_A is the analytical stiffness matrix. Although this method produces accurate model for control design purposes, resulting model may not always accurately capture the zeros of the experimental transfer functions. A clear reason for the poor zero tracking is because the model updating method uses eigenvectors of the analytical model. If the real eigenvectors of the structure deviate from eigenvectors, Φ_A of the analytical model, the modeling error may lead to low quality models, thus, semi-active controllers with lowered performance or even unstable active controllers. To overcome this problem, a new model-updating methodology promising better zeros-tracking is necessary. The proposed method herein uses mode shapes identified by ERA process. A straightforward application of modal updating based on the use of identified mode shapes can be written as below:

$$[K_E] = M_A \Phi_E [2\pi f_E] \Phi_E^T \quad (3.31a)$$

$$[C_E] = M_A \Phi_E (2\xi_E [2\pi f_E]) \Phi_E^T \quad (3.31b)$$

where Φ_E is ERA identified eigenvector matrix of the structure.

However, in most cases, since eigenvector, Φ_E will not be M_A -orthogonal (i.e. $\Phi_{E_i}^T M_A \Phi_{E_i} = 1$ where Φ_{E_i} is the i th column of Φ_E), the resulting matrices will not be symmetric. Although K_E and C_E trace zeros very successfully, their asymmetry does not reconcile with the Maxwell's Reciprocal Theorem. In order to symmetrize K_E and C_E , M_A needs to be modified in such a way that, Φ_E will be M_E -orthogonal, where M_E is the updated mass matrix of the system. At the same time, for the sake of the problem, M_E needs to be as similar as possible to M_A , so that M_E will still comply with initial modeling assumptions. Then, the objective function is minimizing the quadratic error between M_A and M_E as given below:

$$\min[\text{vec}(M_E - M_A)^T W \text{vec}(M_E - M_A)] \quad (3.32)$$

subject to

$$M_E = Z_E^T D_E Z_E \quad (3.33)$$

$$Z_E = \Phi_E^{-1} \quad (3.34)$$

where vec is the vectorization operation, Z_E is the inverse of Φ_E as given in Eq. (3.34), W is the weighting matrix and D_E is a diagonal matrix to be found as a solution to the minimization problem given in Eq. (3.32). Weighting vector W can be adjusted to give more weight to the elements that need to be minimized.

Note that, Eqs. (3.33) and (3.34) also lead us to the flowing formula:

$$\Phi_E^T M_E \Phi_E = D_E \quad (3.35)$$

After finding D_E , the mass matrix, M_E can be produced from Eq. (3.33). Finally, by rewriting Eqs. (3.31a) and (3.31b), updated stiffness and damping

matrices, K_E and C_E can be obtained as follows:

$$[K_E] = M_E \Phi_E [2\pi f_E] \Phi_E^T \quad (3.36a)$$

$$[C_E] = M_E \Phi_E (2\xi_E [2\pi f_E]) \Phi_E^T \quad (3.36b)$$

It should be noted that Eq. (3.36) allows fine-tuning of mode shapes as well as natural frequencies and damping ratios, in case those parameters are not accurately identified using ERA.

The model updating methodology explained above is implemented and automated in MATLAB. To solve the minimization problem, *fminunc*, unconstrained nonlinear optimization function already implemented in MATLAB is used.

3.4 Limitations of the Proposed Method

Although this method supersedes the previous model updating method in various ways, it has some incompetencies either inherited from its predecessor or due to implications regarding implementation.

It has been observed that the model updating methodology may introduce small off-diagonal terms in the lumped mass matrix up to 1% of the diagonal terms. Since the updated mass matrix is not diagonal anymore, the inverse of mass matrix is not going to be diagonal. Eventually, off-diagonal terms of M^{-1} will leak in B , D and E vectors. Although the leakage does not impose any problem, it should be noted that for a system presented in Eqs. (3.4) to (3.8), force applied at first floor will affect all internal states related to its relative accelerations, even if initial conditions are zero. A similar behavior is observed also for the systems modeled with consistent mass matrix.

The proposed method can yield symmetric matrices that comply with direct

stiffness method, albeit, the results will not be in band matrix form with a band-width of three like shown in Eqs. (3.2b) and (3.2c). Thus, stiffness and damping of individual floors cannot be extracted. One potential impact of this issue is not being able to calculate exact shear force at floor level.

3.5 Evaluation Criteria

A set of criteria is developed to understand:

- the effectiveness of numerical model in simulating reference structure responses on the shake table
- the performance of RTHS conducted at Purdue to simulate reference structure responses

Focusing on global structural performance, evaluation criteria are concentrated on peak, root mean square (RMS) responses and moving RMS responses. Relative displacement and absolute acceleration responses are selected as the basis of comparison for two cases mentioned above. The performance indices are prepared such that smaller values indicate better performance. A summary of these criteria is presented in Table 3.1. Here, x_i and \ddot{x}_i represent displacement relative to the ground and absolute acceleration at i th floor. Definition for *RMS* of an arbitrary discrete signal, x is given as:

$$RMS(x) = \sqrt{\frac{1}{n} \sum_{i=1}^n (x_i - \bar{x})^2} \quad (3.37)$$

Likewise, RMS error between two arbitrary signals, x and y , is calculated as:

$$RMS(x - y) = \sqrt{\frac{1}{n} \sum_{i=1}^n (x_i - y_i)^2} \quad (3.38)$$

To calculate moving RMS error, a window of length τ is slid until the end of the signal. Therefore, this index is a function of time. Since RMS with sliding window is computationally demanding when implemented in loop form, convolution is used to compute the moving average of the squared signal.

3.6 Results

To perform model verification, the structure is identified experimentally at HIT and the results of the model updating technique are compared to the shake table response.

3.6.1 Initial Model

An initial model of the test structure based on the information provided in Sections 2.1 and 3.1 is established as the baseline model.

The following assumptions are made for the baseline model:

- Each column is assumed to have fixed-fixed connection with identical stiffness of $12EI/L^3$.
- E , Young's modulus of structural steel is equal to 220 GPa.
- I , moment of inertia of a single column in weak-axis is equal to 10.2 cm^4 .
- L , length of the column is equal to 1.2 m.
- Damping ratio, ξ for all of the structural modes is assumed to be 0.5%.
- Each story is supported by four columns.
- Structural masses and concrete slabs are lumped to the nodes.

Table 3.1: List of Evaluation Criteria

Index #	Equation	Description
J1	$\frac{RMS(x_{i, \text{actual}}(t) - x_{i, \text{reference}}(t))}{RMS(x_{i, \text{reference}}(t))}$	Normalized RMS Floor Displacement Error Ratio of RMS error between actual and reference value to the RMS reference value
J2	$\frac{x_{i, \text{actual}}^{max} - x_{i, \text{reference}}^{max}}{x_{i, \text{reference}}^{max}}$	Peak Floor Displacement Error Ratio of error between peak actual and peak reference value to the peak reference value
J3	$\frac{RMS(\ddot{x}_{i, \text{actual}}(t) - \ddot{x}_{i, \text{reference}}(t))}{RMS(\ddot{x}_{i, \text{reference}}(t))}$	Normalized RMS Floor Acceleration Error Ratio of RMS error between actual and reference value to the RMS reference value
J4	$\frac{\ddot{x}_{i, \text{actual}}^{max} - \ddot{x}_{i, \text{reference}}^{max}}{\ddot{x}_{i, \text{reference}}^{max}}$	Peak Floor Acceleration Error Ratio of error between peak actual and peak reference value to the peak reference value
J5	$\frac{RMS(x_{i, \text{actual}}(t) - x_{i, \text{reference}}(t))}{x_{i, \text{reference}}^{max} - x_{i, \text{reference}}^{min}}$	RMS Floor Displacement Error divided by the range Ratio of RMS error between actual and reference value to the difference of the maximum and minimum value
J6	$\frac{RMS(\ddot{x}_{i, \text{actual}}(t) - \ddot{x}_{i, \text{reference}}(t))}{\ddot{x}_{i, \text{reference}}^{max} - \ddot{x}_{i, \text{reference}}^{min}}$	RMS Floor Acceleration Error divided by the range Ratio of RMS error between actual and reference value to the difference of the maximum and minimum value
J7	$\left[\frac{RMS(x_{i, \text{actual}}(t) - x_{i, \text{reference}}(t))}{RMS(x_{i, \text{reference}}(t))} \right]_{\tau}$	Moving RMS Floor Displacement Error Ratio of RMS error between actual and reference value to the RMS reference value in a time window
J8	$\left[\frac{RMS(\ddot{x}_{i, \text{actual}}(t) - \ddot{x}_{i, \text{reference}}(t))}{RMS(\ddot{x}_{i, \text{reference}}(t))} \right]_{\tau}$	Moving RMS Floor Acceleration Error Ratio of RMS error between actual and reference value to the RMS reference value in a time window

Using the assumptions stated above, the baseline model can be formed as:

$$[M] = \begin{bmatrix} 400.1 & 0 & 0 \\ 0 & 355.3 & 0 \\ 0 & 0 & 355.3 \end{bmatrix} \text{ kg} \quad (3.39a)$$

$$[C] = \begin{bmatrix} 211.1 & -60.5 & -13.6 \\ -60.5 & 187.4 & -71.1 \\ -13.6 & -71.1 & 128.5 \end{bmatrix} \text{ N sec/m} \quad (3.39b)$$

$$[K] = \begin{bmatrix} 1222.2 & -611.1 & 0 \\ -611.1 & 1222.2 & -611.1 \\ 0 & -611.1 & 611.1 \end{bmatrix} 10^3 \text{ N/m} \quad (3.39c)$$

The estimated natural frequencies are calculated 2.92 Hz, 7.96 Hz and 11.62 Hz.

3.6.2 System Identification: Identified Parameters

A general block diagram of the structure to be identified is shown in Fig. 3.6. Here, \ddot{x}_g is the disturbance as the ground motion to the system, f_1 is the input force applied at the first floor, also where the MR damper device will be connected, and x_i , \dot{x}_i , \ddot{x}_i are the relative displacement to the ground, relative velocity to the ground, and absolute acceleration of i^{th} floor, respectively.

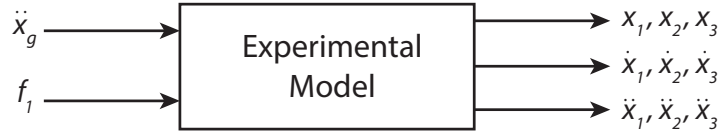


Figure 3.6: Block Diagram of the Structure to be Identified

Structure is identified with an impact hammer by hitting to its first floor and recording the resulting acceleration responses. Due to the limited number of

sensors available, multiple tests were performed. Thus, three sensors are used in each test to measure the accelerations at various locations in the weak direction. The tests are categorized based on the sensor placements at north side, mid point and south side as given in Fig. 3.7. At each trial, 25 hits, each having up to 60 sec time window, are performed on the mid point of the girder at the first floor. For each set of data, including the hammer force, 4 channels are sampled at 3000 Hz. For all acceleration and hammer force sensors, 0.3 Hz and 300 Hz are selected as low pass filter and high pass filter, respectively. Curious readers can access the impact test data from the NEES Project Warehouse ([Ozdogli et al., 2013a,b](#)).

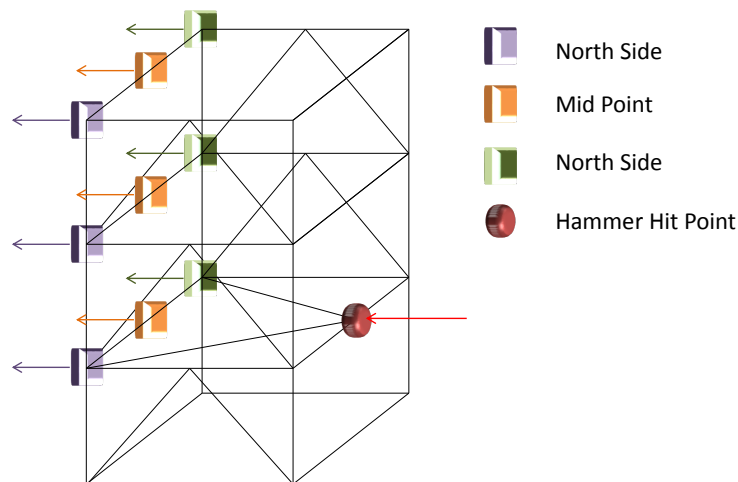


Figure 3.7: Sensor and Hit Location Layout

After the data is collected, post-processing is conducted involving dividing each impact responses into individual time histories associated with the hammer force response. A decaying exponential window of 1% to the structural responses is applied to the structural responses. Transfer functions are generated from force to acceleration for all successful hits and averaging is performed in order to increase signal to noise ratio and eliminate structural nonlinearities. Using

the averaged transfer functions, impulse response functions are developed. After impulse functions are bounded to 0 Hz to 40 Hz, ERA procedure has been applied on each trial individually. 500 columns and 1500 rows with a singular value of 25 are selected as the input parameters to ERA. Finally, 11 modes are identified in the system. However, only first three modes are used since higher modes are mainly associated with the torsional movement of the structure. The identified modes and damping ratios are determined as 2.88 Hz, 8.10 Hz and 12.34 Hz; 0.57 %, 0.21 % and 0.15 %, respectively. For each ERA application, EMAC numbers yielded over 95 %. Transfer functions and phase diagrams of experimental data are compared to those generated with ERA in Figs. 3.8 and 3.9. The identified mode shapes for each identified mode are represented in Fig. 3.10.

As seen from comparisons and identified mode shapes, there is no significant difference between results. However, since ERA results of mid-point accelerations have better estimations on the zeros, it is decided to place the accelerometers to the mid-point for further shake table tests.

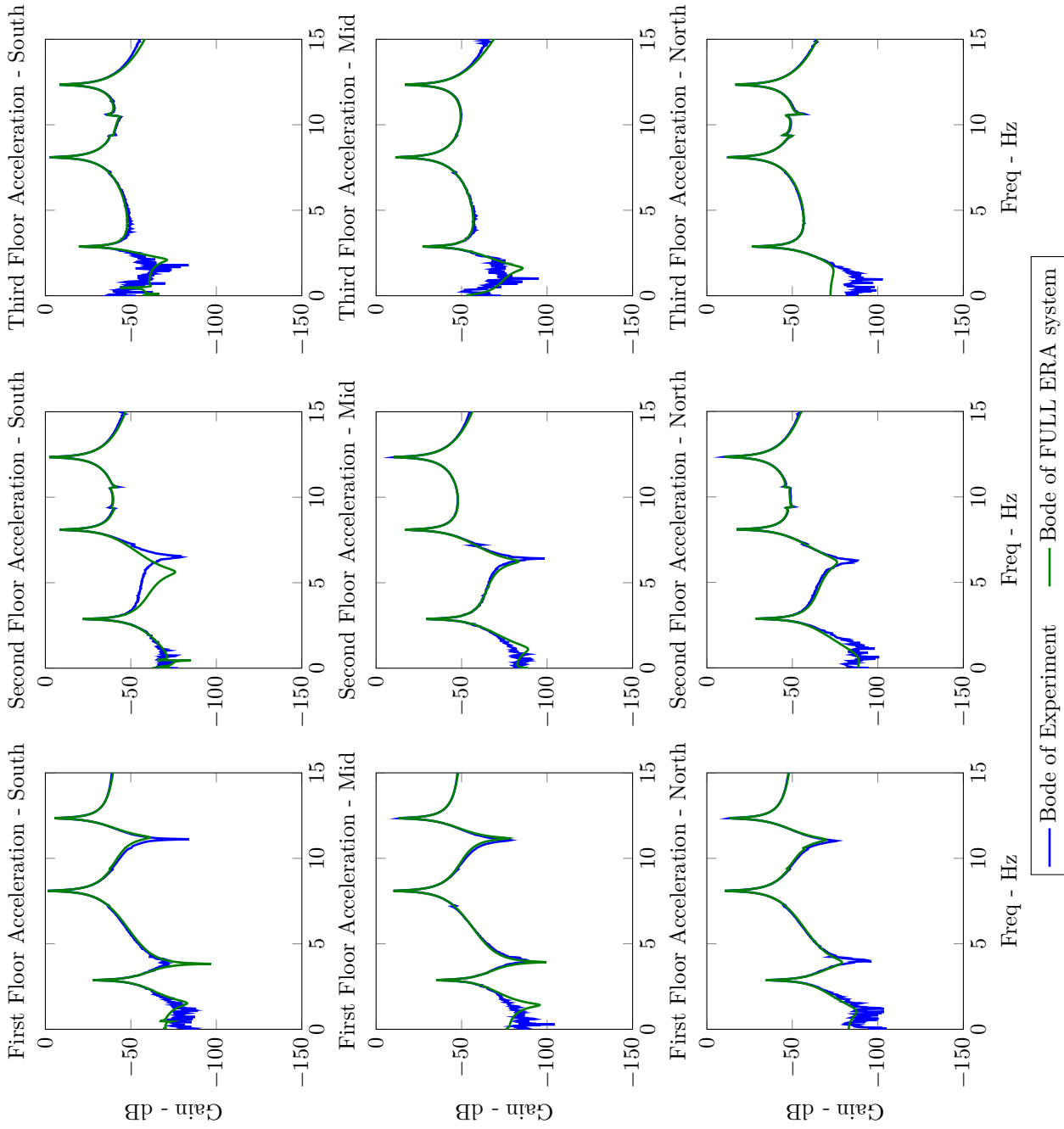


Figure 3.8: Transfer Function Comparison between Experimental Data vs ERA Data

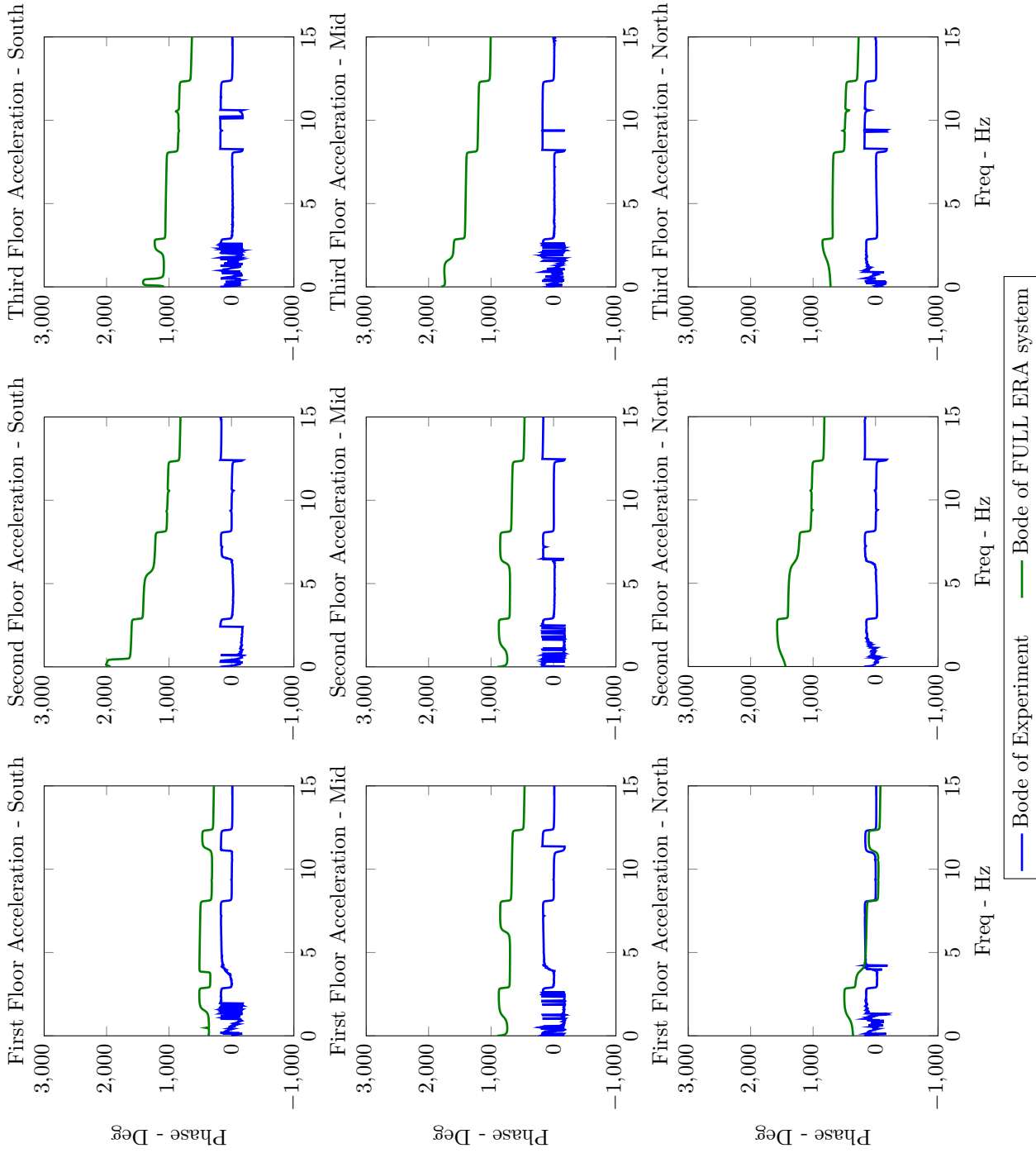


Figure 3.9: Phase Diagram Comparison between Experimental Data vs ERA Data

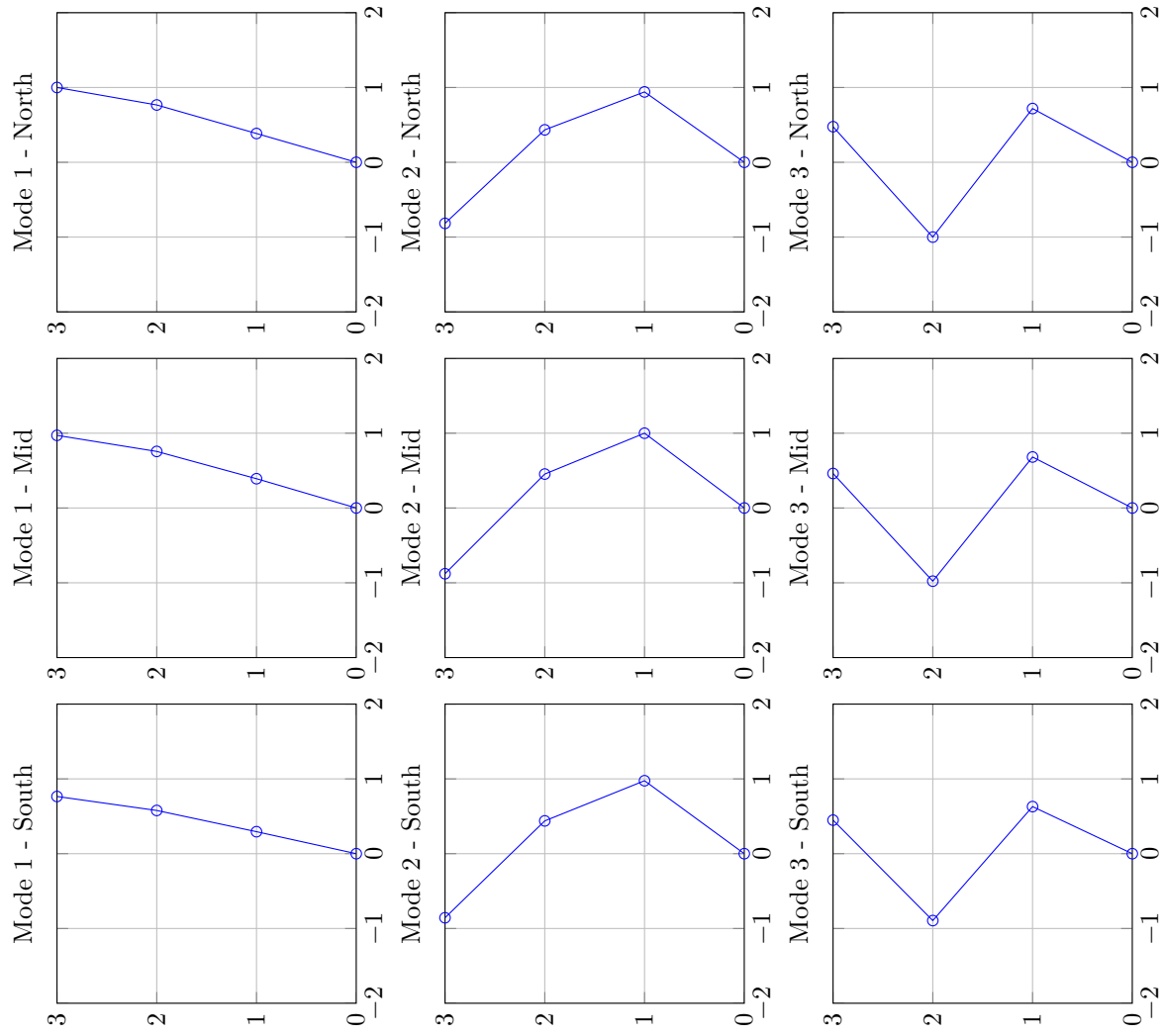


Figure 3.10: Identified Mode Shapes of the First Three Identified Modes

3.6.3 Comparison of Model Updating Methods

Two model updating methodologies have been discussed previously in Section 3.3. According *CK* updating method (Eq. (3.30)), the following matrices are formed:

$$[M] = \begin{bmatrix} 400.1 & 0 & 0 \\ 0 & 355.3 & 0 \\ 0 & 0 & 355.3 \end{bmatrix} \text{ kg} \quad (3.40a)$$

$$[C] = \begin{bmatrix} 101.6 & 3.3 & 3.8 \\ 3.3 & 93.3 & 6.2 \\ 3.8 & 6.2 & 96.2 \end{bmatrix} \text{ N sec/m} \quad (3.40b)$$

$$[K] = \begin{bmatrix} 1316.4 & -703.8 & 30.5 \\ -703.8 & 1357.1 & -680.2 \\ 30.5 & -680.2 & 649.8 \end{bmatrix} 10^3 \text{ N/m} \quad (3.40c)$$

For the *MCK* update method (Eq. (3.36)), there are 9 components, each corresponding to an element in *M* matrix. Given a weighting vector, *W* in the form of *I*₉, the identified *MCK* system based on the identified parameters is

given as:

$$[M] = \begin{bmatrix} 419.1 & 2.6 & 2.4 \\ 2.6 & 359.1 & 10.1 \\ 2.4 & 1.1 & 325.9 \end{bmatrix} \text{ kg} \quad (3.41a)$$

$$[C] = \begin{bmatrix} 91.4 & -1.7 & 0.3 \\ -1.7 & 75.23 & -0.1 \\ -0.1 & -0.1 & 69.0 \end{bmatrix} \text{ N sec/m} \quad (3.41b)$$

$$[K] = \begin{bmatrix} 1446.7 & -726.0 & 44.7 \\ -726.0 & 1299.6 & -615.9 \\ 44.72 & -609.3 & 552.3 \end{bmatrix} 10^3 \text{ N/m} \quad (3.41c)$$

Readers should note that all matrices from *CK* and *MCK* methods are symmetric but have small off-diagonal terms that are not larger than 10% of diagonal elements.

Transfer functions of experimental data collected from mid-point accelerometers upon impact, initial analytical model estimation and updated models are compared in Fig. 3.11.

As seen from the figures, it is evident that the proposed *MCK* updating method is superior not only in capturing zeros but also peaks, compared to *CK* updating method.

3.6.4 Model Verification

For the validation of the model, structural responses of the seismically excited, uncontrolled system are compared to updated model. El Centro, Kobe and Morgan Hill earthquakes explained in Section 2.3.3 are chosen as the disturbance

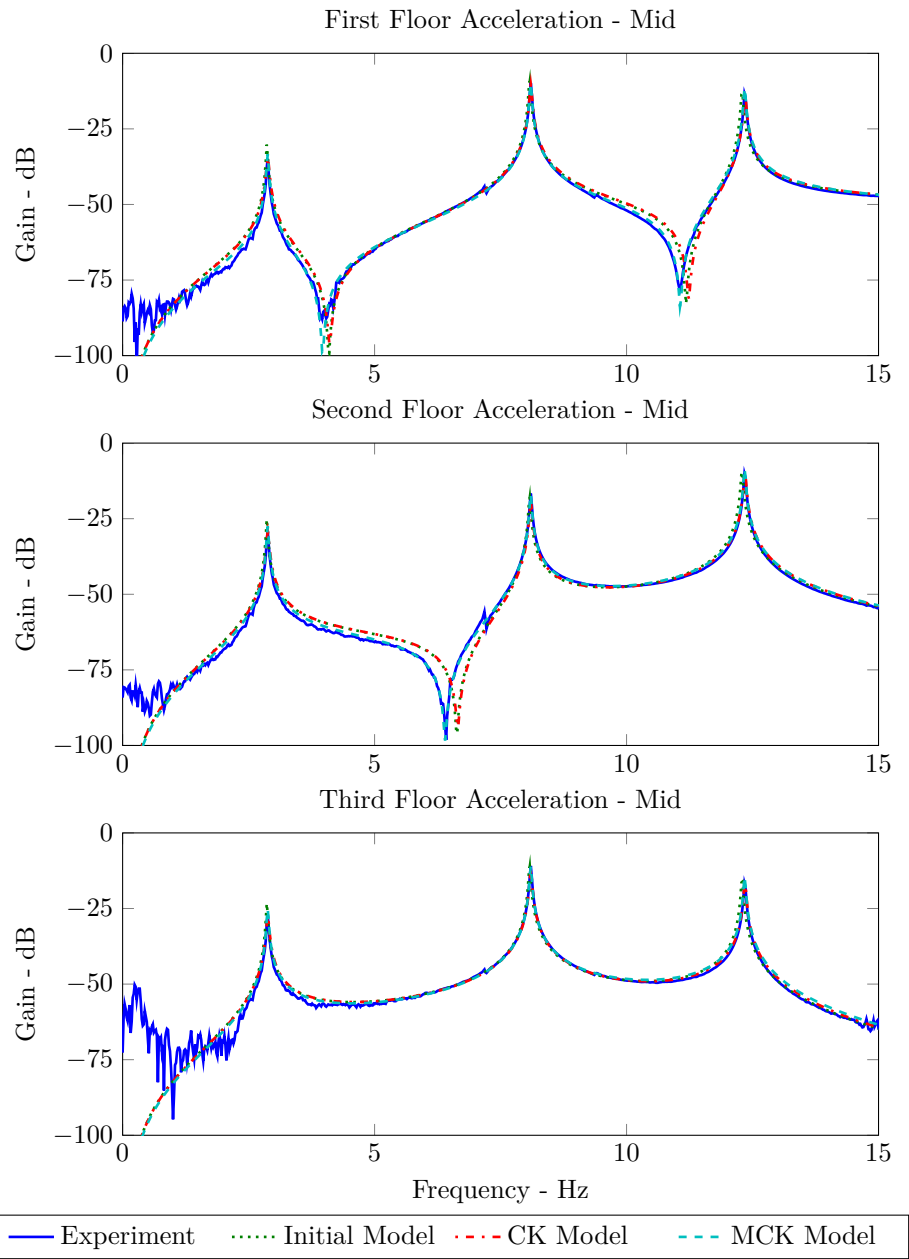


Figure 3.11: Transfer Function Comparison between Experimental Data and Updated Models

(Fig. 3.6). The simulated earthquake motion measured on the shake table by accelerometers is used as the input to the analytical simulation of the model given in Eq. (3.41). For the basis of the comparisons, the experimental displacement and acceleration records are compared to analytical simulation responses. Experiments and simulations, both are conducted at a rate of 5000 Hz.

The comparison plots are given in Figs. 3.12 to 3.14. RMS and peak response errors are tabulated in Table 3.2. Only the first 25 seconds of data is processed to calculate the given errors. All values are given as percentages.

From Table 3.2, it is reported that average peak error of floor accelerations and displacements are ranging from 6 % to 8 %. For the RMS response categories, the average error is varying from 10 % to 14 %. The overall criteria average yields about 10 % error for all three earthquakes.

Among three earthquakes, largest RMS error has occurred during Kobe earthquake both for displacement and accelerations. Similarly, largest peak displacement and acceleration errors are reported for the Morgan Hill earthquake.

It is natural that systems having been identified based on impact testing parameters may behave differently when excitation input used for the model validation is a different source, e.g. ground motion. Dynamic characteristic of the system in time domain is often ignored while frequency domain processes linearize the system that contains small local nonlinearities and other dynamic impurities such as out-of-plane movements or torsion.

After all, a model is a mathematical explanation of the system it represents. User requirements define a basis for the assumptions made to eliminate discretizations at the expense of modeling inaccuracies. Development of a computationally inexpensive model due to time constraints of hard real-time simulation is a major requirement for this study.

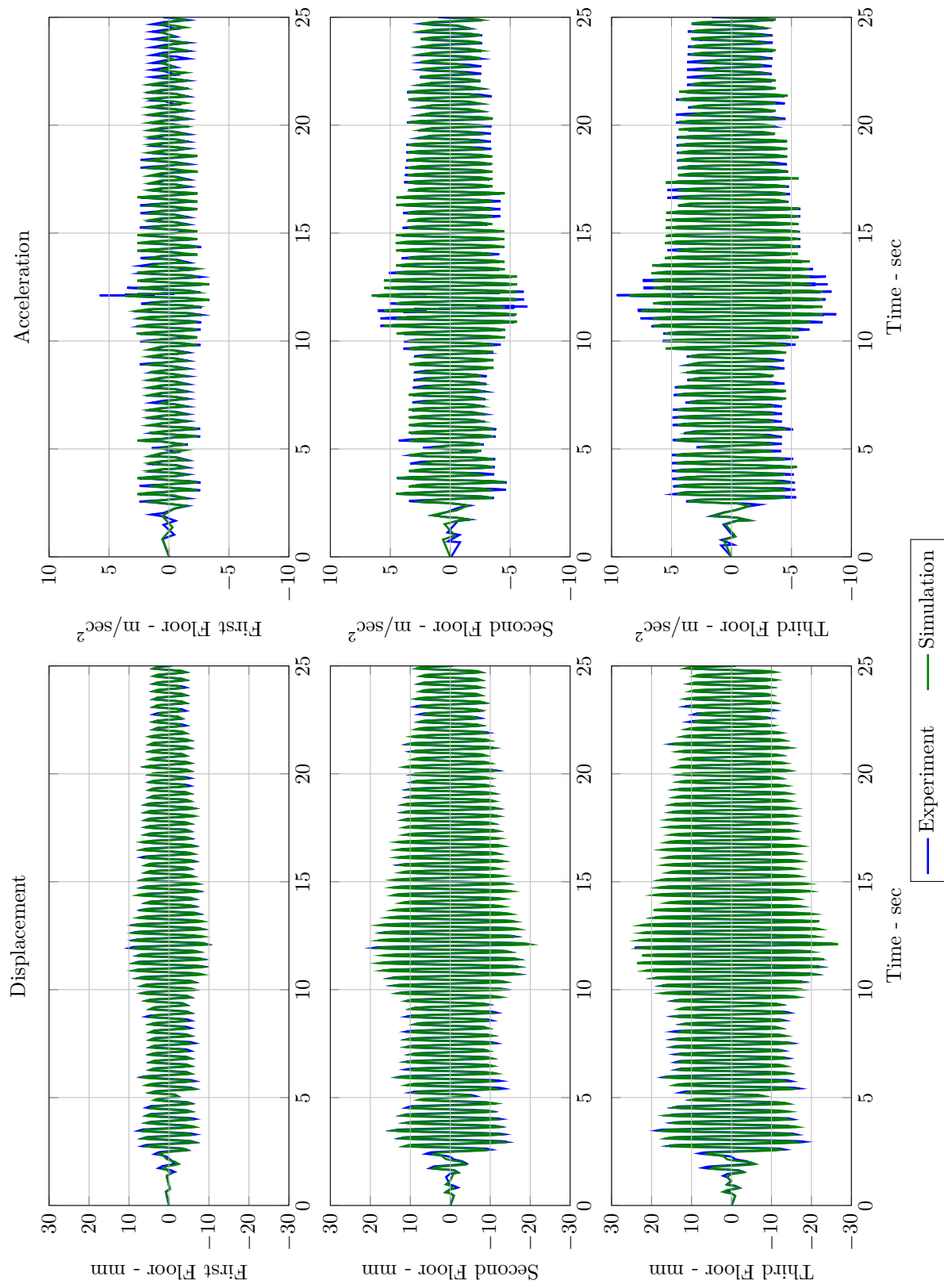


Figure 3.12: El Centro Earthquake Comparison

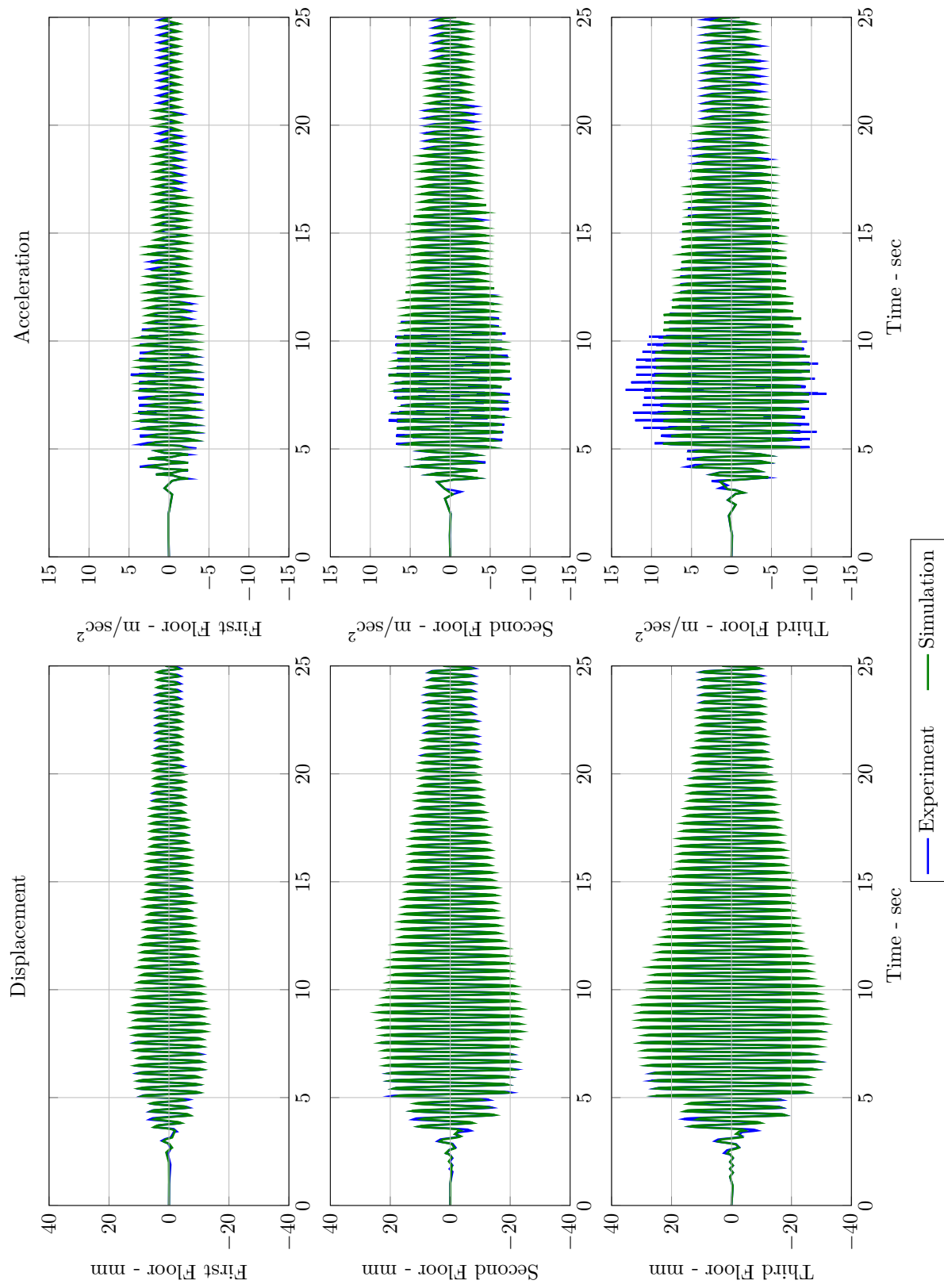


Figure 3.13: Kobe Earthquake Comparison

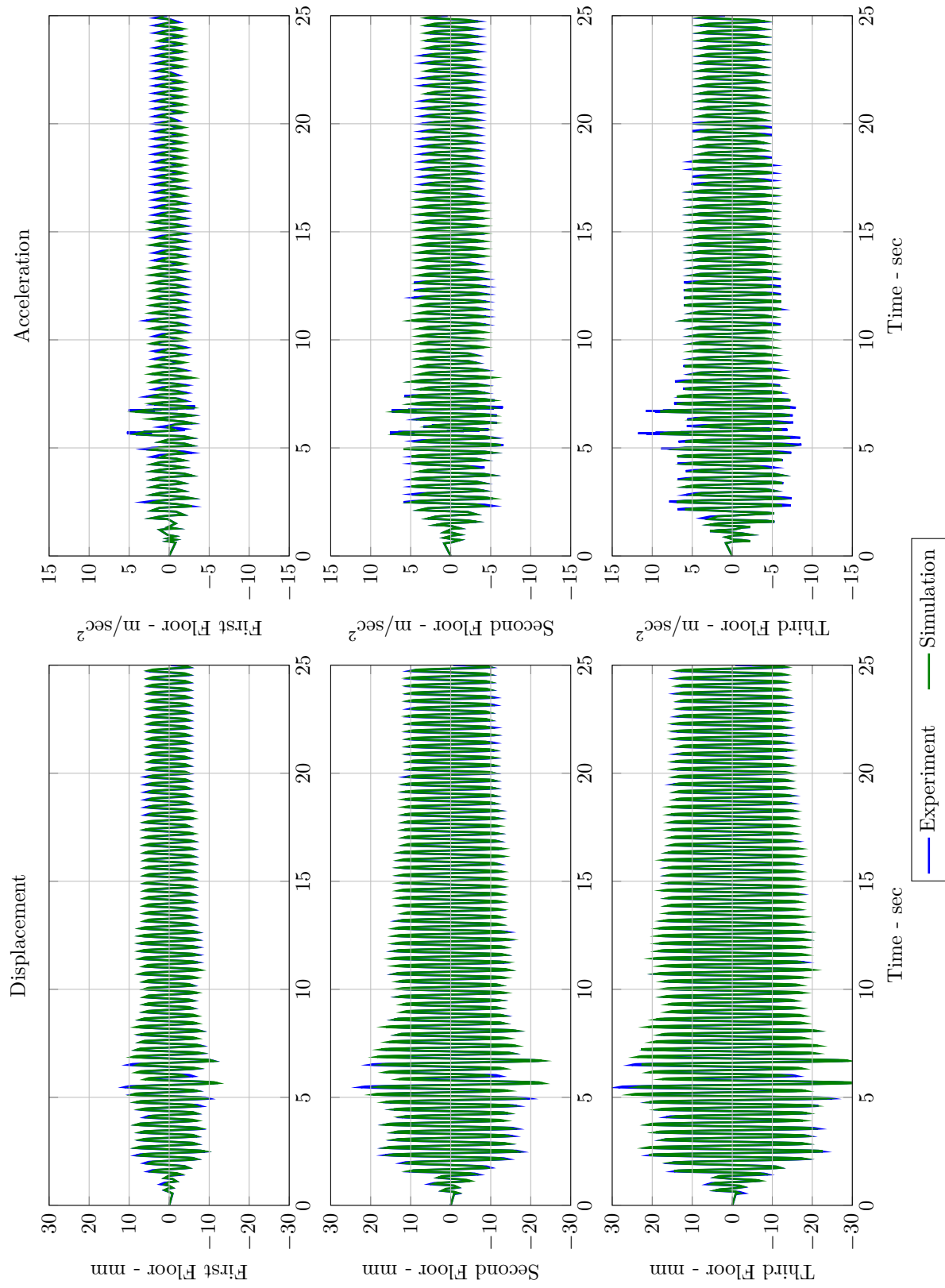


Figure 3.14: Morgan Hill Earthquake Comparison

Table 3.2: Evaluation Criteria for Model Verification

Ground Motion	Location	Evaluation Criteria				Criteria Average
		J1	J2	J3	J4	
El Centro	First Floor	8.17	12.08	0.65	15.25	9.04
	Second Floor	4.81	10.92	1.22	10.21	6.79
	Third Floor	1.54	11.46	1.56	10.07	6.16
Kobe	First Floor	5.14	13.85	4.09	17.31	10.10
	Second Floor	2.71	14.80	10.16	14.45	10.53
	Third Floor	4.82	16.23	1.58	12.98	8.91
Morgan Hill	First Floor	10.95	10.70	10.68	9.28	10.40
	Second Floor	13.19	11.07	0.20	7.41	7.97
	Third Floor	11.84	11.24	5.96	7.79	9.21
EQ Average	First Floor	8.09	12.21	5.14	13.95	9.85
	Second Floor	6.90	12.26	3.86	10.69	8.43
	Third Floor	6.07	12.98	3.03	10.28	8.09

3.7 Conclusion

To validate RTHS with experimental data and pure analytical simulations, an accurate model of the test structure is necessary. In this chapter, theoretical background on system identification via dynamic impact hammer testing and novel MCK model updating methodology based on identified structural parameters are described. To verify the proposed updating method, the test structure is excited using shake table when no MR damper device is attached and the global responses of the system to several ground motions were compared to those of pure numerical model.

Overall, the new model updating method has proven to be superior compared to its predecessors for estimating non-observable states while relying completely on identified structural characteristics.

CHAPTER 4

MAGNETO-RHEOLOGICAL DAMPER CHARACTERIZATION AND SEMI-ACTIVE VIBRATION CONTROL DESIGN

In this chapter, an overview of the magneto-rheological damping device is given including its working principle, modeling and control in a semi-active control setting. Section 4.1 presents a brief background on vibration control and the development idea behind semi-actively controllable devices. Section 4.2 explains behavior characterization and modeling procedure of the MR dampers used at HIT and IISL for this study. In addition, this chapter discusses the main differences of physics in HIT and Purdue damper and prescribes a method to describe one damper in terms of the other one, mathematically. In Section 4.3, the theory behind a common semi-active controller, clipped-optimal control

algorithm is introduced, including its implementation. Finally, a summary of this chapter is presented.

4.1 Introduction

The seismic performance of a building is related to the damage and loss its structural and non-structural elements can take during an earthquake (Deierlein et al., 2010). Although aseismic design practices improve perseverance of civil structures and reduce life loss significantly by sacrificing non-structural elements, severe economic losses may be still inevitable considering dynamic nature of ground motions (Constantinou et al., 1998). ASCE (2007) provides a guideline on three performance levels: Immediate Occupancy; Life Safety; and Collapse Prevention. By separating structural frame from energy dissipative structural elements and adding vibration control devices, an improvement in the safety level of buildings can be achieved.

Roots of vibration control reach back to 1972 with the conceptual introduction by Yao (1972). From this date forward, the evolution of the civil engineering field in structural control has been rapid, attracting many researchers for decades and the topic still continues to mature (Housner et al., 1997). Among vibration control devices currently available on the market, passive damping devices are often considered as the first solution to control structural vibration since they can dissipate energy directly by increasing the damping of the structure. As an example to this device category, passive base isolation systems for seismic protection have become an accepted design strategy in low- and medium-rise buildings, in US and worldwide (Kelly and Konstantinidis, 2011). Even though those devices are commonly used in the practice, they may not be, in fact, effective for every type of excitation, especially where stochastic nature of the input governs its overall behavior (Chang et al., 2009). To overcome the limitations

of passive devices, active control strategies have been developed. Essentially, active devices can adapt themselves to the excitation and structural responses by imposing external forces supplied by actuators (Spencer and Nagarajaiah, 2003). For successful operation of those devices, uninterrupted power source for actuation and computer systems, that monitor structural responses and enforce command to these devices based on a predefined control strategy, are needed. An extensive study on the effectiveness of this device type is explored by Dyke (1996) and Loh et al. (2007).

As a major drawback, the active control device may be ineffective or at risk of becoming unstable in such cases where uncertainties and disturbances in the system affect structural integrity. To ensure a fail safe operation of control system and still to minimize the structural vibration, a new generation of control devices have been developed. Namely, semi-active devices that combine best features of passive and active control system offers a great range of adaptability and reliability (Soong and Spencer, 2002). By nature, a semi-active device is a controllable passive device. By using small amount of external power of ≈ 100 W, system's stiffness and damping characteristics can be modified via control signal tuned according to structural responses, and system can *consume* the motion of the structure to develop control forces. Since the device cannot increase mechanical energy in the structure, bounded input - bounded output stability is guaranteed during the operation. Moreover, in the event of loss of power due to impact loads caused by earthquakes, the system can still rely on its passive damping features.

Vibration control using semi-active force generators dates back to 1974 (Karnopp et al., 1974). Among many semi-active devices developed so far, MR fluid dampers have received a lot of attention due to their reliability and adaptability, in the last decade. A typical MR damper contains a special type of

fluid called MR fluid that consists of a suspension of micron-sized magnetic iron particles that can be controlled with the help of magnetic field. By exposing to the magnetic field, the viscous MR fluid can turn into a semi-solid state instantly and generate large amount of resisting forces, as shown in Fig. 4.1. Since an appropriate magnetic field can be imposed with a very small amount of electrical current, MR dampers are counted as sustainable devices. Combining high reliability with meager power consumption, the MR damper becomes a strong candidate for vibration control applications. An illustration of MR damper is provided in Fig. 4.2.

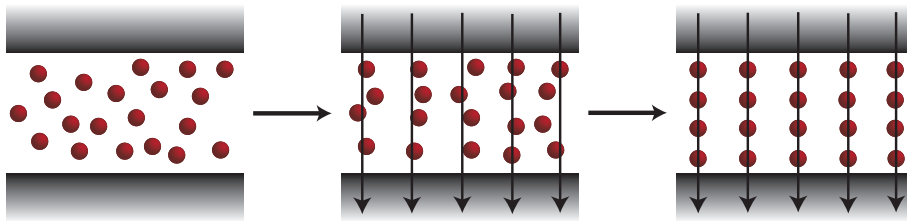


Figure 4.1: Particulate Alignment in MR fluid

Pilot studies conducted by [Dyke et al. \(1996b\)](#) and [Johnson et al. \(1998\)](#) demonstrated through laboratory experiments that MR damper can reduce seismic response of structures compared to passive configurations. In addition, the success of this novel technology has been proven in small-scale mechanical systems such as vehicular suspension by [Karkoub and Zribi \(2006\)](#) and large-scale civil engineering structures as in Dongting Lake Cable-stayed Bridge, China by [Chen et al. \(2003\)](#) and National Museum of Emerging Science and Innovation, Tokyo. To persuade contractors, especially in US, hesitant to apply MR damper technology on current structures and future designs, many research projects nationwide are focused on investigation of the effectiveness of MR dampers and development of appropriate design procedures ([Friedman et al., 2010](#); [Jiang and Christenson, 2011](#); [Phillips and Spencer, 2013](#)).

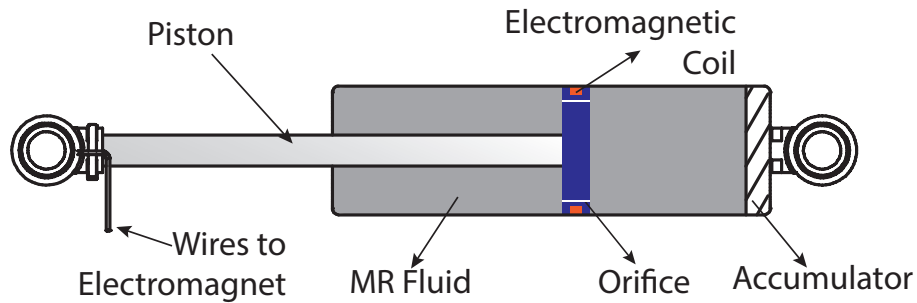


Figure 4.2: MR Damper Internals

4.2 Damper Identification and Modeling

MR dampers are highly nonlinear devices and their force-velocity relationship shows a hysteretic behavior that cannot be easily represented using simple mathematical relationships (Zapateiro de la Hoz, 2009). There has been serious effort on modeling of MR damper hysteresis to ease the implementation and performance evaluation of new controllers and to simulate the behavior in numerical analyses and real-time hybrid simulations where experimentation in full-scale is not possible. As for damper models, there exists two mainstream models: parametric and non-parametric. While parametric models are developed loosely based on mechanical properties of the damper, non-parametric models do not have a physical ground (Sahin et al., 2010). A tree of known models are listed in Fig. 4.3. The report will focus on a member of parametric model family, the phenomenological Bouc-Wen model introduced by Dyke et al. (1996b) and Spencer et al. (1997).

4.2.1 Modeling of the MR Damper

A phenomenological MR damper was proposed by Spencer et al. (1997). This model, which combines Bouc-Wen equations proposed by Bouc (1971) and Wen

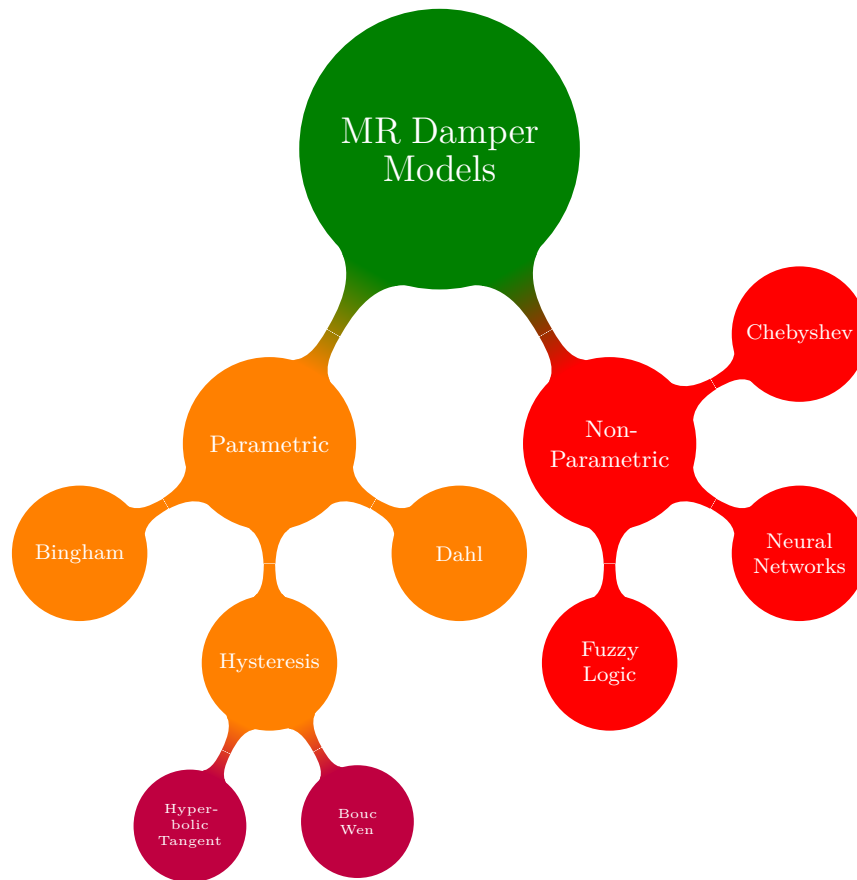


Figure 4.3: MR Damper Models

(1976) with a series of springs and dashpots in parallel, was sufficient in simulating dynamics of prototype dampers by Lord Corp. A mathematical idealization of this model is shown in Fig. 4.4. In addition, a simplified version of Bouc-Wen model was developed by Dyke et al. (1996b) with the aim to portray force-velocity characteristics of a specific MR damper family more accurately. This report will focus on the complex MR damper model.

According to phenomenological Bouc-Wen model, an MR damper can be

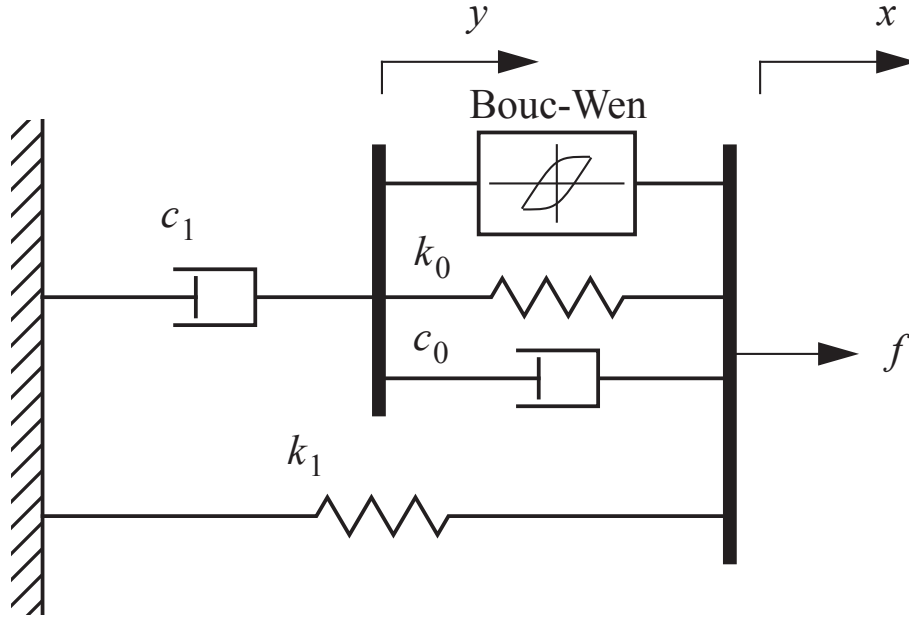


Figure 4.4: Phenomenological Bouc-Wen Hysteresis Model of the MR Damper

characterized by the following equations:

$$c_1 \dot{y} = \alpha z + k_0(x - y) + c_0(\dot{x} - \dot{y}) \quad (4.1a)$$

$$\dot{z} = -\gamma |\dot{x}_d - \dot{y}| |z|^{n-1} - \beta (\dot{x}_d - \dot{y}) |z|^n + A(\dot{x}_d - \dot{y}) \quad (4.1b)$$

$$F = \alpha z + c_0(\dot{x} - \dot{y}) + k_0(x - y) + k_1(x - x_0) \quad (4.1c)$$

where F represents the total damper force, k_1 represents the accumulator stiffness, c_0 represents the viscous damping observed at larger velocities, c_1 produces roll-off at low velocities, k_0 controls the stiffness at large velocities and x_0 is the initial displacement of spring, k_1 .

For a passive damper system, where voltage kept constant, identifying the parameters mentioned above is adequate. However, for achieving optimal performance, a semi-active control scheme needs to be implemented through commanding voltage signal using a current driver. In view of that, any change in

voltage will create a fluctuation in the magnetic field. In other words, damping constants given in Eq. (4.1) will vary virtually linearly with the applied voltage. The equations given below reveal this relationship:

$$\alpha(u) = \alpha_a + \alpha_b u \quad (4.2a)$$

$$c_0(u) = c_{0a} + c_{0b} u \quad (4.2b)$$

$$c_1(u) = c_{1a} + c_{1b} u \quad (4.2c)$$

$$\dot{u} = -\eta(u - v) \quad (4.2d)$$

where v and u are the command voltage sent to current driver and filtered voltage, respectively, and η is the lag constant. Eq. (4.2d) can be recognized as a filter that defines a basic model of the current driver and dynamics of MR fluid reaching rheological equilibrium.

Eqs. (4.1) and (4.2) can be implemented as an input-output block or hard-coded inside embedded function block in Simulink/MATLAB ([MATLAB, 2011](#)).

4.2.2 Identification Process

The damper parameters mentioned in the Eq. (4.1) are determined based on characterization tests. In a typical parameter identification process, for each supply voltage level, the damper attached to an actuator is excited with a sinusoidal displacement and damper reaction force is measured. Since MR damper is a nonlinear device, its behavior may change with respect to the frequency and amplitude for the given displacement. Thus, for the sake of best performance in characterization, the frequency and amplitude of the sine wave should be adjusted according to the characteristic dynamics of the test structure, to which damper is going to be attached.

To obtain the parameters related to each voltage supplied to the damper,

lsqcurvefit, nonlinear curve-fitting algorithm is used, which has already been implemented in MATLAB. The identification process should be set up in such a way that different voltage levels should yield same values for k_0 , k_1 , γ , β and A , while varying α , c_0 and c_1 . Since the parameters n , η and x_0 are pre-defined based on damper properties, they are not required to be part of the curve-fit algorithm. Finally, using characterization results and Eq. (4.2), α_a , α_b , c_{0a} , c_{0b} , c_{1a} and c_{1b} are calculated.

4.2.3 Damper Characterization Results

In this section, the identification process explained above are applied to MR dampers located at HIT and IISL/Purdue. The characterization results of those dampers, as well as representation of Purdue damper with HIT damper equations are also given in subsequent sections.

(i) *HIT Damper*

Characterization tests conducted at HIT are performed with MR damper #RD-1005-3 attached to the uniaxial servohydraulic load frame (see Section 2.4). A sinusoidal displacement input with a magnitude of 5 mm at a frequency close to the first mode of the test structure, 2.9 Hz is tested, when the damper is subjected to constant voltage levels of passive-off (0 V) and -on (1.7 V). Since damper characteristics are different between pushing and pulling state, load response is detrended to remove the offset.

The force-time history, force-displacement and force-velocity relationships are given in Fig. 4.5. In Fig. 4.6, comparison between the experimentally obtained responses and the identified Bouc-Wen model is presented. It is observed that the Bouc-Wen model is effective at capturing the damper's behavior. Optimization routine yielding Bouc-Wen model parameters are listed in Table 4.1. A relative

standard deviation error of 15% to 18% is found between experimental data and model.

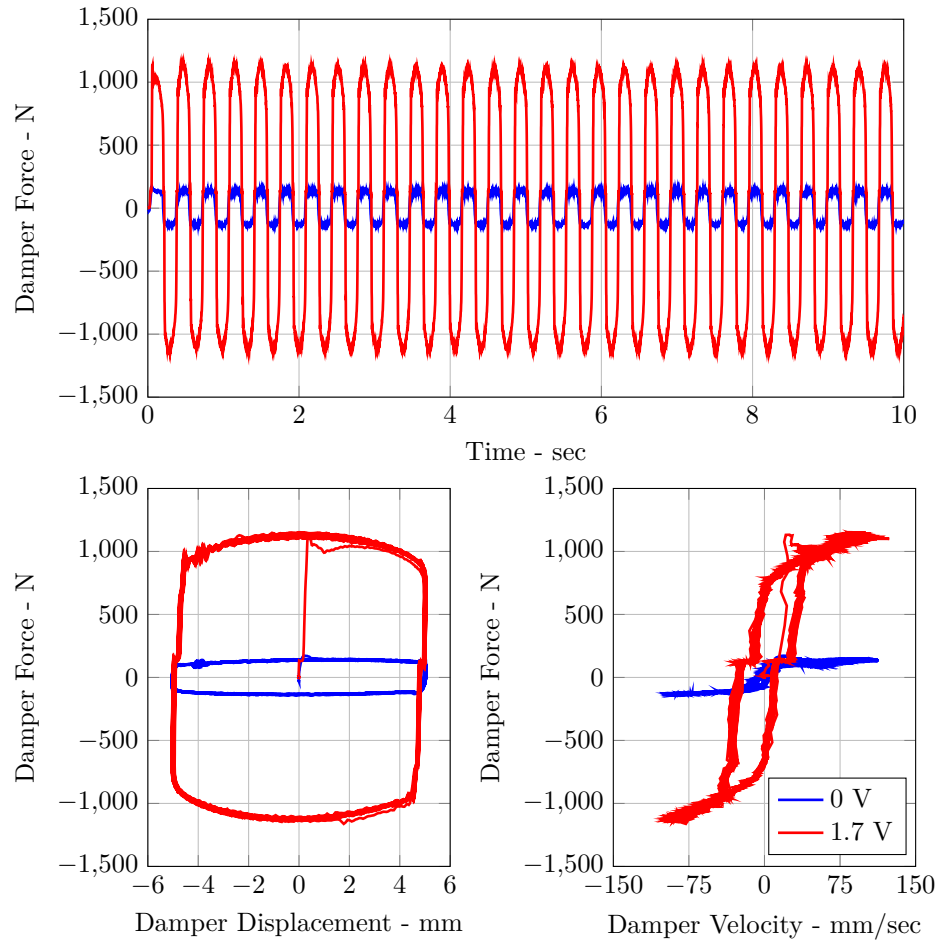


Figure 4.5: HIT MR Damper Experimental Data for 0V and 1.7V Constant Voltage Levels

(ii) Representation of Purdue Damper with HIT Damper Behavior

Since MR damper and current driver used at HIT are different from the devices at IISL, it is expected that their particular mechanical properties will affect the damper behavior.

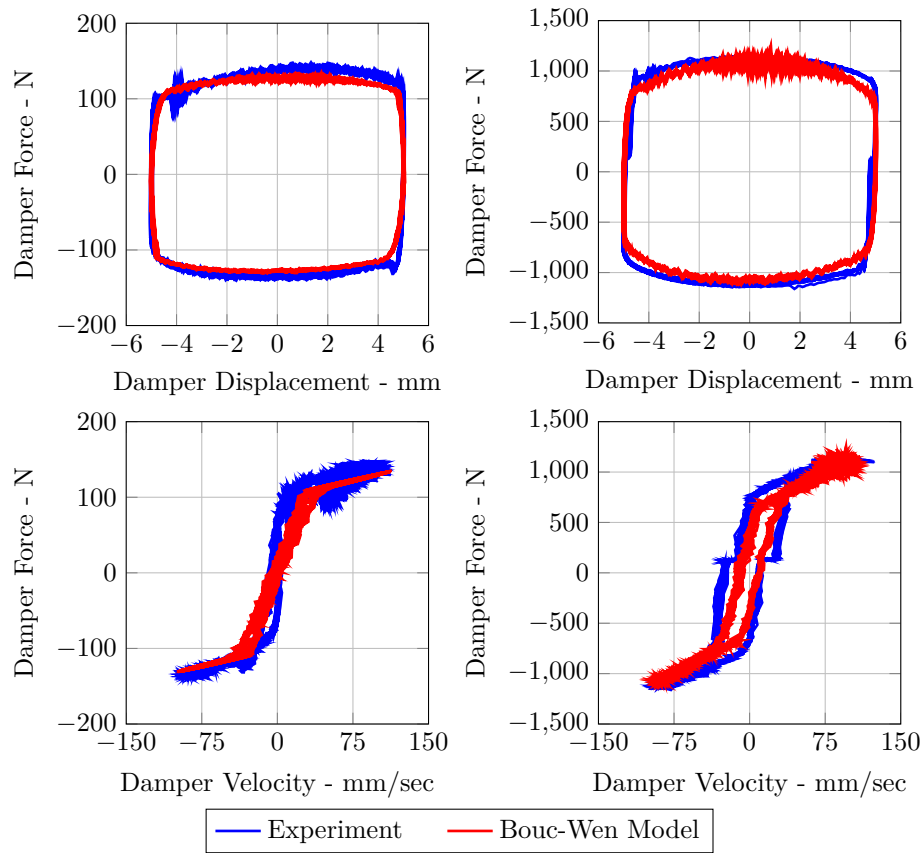


Figure 4.6: Comparisons for HIT MR Damper Experimental Data vs Identified Model

Following that, to perform successful RTHS tests and understand sources of experimental errors due to the use of physical substructures, it is imperative that a comparison between their mechanical behaviors should be employed. For this reason, both dampers are subjected to constant voltage levels in passive-off and -on modes while driven by a sinusoidal displacement input damper with a magnitude of 5 mm at 2.9 Hz. The comparison results are presented in Fig. 4.7.

It is observed that two dampers show similar passive-off (0 V) behavior before the saturation occurs, both in force-displacement and force-velocity relationships. On the other hand, at peak saturation level, Purdue damper is generating 80 N

Table 4.1: Identified Bouc-Wen Model Parameters

Parameter	Value	Unit
α_a	2740.734	N m^{-1}
α_b	10010.25	$\text{N m}^{-1} \text{V}^{-1}$
c_{0a}	175.13	N sec m^{-1}
c_{0b}	1709.24	$\text{N sec m}^{-1} \text{V}^{-1}$
c_{1a}	3353.68	N sec m^{-1}
c_{1b}	175.13	$\text{N sec m}^{-1} \text{V}^{-1}$
k_0	1940.41	N m^{-1}
k_1	1.58	N m^{-1}
γ	36332.07	m^{-2}
β	36332.07	m^{-2}
A	155.32	-
x_0	0	m
n	2	-
η	60	sec

more force than HIT damper. As for the passive-on mode, the force generated at 1.7 V for HIT damper is equivalent to the behavior of Purdue damper at 2.1 V. The two dampers show similar force-displacement and force-velocity relationships.

Based on the observations, to simulate HIT damper on the shake table on a RTHS framework at IISL/Purdue, the Purdue damper should be driven at constant 0 V and 2.1 V for passive-off and -on modes, respectively.

4.3 Semi-active Control Algorithm

Essentially, MR dampers represent a class of controllable devices where the shear force of the fluid is controlled by a magnetic field (Carlson et al., 1996; Carlson and Spencer, 1996). The effectiveness of an MR damper in controlling vibration highly depends on developing a proper control strategy. However, for designers, generating control algorithms for MR damper is often a challenge due to nonlinear nature of the fluid. To overcome the difficulty in controlling MR

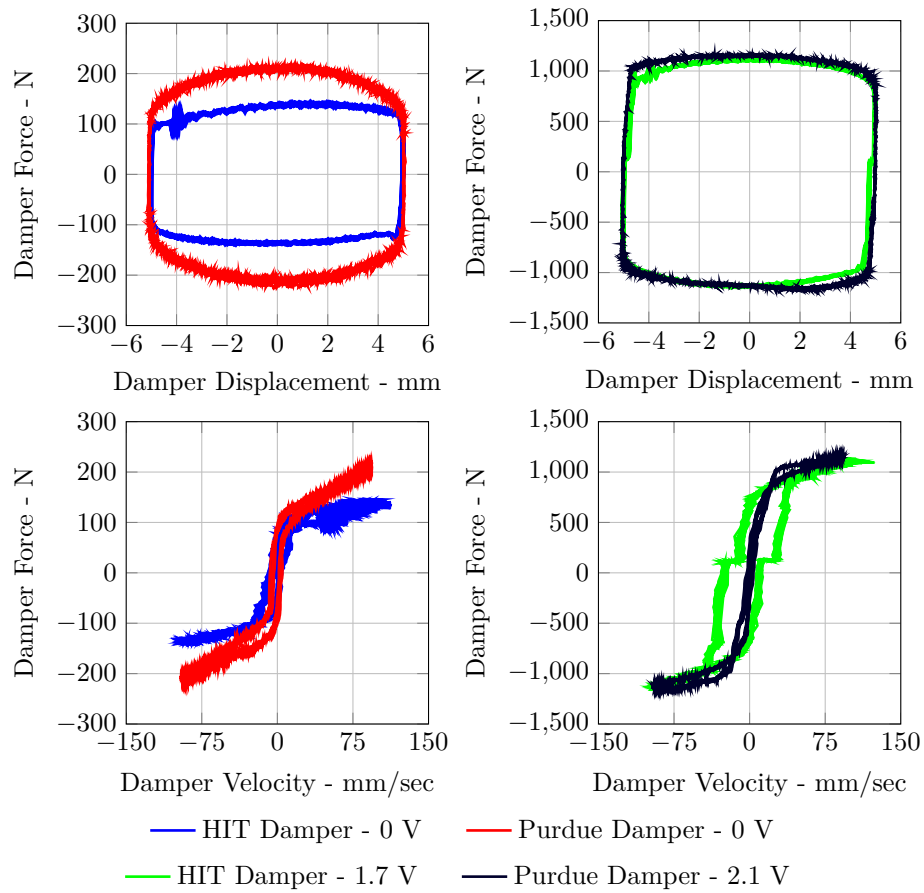


Figure 4.7: Comparisons for HIT vs Purdue Dampers

damper, [Dyke \(1996\)](#); [Dyke et al. \(1996a,b\)](#) proposed a Linear Quadratic Gaussian (LQG) regulator based clipped optimal controller that uses acceleration feedback while eliminating the need for states of velocities and displacements, which are difficult to measure for real civil structures. Although the clipped optimal control ignores dynamics of the MR damper, LQG control block attempts to linearize the nonlinear plant, herein, MR damper, with a bang-bang control. Thus, the optimal controller has still the ability to track the control force.

4.3.1 Implementation of Clipped-optimal Control Algorithm

A structure controlled with an MR damper can be idealized as in Fig. 4.8. The structure produces structural responses, y_m , when seismically excited with \ddot{x}_g . Reactively, MR damper develops force, f_m that is feedback to the structure. The system has already been formulated in Section 3.1. The force generated by the MR damper cannot be controlled directly, however, by varying the voltage input, the magnetic field can be adjusted such that a desired force history can be induced. Nevertheless, a control algorithm needs to be implemented to achieve an optimal control force while reducing structural responses. Determination of the desired force, f_c is determined with a linear optimal controller gain, K_c as:

$$f_c = \mathcal{L}^{-1} \left\{ -K_c(s) \mathcal{L} \left(\begin{bmatrix} y_m \\ f_m \end{bmatrix} \right) \right\} \quad (4.3)$$

where \mathcal{L} is the Laplace transform, y_m is the measured system response, and f_m is the measured force. To utilize desired force, f_c , clipped optimal control (COC) proposed by [Dyke et al. \(1996b\)](#) is used. Essentially, COC compares the sign of the desired force and the measured force of the damper and applies maximum voltage if the signs match, otherwise zero voltage using a bang-bang controller, as given in Eq. (4.4), :

$$v = V_{max} H((f_c - f_m)f_m) \quad (4.4)$$

where f_c represents selected optimal control force, f_m represents measured damper force and $H(x)$ is the Heaviside step function.

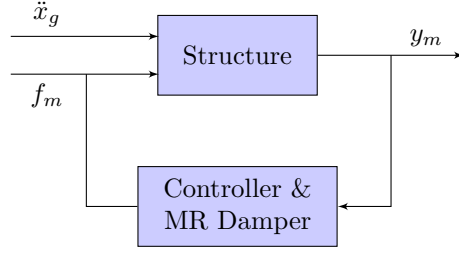


Figure 4.8: An Idealization of Structural Control with MR Damper

4.3.2 Implementation of H_2/LQG Control

Assuming earthquake is a stochastic process, an optimal control problem to estimate K_c with the aim towards optimal minimization of structural responses can be constructed using H_2/LQG . Fundamentally, LQG is the combination of a linear-quadratic estimator (LQE) with a linear-quadratic regulator (LQR). In general, LQR is sufficient to estimate the control force only with the internal states, such as velocity and displacement responses of a structure. In reality, it is hard to measure such states without fixed reference points. Fortunately, many accelerometer forms are classified as inertial sensors, have their reference frame inside the sensor mechanism and allow measuring acceleration without any issues. Later, unobserved internal states can be restored with the help of observed states with LQE and are feed-forward to LQR (Kalman, 1960). A typical LQG regulator can be described such as:

$$\dot{\hat{x}} = (A - LC)\hat{x} + Ly_m + (B - LD)f_m \quad (4.5)$$

where \hat{x} is estimated unobserved states and L is quadratic estimator gain. With the help of Eq. (4.5), Eq. (4.3) can be simplified to:

$$f_c = K\hat{x} \quad (4.6)$$

where K is quadratic regulator gain.

Computation of LQR Gain

For a continuous-time state-space model with state-feedback presented in Eq. (4.6), infinite horizon performance index or cost function, J to be minimized can be formulated:

$$J(f_m) = \int_0^{\infty} y_o^T Q_{LQR} y_o + f_m^T R_{LQR} f_m \, dx \quad (4.7)$$

where y_o is the system responses to be optimized, Q_{LQR} and R_{LQR} are weighting matrices determining the relative importance of state variables and control forces. A Riccati equation can be formed using Q_{LQR} , R_{LQR} and state space of the system.

$$A^T S + SA - (SB)R_{LQR}^{-1}(B^T S) + Q_{LQR} = 0 \quad (4.8)$$

Finally, regulator gain, K can be derived as:

$$K = R_{LQR}^{-1} B^T S \quad (4.9)$$

Computation of LQE Gain

LQE, i.e. Kalman state estimator filter provides an optimal solution of unobserved states for a given system with process and measurement noise. A system described in Eqs. (3.4) and (3.5) can be rewritten including such noises:

$$\dot{x} = Ax + Bu + Gw \quad (4.10)$$

$$y = Cx + Du + Hw + v \quad (4.11)$$

where w and v are white process and white measurement noises with the following definitions:

$$E(w) = E(v) = E(wv^T) = 0 \quad (4.12a)$$

$$E(ww^T) = Q_{LQE} \quad (4.12b)$$

$$E(vv^T) = R_{LQE} \quad (4.12c)$$

Here, G and H correspond to E and F in Eqs. (3.4) and (3.5). Eq. (4.12) implies that ground excitation is a process noise and both process and measurement noises are Gaussian stationary white noise with zero mean. Estimated state, \hat{x} can be obtained by minimizing error covariance such as:

$$P = \lim_{t \rightarrow \infty} (\{x - \hat{x}\}\{x - \hat{x}\}^T) \quad (4.13)$$

A Ricatti equation can be assembled to solve P :

$$A^T P + P A - (P C^T) R^{-1} (C P) + Q_{LQR} = 0 \quad (4.14)$$

which leads to the computation of the estimator gain, L :

$$L = (P C^T + G Q_{LGE} H^T) (R_{LGE} + H Q H^T)^{-1} \quad (4.15)$$

For typical implementations of COC, first, regulator and estimator gains are determined from built-in *lqry.m* and *lqew.m* MATLAB scripts. Later, Eqs. (4.4) and (4.5) are formulated as block diagrams in Simulink.

4.4 Summary

In this chapter, a general way to characterize and model MR dampers are discussed. Following that, a parametric model of the MR damper located at HIT is developed. In addition, force-displacement and force-velocity relationships of the Purdue damper are tried against HIT damper at passive-off and -on modes. The motivation and concepts of semi-active control strategies, particularly, LQG control and its implementation are discussed for its use in shake table tests and RTHS. In the following chapters, the control algorithm introduced here will be employed in several simulations, experiments and RTHS.

CHAPTER 5

VERIFICATION OF SHAKE TABLE TESTS WITH ANALYTICAL SIMULATIONS

In this chapter, a description of the experimental study is given to validate the model of the three story structure equipped with MR damper by comparing the responses with those of shake table tests. First, Section 5.1 discusses the selection and design of MR damper controllers aimed towards effective structural control. Next, Section 5.2 illustrates post-processing procedure of the structural responses yielding from shake table tests and simulations for comparison purposes. In Section 5.3, performance of the structural model introduced in Chapter 3 is evaluated using a variety of earthquake inputs through both numerical simulation and shake table tests under different damper control strategies. For all cases, error in relative displacement, absolute acceleration in the global sense of the structure is examined including other evaluation criteria discussed in Section 3.5.

Finally, a summary of the chapter, that interprets and concludes main findings in the comparisons, is given in Section 5.4.

In order to perform a successful comparison between shake table experiments and pure analytical simulations, several steps must be taken, including (i) modeling of the existing test structure, (ii) characterization of the MR damper which will be used in analytical simulations, and (iii) design of MR damper semi-active control algorithms.

Step (i) was already explained in Chapter 3 in detail. Furthermore, steps (ii) and (iii) were discussed in Chapter 4. In the following sections of this chapter, design of the MR damper controllers is also discussed.

5.1 Design of MR Damper Controllers

For pure simulations, the damper model based on HIT damper is utilized. Three cases are considered for structural control problem based on this damper. Those are (i) passive-off case where a constant 0 V is sent to the current driver; (ii) passive-on case where damper is fed with a constant 1.7 V; and finally (iii) semi-active control case where clipped-optimal control strategy is implemented. The principle of semi-active control has already been discussed in Chapter 4. For semi-active control, displacement responses are estimated from three floor accelerations and first floor relative MR damper displacement. To ensure effectiveness of the structural control in reducing accelerations, R matrix is selected to be the identity matrix with proper order, whereas a wide range of Q matrices were tested using a variety of earthquakes. Finally, Q matrix is selected to be 23000 with equal weighting on all floor accelerations of the structure, for shake table tests and pure simulations.

5.2 Post-processing of Data

Each shake table test record lasts 60-200 seconds or longer. For the initial 10–60 seconds of the recorded data, shake table is kept at zero position. After stand-by time, the actual earthquake input is initiated which takes 50–60 seconds. Finally, another 10–60 seconds of data is recorded until the structural responses fully decay and test setup is ready for a new test.

The recorded data is long and also contains noise due to the test apparatus used during the experiments. Therefore, post-processing is required to make it presentable for further analysis. It should be noted that the results of the shake table tests and simulation results are similarly post-processed as explained in the following sections.

5.2.1 Time Windowing

To employ a robust visual comparison between records, a rectangular time window is applied isolating response where ground motion is dominant. An example is illustrated in Fig. 5.1. After windowing, the start of the response is assumed as $t = 0$.

For relative RMS and peak error calculations, the responses are windowed even further, where the earthquake is strongest. For already windowed responses, this range is 2–5 seconds for El Centro, 3–6 seconds for Kobe, and 1.5–4.0 seconds for Morgan Hill.

5.2.2 Filtering

The structural responses obtained experimentally from shake table tests may contain some artifacts that can affect comparisons of simulations results. Mostly, such artifacts are comprised of measurement errors due to (a) unwanted forced

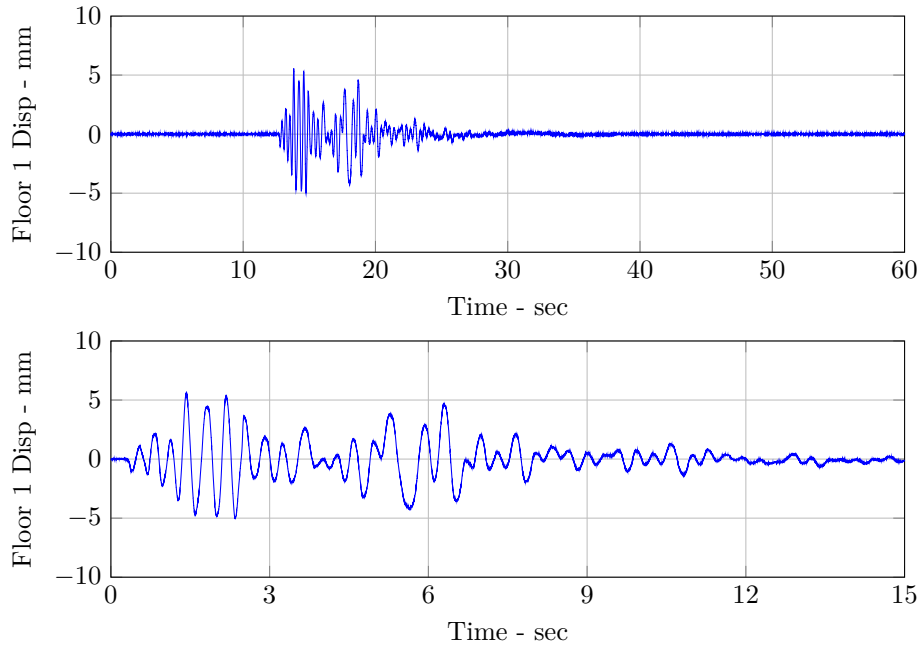


Figure 5.1: Application of Time Windowing to First Floor Displacement Response for Morgan Hill Semi-Active Control Case

vibrations caused by the actuator driving the shake table and (b) amplification of the forced vibration by the structure, and (c) strong ground motion affecting off-plane dynamics of the test structure.

Since hydraulic fluid is compressible, it has a finite stiffness. When a hydraulic actuator system is coupled with mass, the fluid resonates with mass. This phenomenon, often called oil-column resonance, tend to cause vibration issues. Eventually, if the coupled mass is large enough, the resonance can leak into frequency content of the structure. Considering the fact that shake table represents a very large mass, oil-column resonance frequency is low enough to affect the structural responses (Nakata, 2013).

The proposed modeling approach discussed in Chapter 3 discretizes the *continuous-time system* test structure into 3-DOF model. Although the applied ground motion is unidirectional along the weak-plane of the structure, the test

setup is not perfect and therefore, it is inevitable that higher modes including torsional and off-plane modes of the system will be induced.

Those artifact can be reduced substantially by filtering responses of the system. A 5th order Butterworth filter with a cut-off frequency of 50 Hz is used to eliminate such responses. The same filter is also applied to the pure simulation results. An example is illustrated in Fig. 5.2 to demonstrate the effectiveness of the filter. It should be noted that the acceleration response is smoothed.

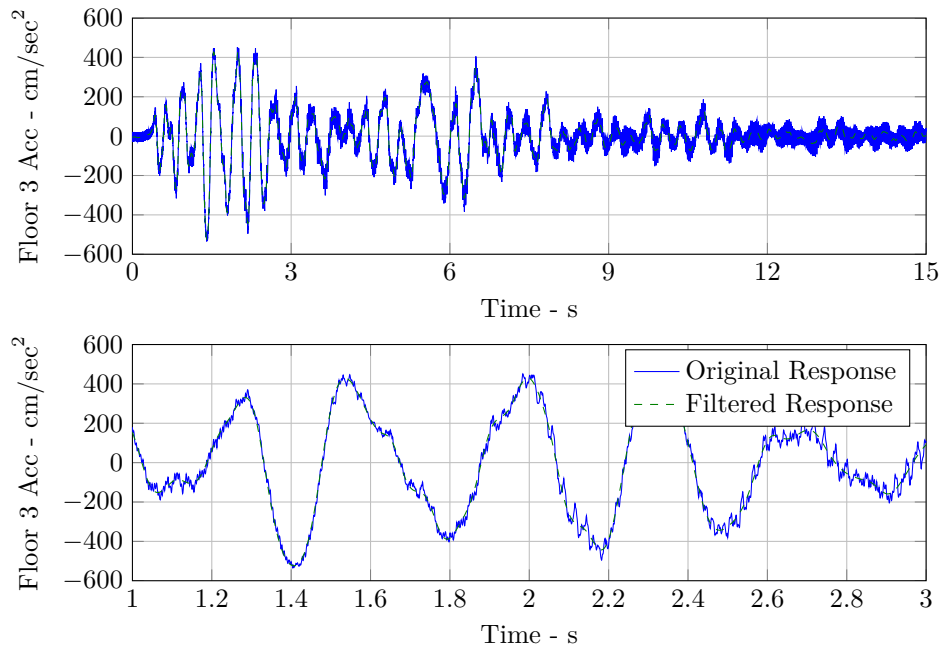


Figure 5.2: Effect of Butterworth Filtering to Third Floor Acceleration Response for Morgan Hill Semi-Active Control Case

5.2.3 Frequency-Domain Calculations

In addition to time-domain post-processing, results were also evaluated in frequency domain. In the course, power spectral density (PSD) of the strong

motion response are calculated using *pwelch* command in MATLAB. PSD estimates are determined as one-sided with no window-averaging and overlapping using windowed responses of 2–6 seconds for all three earthquakes.

5.3 Comparison of Shake Table Test Responses with Pure Simulation Results

To employ a proper comparison between simulation and experimental results, a good understanding of the test structure is required. The test structure used in the shake tables tests was explained in detail in Chapter 2. Development of the accurate model of the structure in *MCK* format was provided in Chapter 3. To simulate the behavior of MR Damper under various control voltages, a model was proposed in Chapter 4. Excitation input to the structure is selected as El Centro, Kobe and Morgan Hill earthquakes. The ground motion in displacement form calculated by double integrating each earthquake is fed to the shake table actuator controller. More detail on the selected earthquakes and tracking performance of the shake table are given in Section 2.3.3. All floor accelerations for the shake tables tests are sampled at 5000 Hz. The ground acceleration of the shake table is captured with two accelerometers and the response is averaged. For each structural control case, the averaged ground acceleration recorded during the specific test is applied as the excitation input to the numerical model, as-is without further modifications. As the shake table tests, numerical simulations are also conducted at a rate of 5000 Hz. An illustration of the Simulink diagram containing numerical structure and MR damper model is given in Fig. 5.3.

The experimental plan for evaluation and validation of the integrated model is focused on replicating the dynamic response of the seismically-excited three story structure equipped with damper device at passive on/off and semi-active

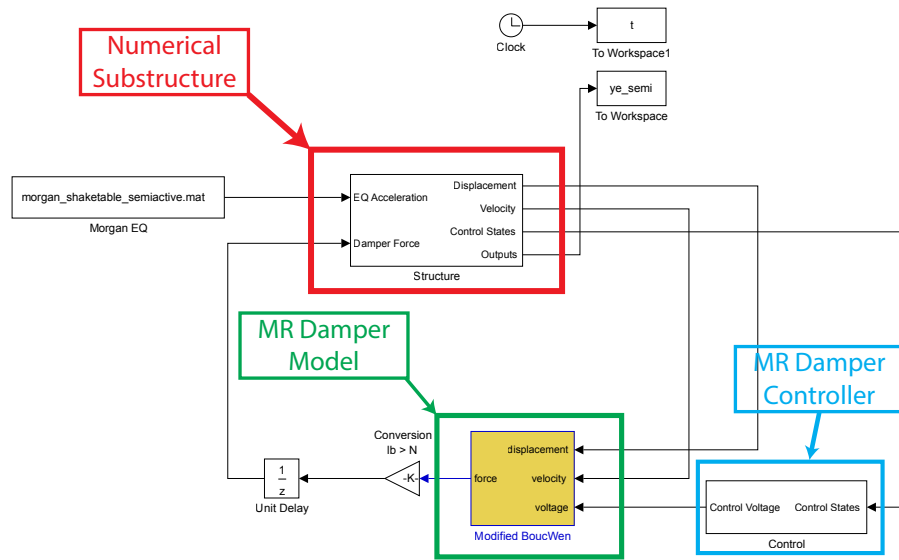


Figure 5.3: A Representative Simulink Model of the Analytical Simulation

control modes. To assess accuracy of the proposed model, the shake table responses are compared to simulation results using the evaluation criteria proposed in Chapter 3. Particularly, RMS, peak and sliding RMS errors are utilized for recorded displacements and accelerations. To sum up, nine individual comparisons, containing three earthquake cases each with three control modes, are conducted to achieve the study goals.

5.3.1 El Centro

In this section, results between shake table and pure simulations are compared for El Centro earthquake. Passive-off (POFF), -on (PON) and semi-active (SA) cases are considered for the comparisons.

Passive-off

Displacement and acceleration comparisons are given in Figs. 5.4 and 5.5. RMS and peak response errors are tabulated in Table 5.1 in percentage. Likewise, in

Fig. 5.6, moving RMS errors are illustrated.

While the reported peak error of floor accelerations and displacements are ranging from 4% to 15%, the normalized RMS errors are trending from 15% to 20%. In addition, range-normalized RMS errors are no more than 15%. Both time- and frequency-domain responses are in correlation.

Passive-on

For PON case, related comparisons and error tables are given in Figs. 5.7 to 5.9 and Table 5.1. Although time-domain displacement responses are not in an ideal correlation, the power spectrum demonstrates that the frequency contents still agree. There is a deviation observed in the first floor displacement time-domain responses around 3–9 seconds. This same trend is also observed in moving RMS error plot. Considering the fact that the first floor acceleration responses are very similar, the aforementioned discrepancy does not indicate a modeling error, but LVDT failure. By inspecting the results, one can conclude that MR damper LVDT might have been stuck due to friction when cyclic displacements are small enough (± 0.5 mm).

RMS and peak response errors for floor accelerations and displacements are ranging from 4% to 45%. The criteria-averaged RMS error is varying from 15% to 30%. The elevated errors indicate that with increasing levels of MR damper forces, it is harder to match structural responses in time-domain.

Semi-active

The comparisons for SA case are given in Figs. 5.10 to 5.12 and Table 5.1.

RMS and peak response errors vary from 3% to 25%, while criteria-averaged RMS errors are reaching up to 15%. Compared to PON case, the errors are much smaller since MR damper forces fall in between PON and POFF cases.

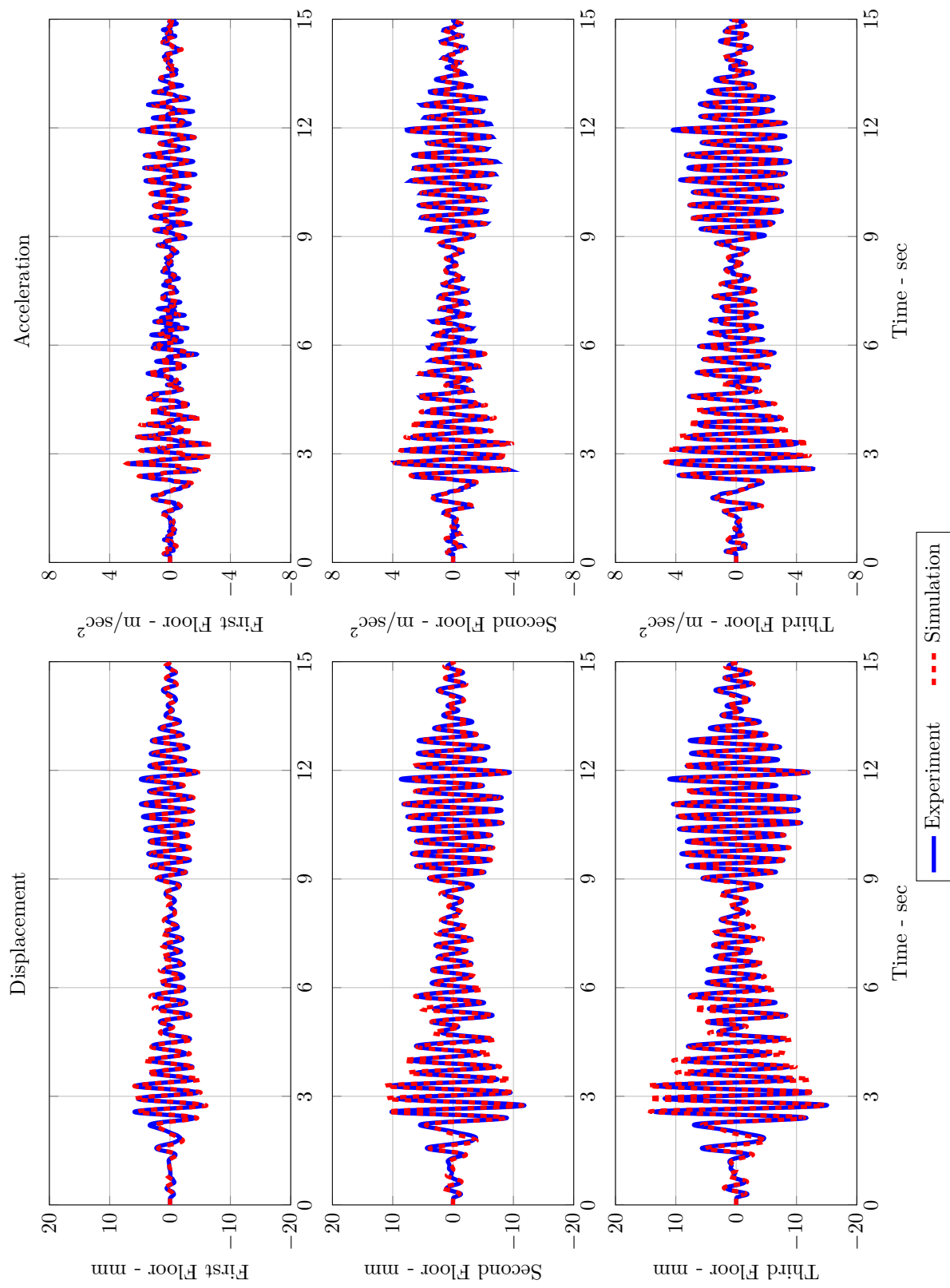


Figure 5.4: El Centro Earthquake Comparison in Time Domain for POFB Case

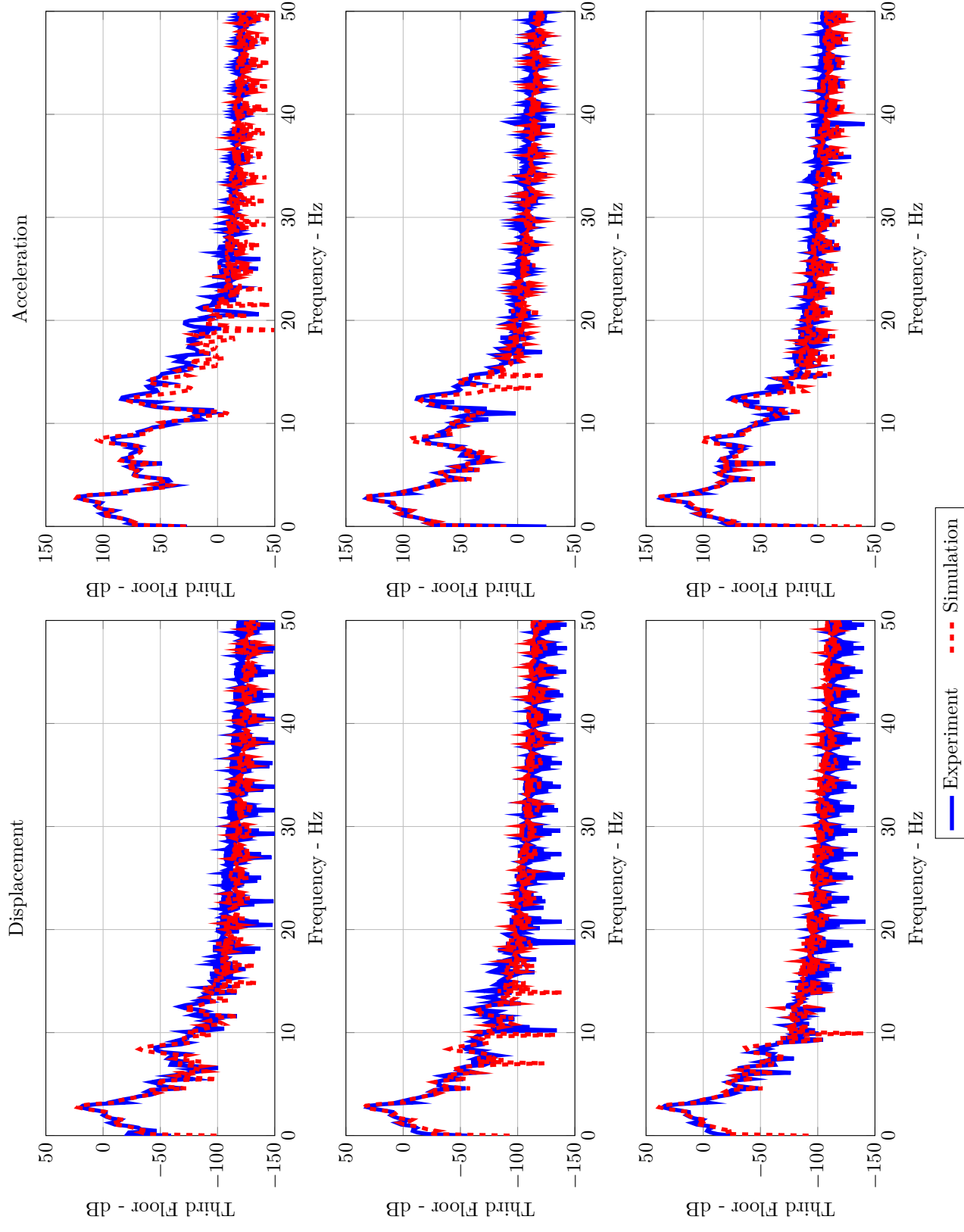


Figure 5.5: El Centro Earthquake Comparison in Frequency Domain for POFB Case

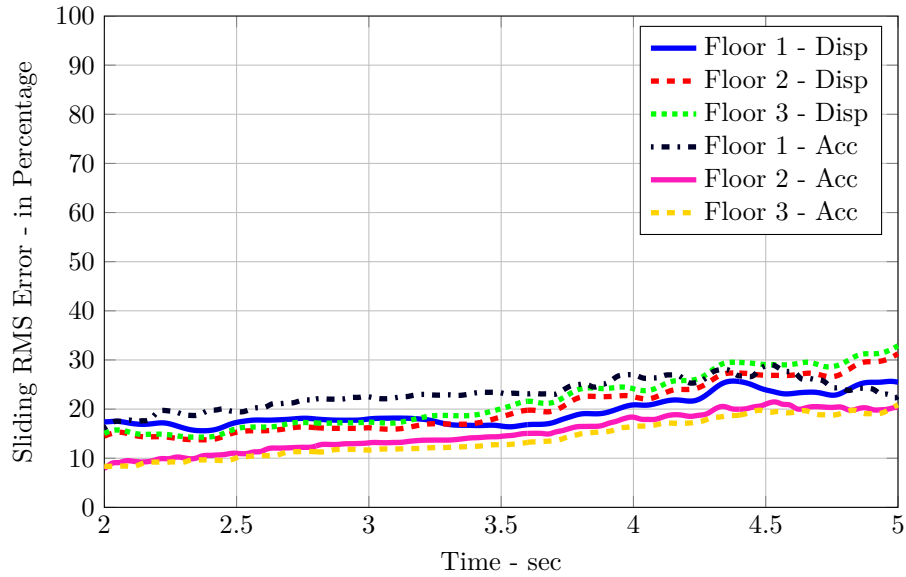


Figure 5.6: Moving RMS Error for El Centro Earthquake POFF Case

5.3.2 Kobe

In this section, results between shake table and pure simulations are compared for Kobe earthquake. POFF, PON and SA cases are considered for the comparisons.

Passive-off

Shake table vs. simulation response comparisons are given in Figs. 5.13 and 5.14. This case has the smallest error among all cases including El Centro and Morgan Hill earthquakes.

Passive-on

PON case comparisons are given in Figs. 5.16 and 5.17. In Fig. 5.9 and Table 5.1, error tables and moving RMS error plot are provided.

Although errors are similar to El Centro and Morgan Hill PON cases, discrepancy due to LVDT is most evident in this case. RMS and peak response

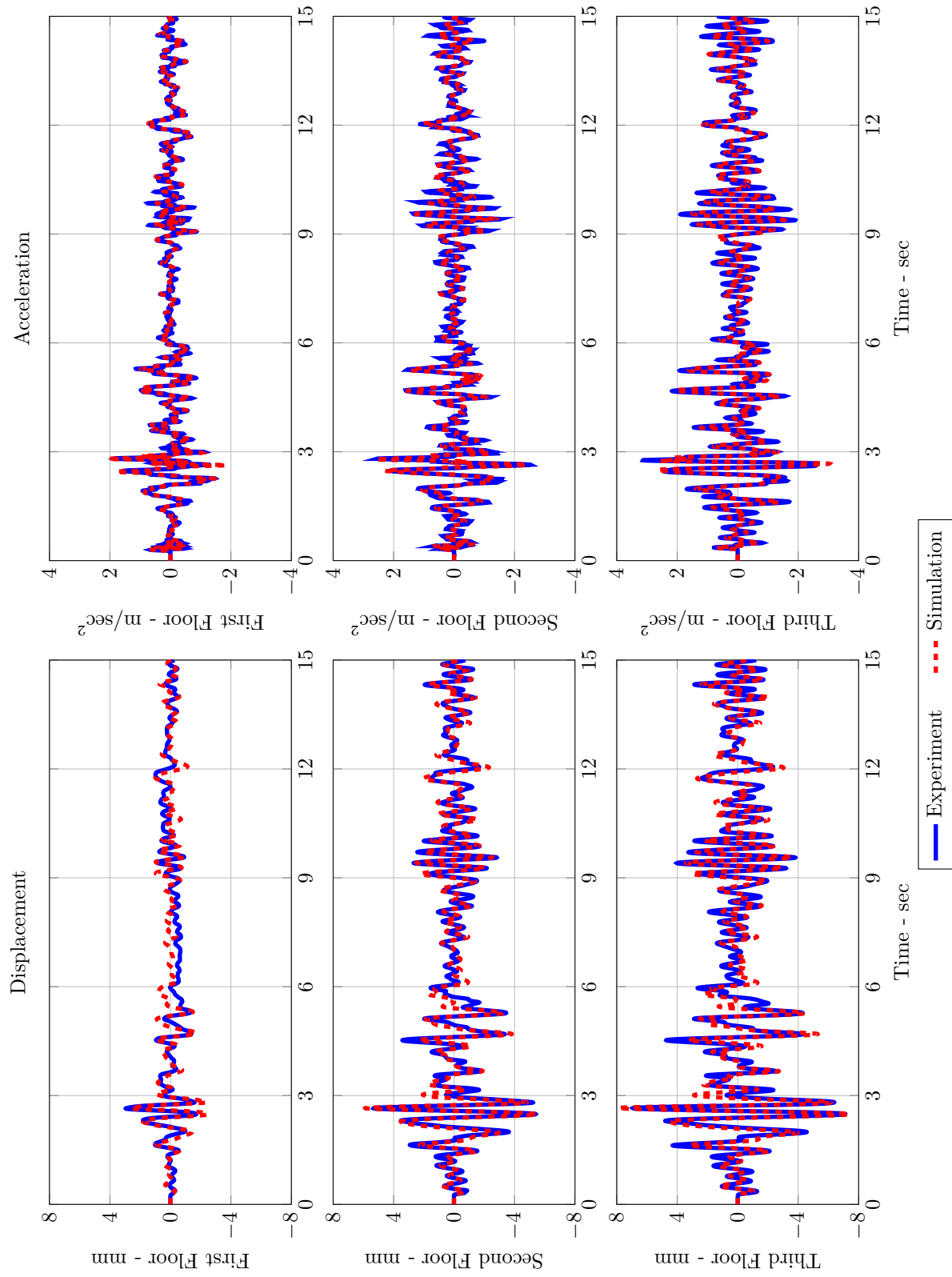


Figure 5.7: El Centro Earthquake Comparison in Time Domain for PON Case

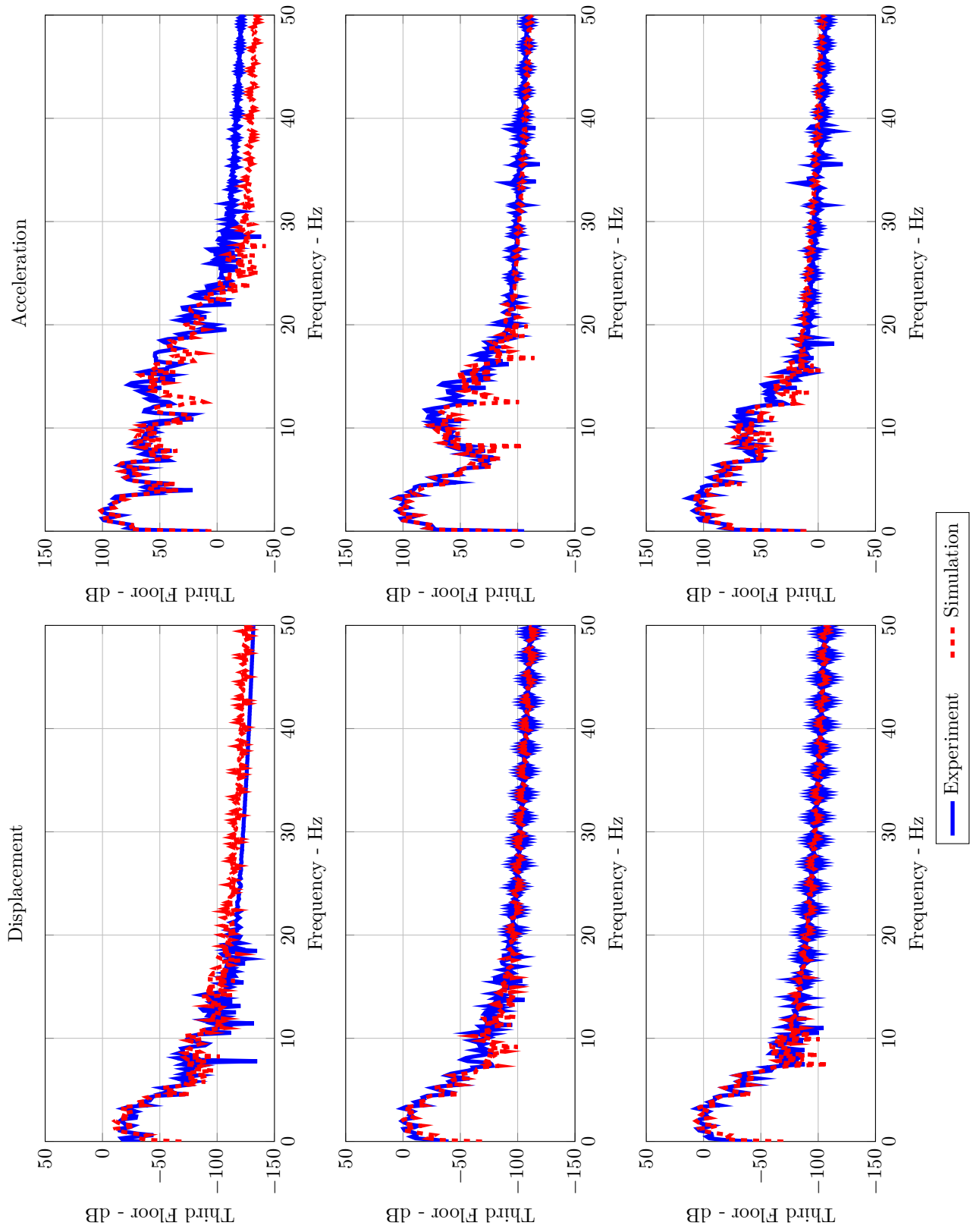


Figure 5.8: El Centro Earthquake Comparison in Frequency Domain for PON Case

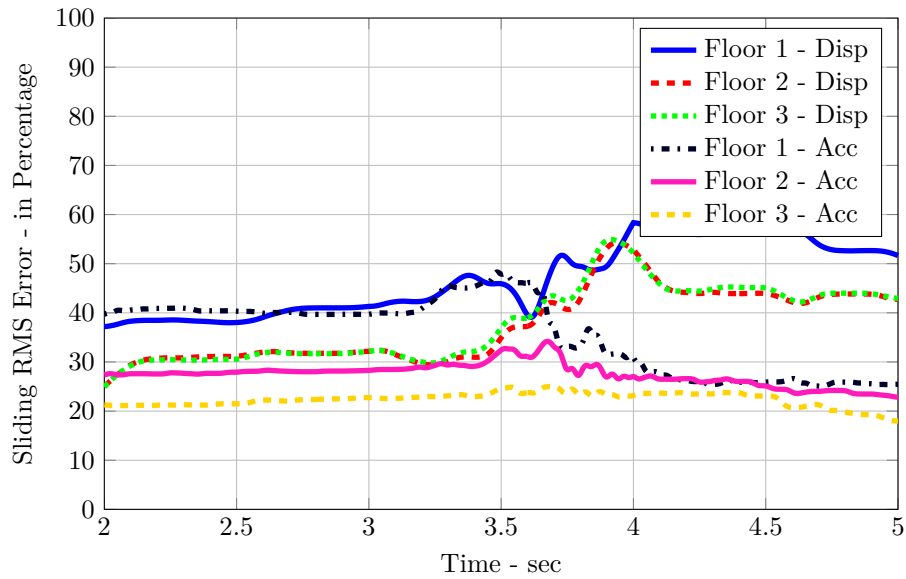


Figure 5.9: Moving RMS Error for El Centro Earthquake PON Case

errors range from 10% to 60%, while criteria-averaged errors are bounded to 30% to 35%.

Semi-active

In Fig. 5.19 and Fig. 5.20, SA case comparisons are presented.

Like in El Centro case, this SA case produced less errors compared PON case. The peak and RMS errors and criteria-averaged errors are in the range of 3% to 30% and 12% to 16%, respectively.

5.3.3 Morgan Hill

In this section, results between shake table and pure simulations are compared for Morgan Hill earthquake. POFF, PON and SA cases are considered for the comparisons.

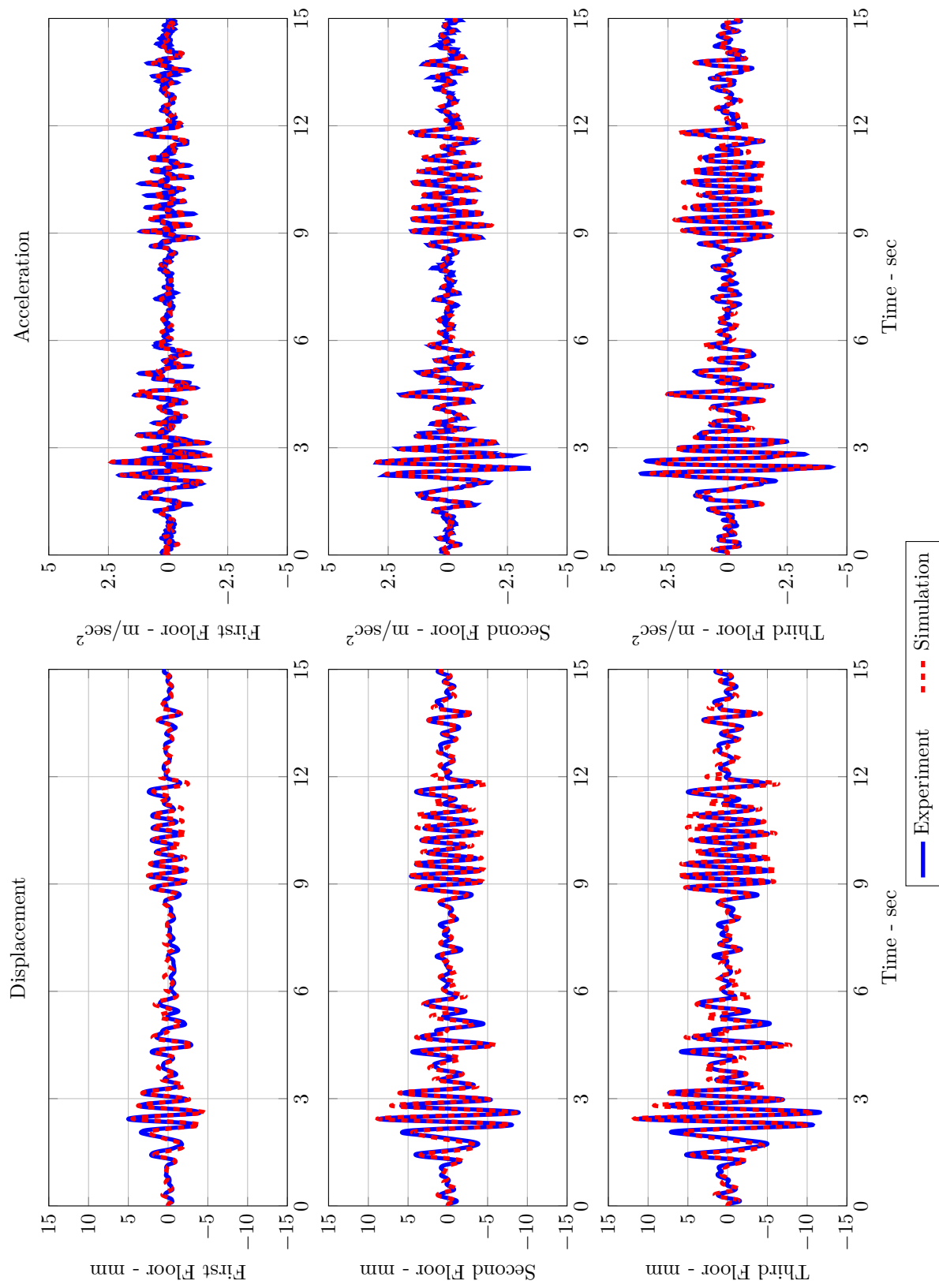


Figure 5.10: El Centro Earthquake Comparison in Time Domain for SA Case

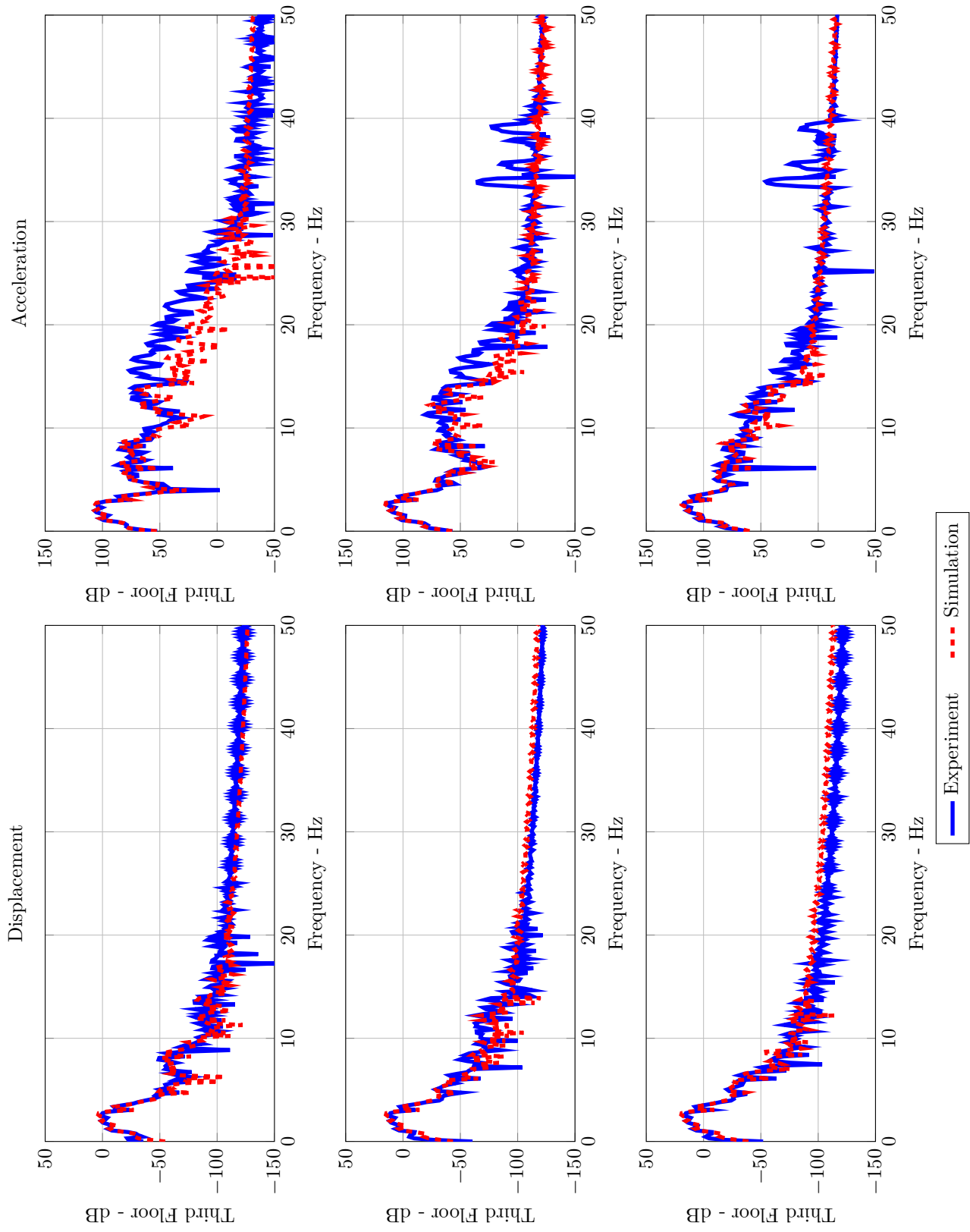


Figure 5.11: El Centro Earthquake Comparison in Frequency Domain for SA Case

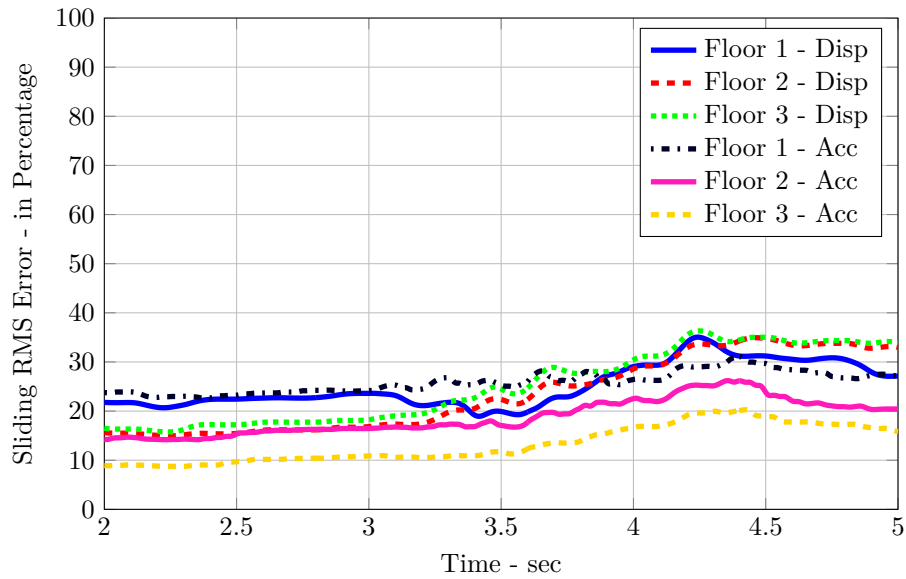


Figure 5.12: Moving RMS Error for El Centro Earthquake SA Case

Passive-off

Time- and frequency-domain comparisons for POFF case are provided in Figs. 5.13 and 5.14. The reported errors are in the range of 5% to 27% and consistent with El Centro and Kobe cases. The averaged errors are as high as 9%.

Passive-on

Displacement and acceleration comparisons are given in Figs. 5.25 and 5.26. Although the time- and frequency-domain responses are in correlation, the errors are as high as the other two earthquake cases, closer to Kobe case.

RMS and peak response errors for accelerations and displacements are ranging from 6% to 60%. On the other hand, the criteria-averaged RMS error is varying from 19% to 28%.

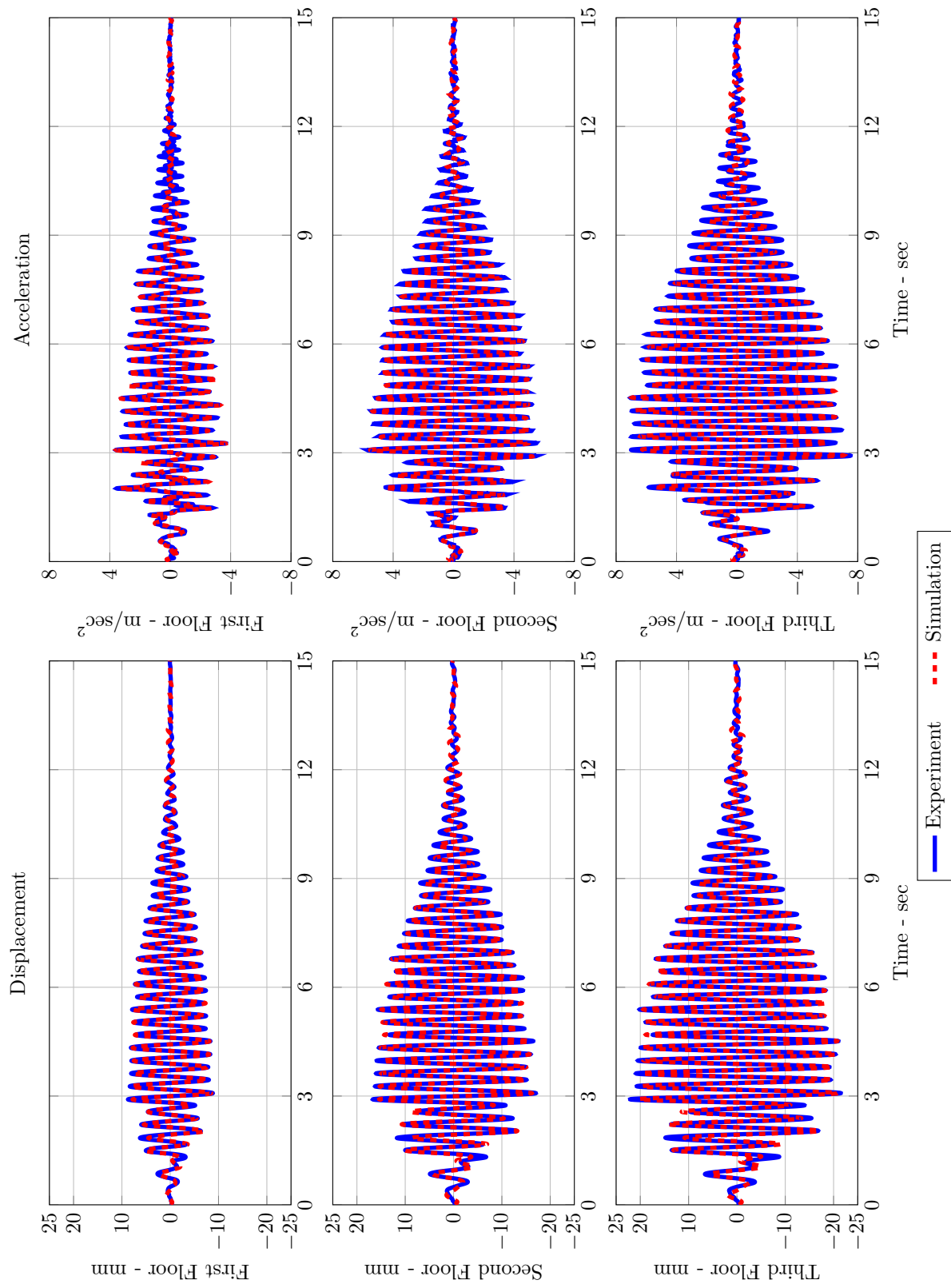


Figure 5.13: Kobe Earthquake Comparison in Time Domain for POFF Case

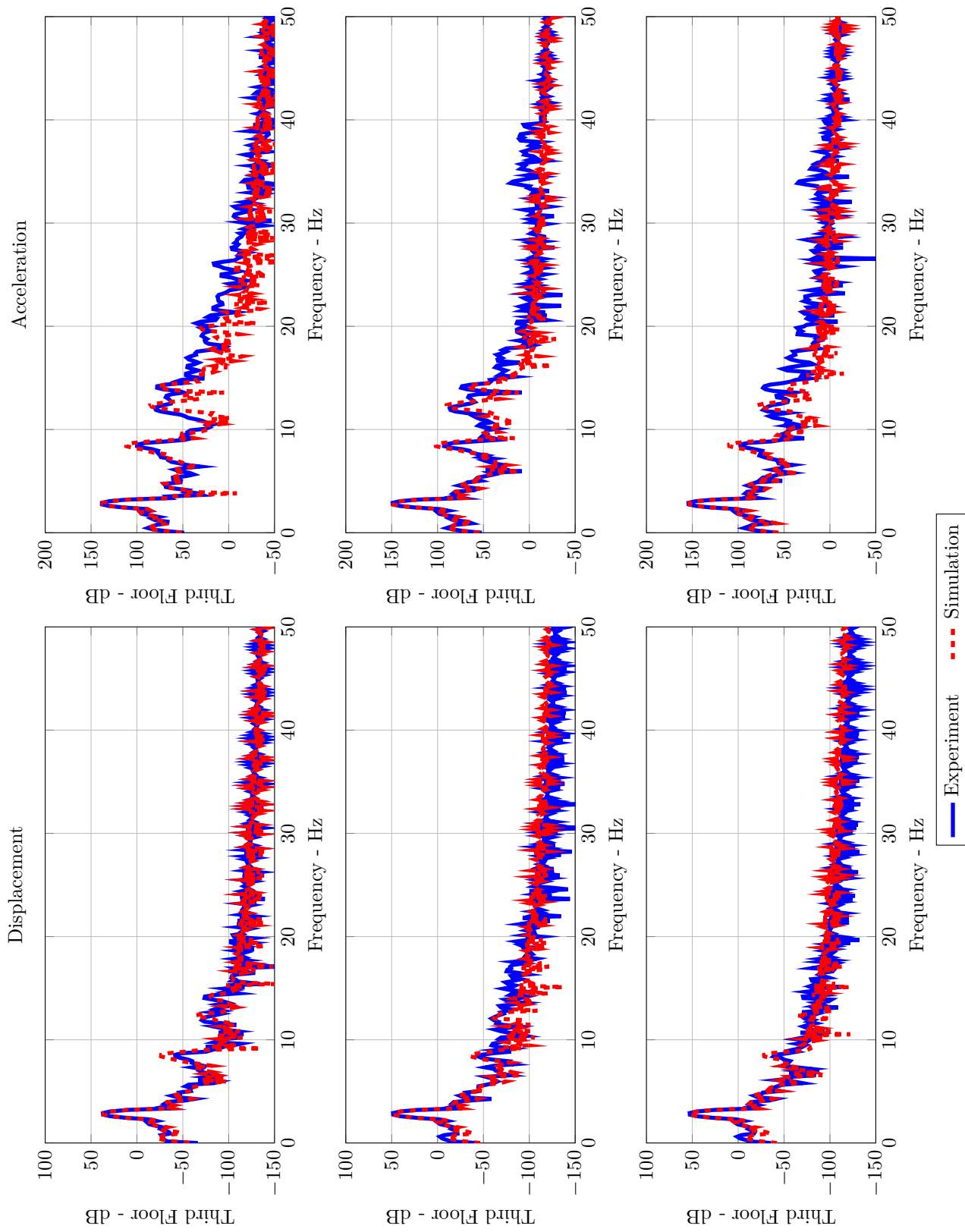


Figure 5.14: Kobe Earthquake Comparison in Frequency Domain for POFF Case

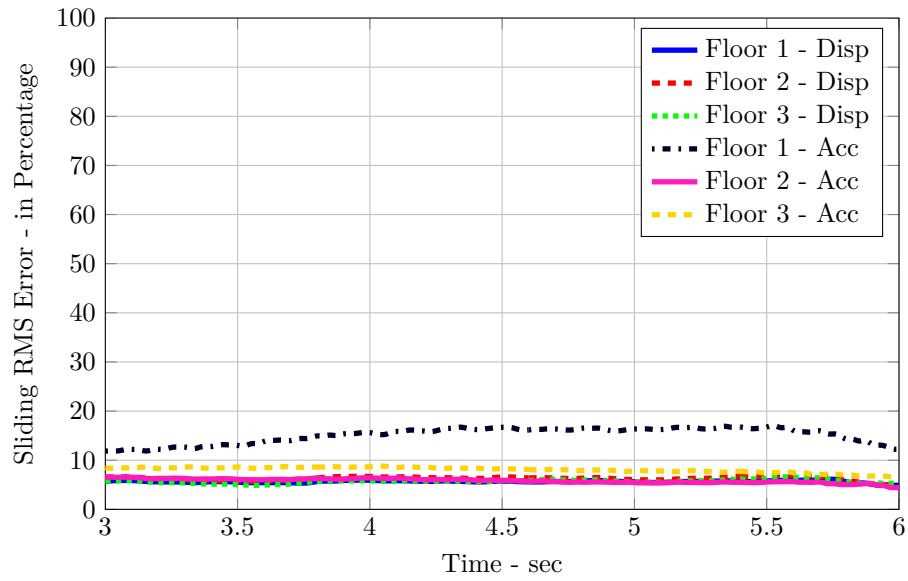


Figure 5.15: Moving RMS Error for Kobe Earthquake POFF Case

Semi-active

SA case comparisons are presented in Figs. 5.19 and 5.20. The RMS and peak response errors are confined within 3% to 18%. All criteria-averaged errors are concentrated near 10%.

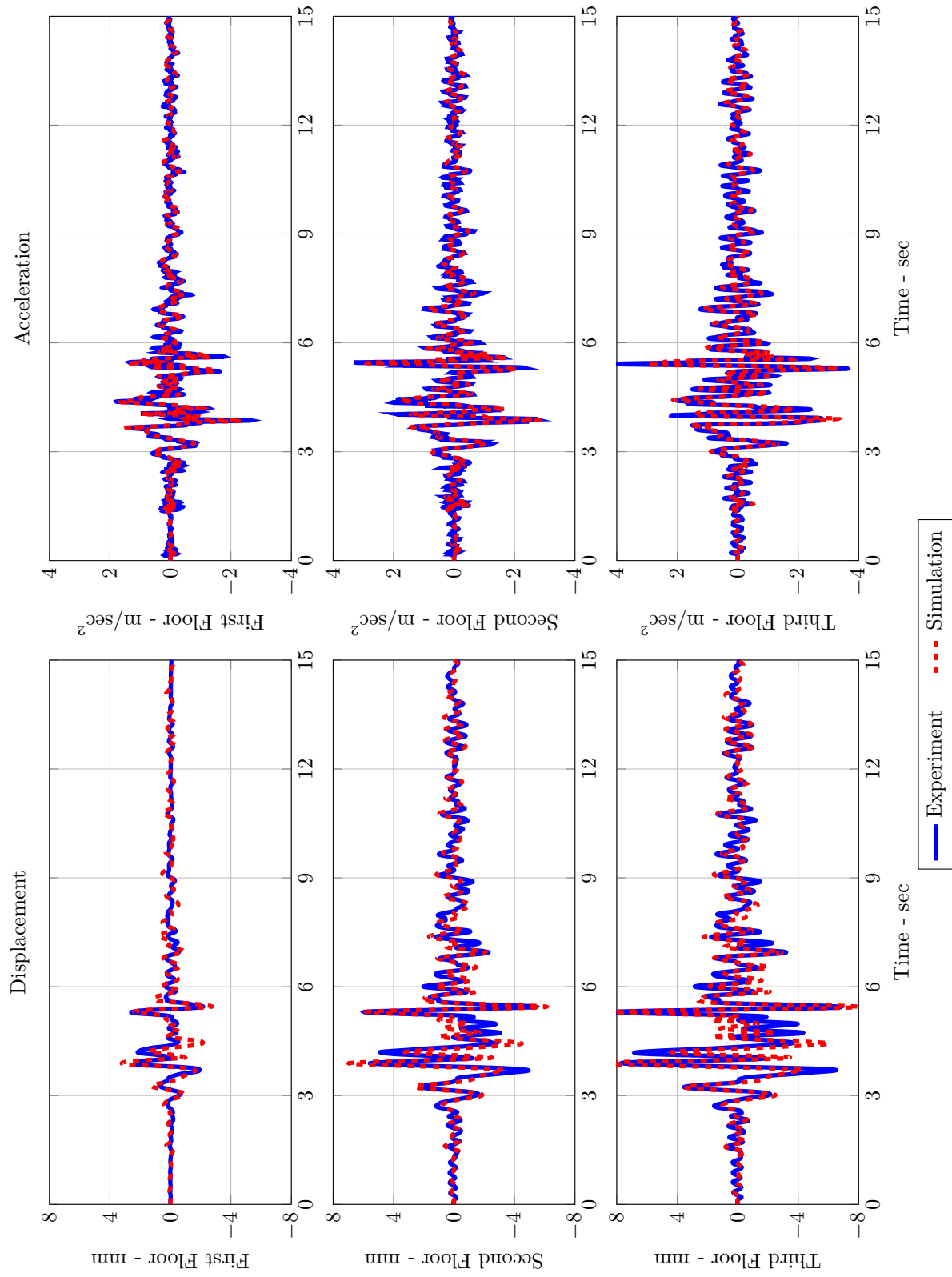


Figure 5.16: Kobe Earthquake Comparison in Time Domain for PON Case

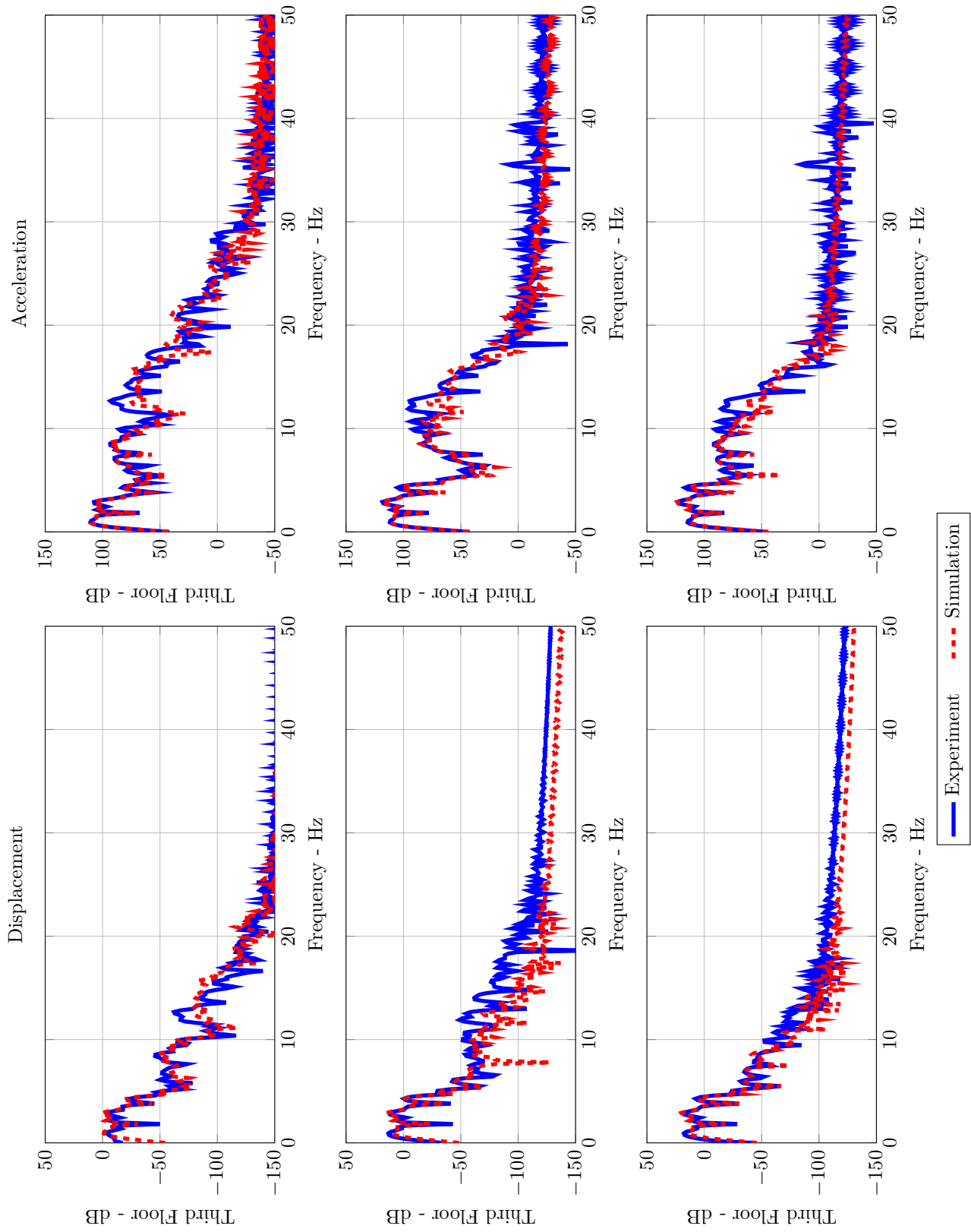


Figure 5.17: Kobe Earthquake Comparison in Frequency Domain for PON Case

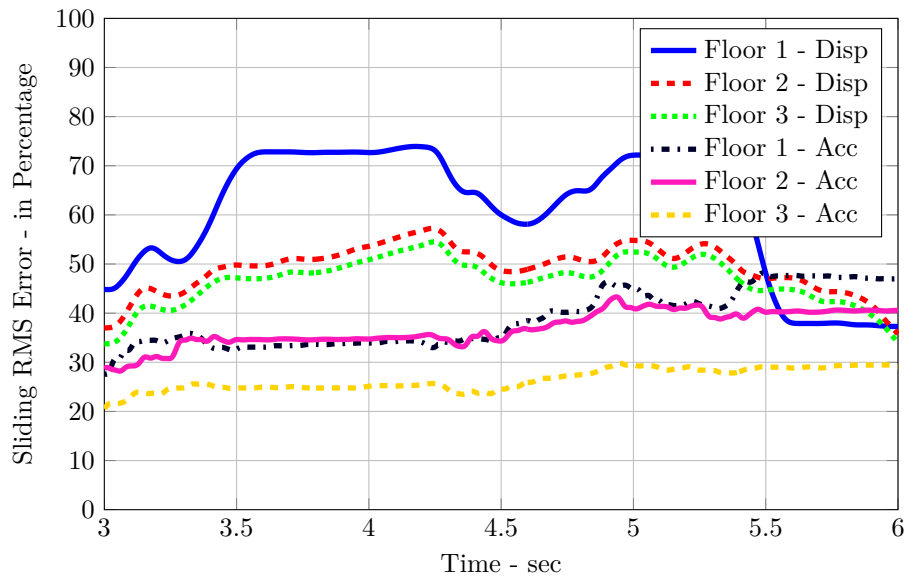


Figure 5.18: Moving RMS Error for Kobe Earthquake PON Case

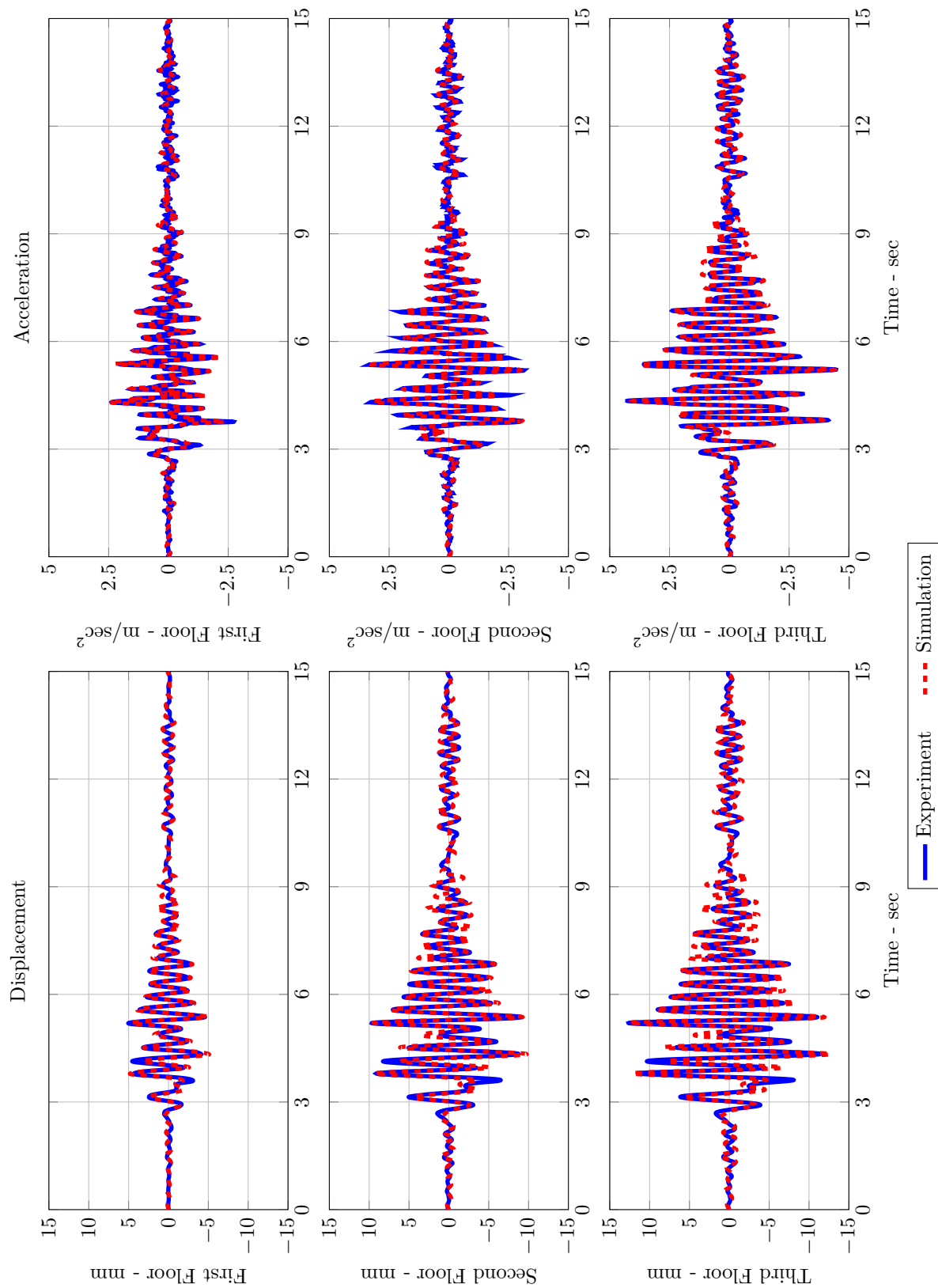


Figure 5.19: Kobe Earthquake Comparison in Time Domain for SA Case

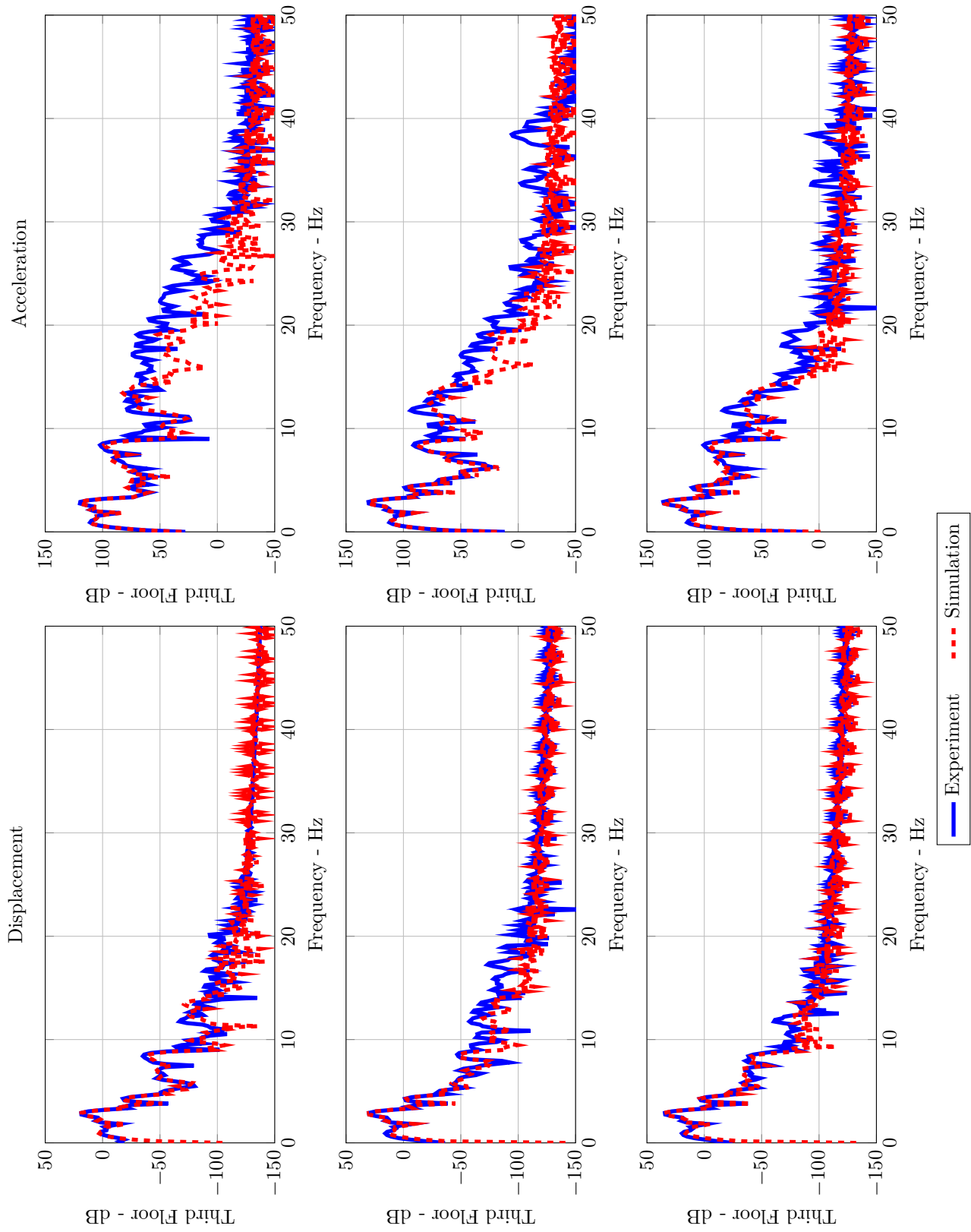


Figure 5.20: Kobe Earthquake Comparison in Frequency Domain for SA Case

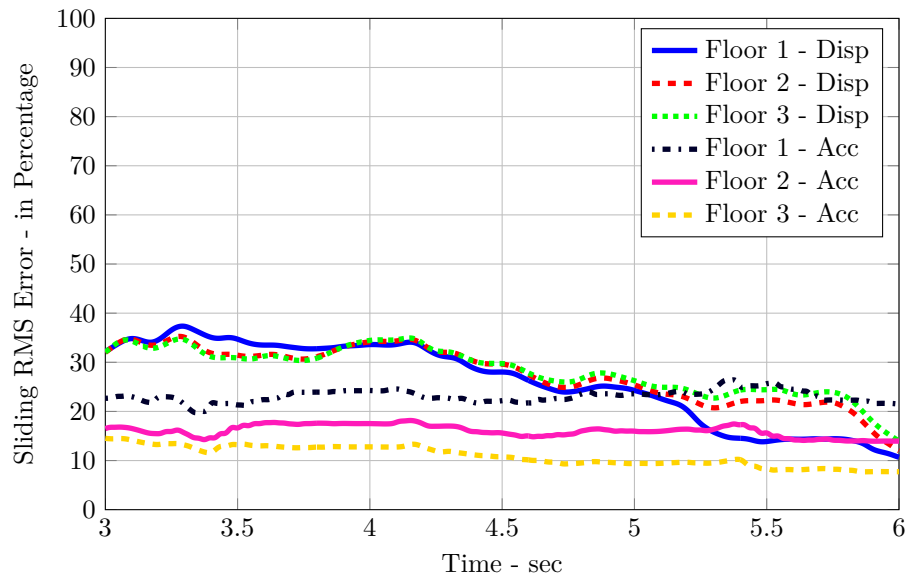


Figure 5.21: Moving RMS Error for Kobe Earthquake SA Case

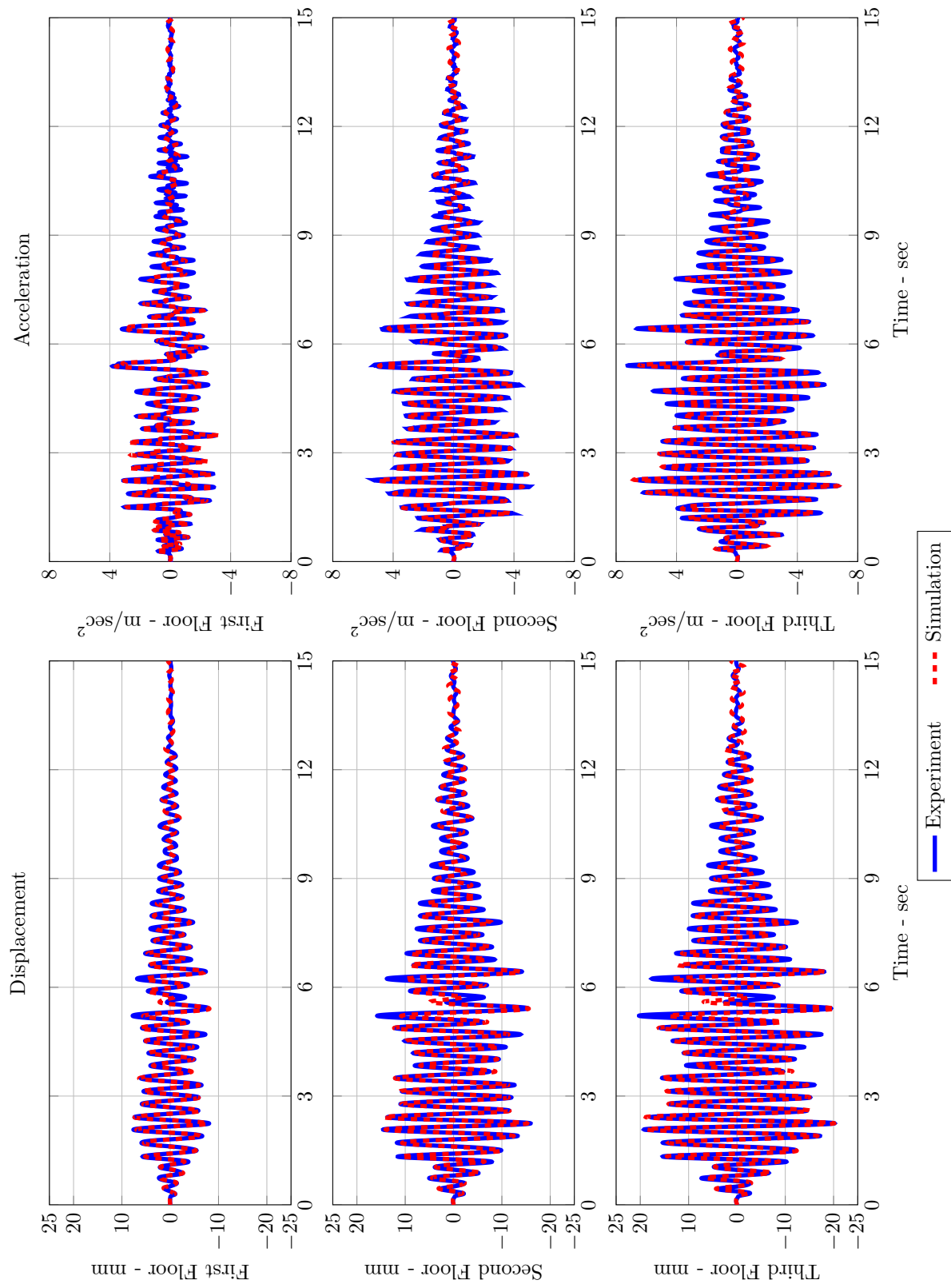


Figure 5.22: Morgan Hill Earthquake Comparison in Time Domain for POFF Case

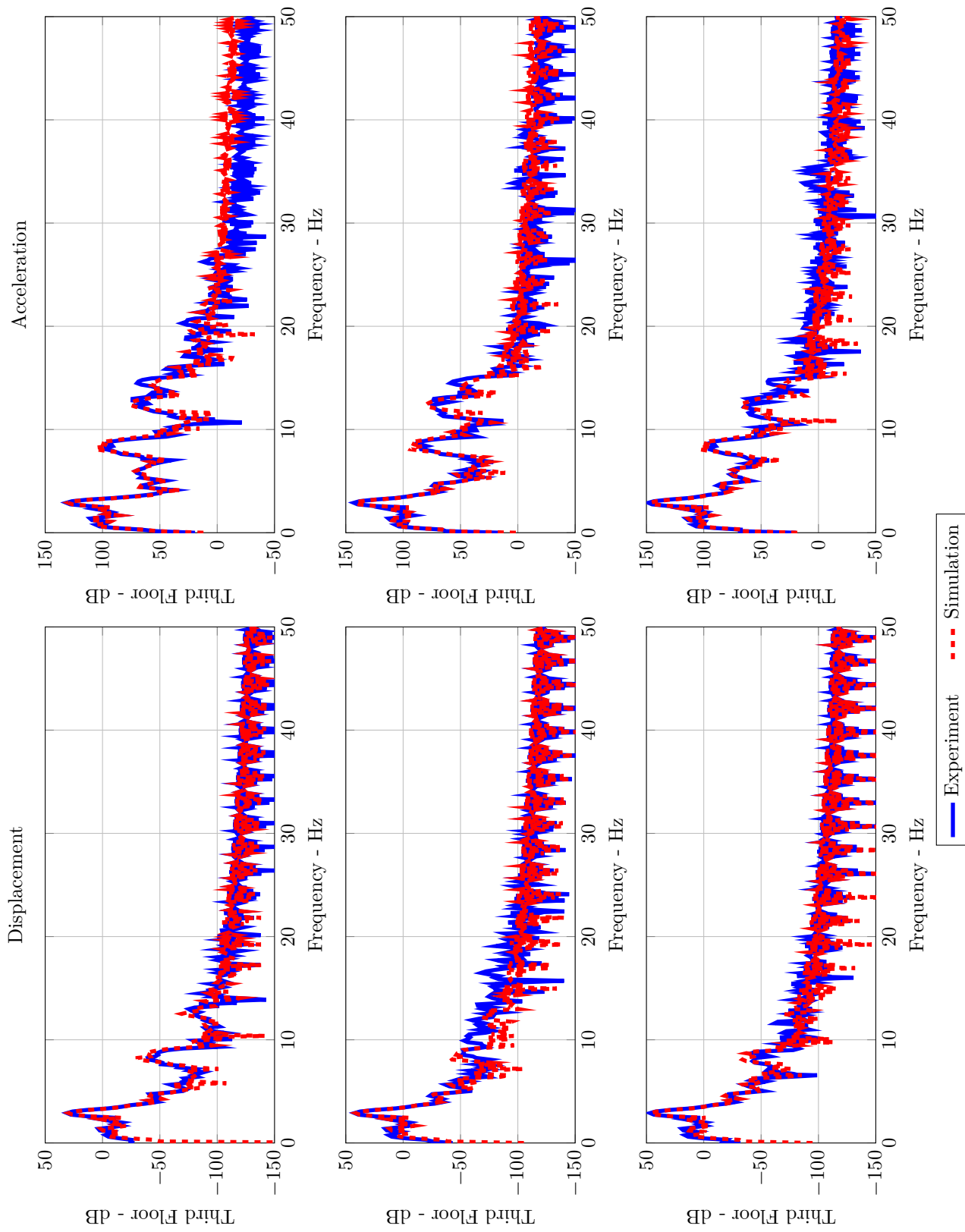


Figure 5.23: Morgan Hill Earthquake Comparison in Frequency Domain for POFB Case

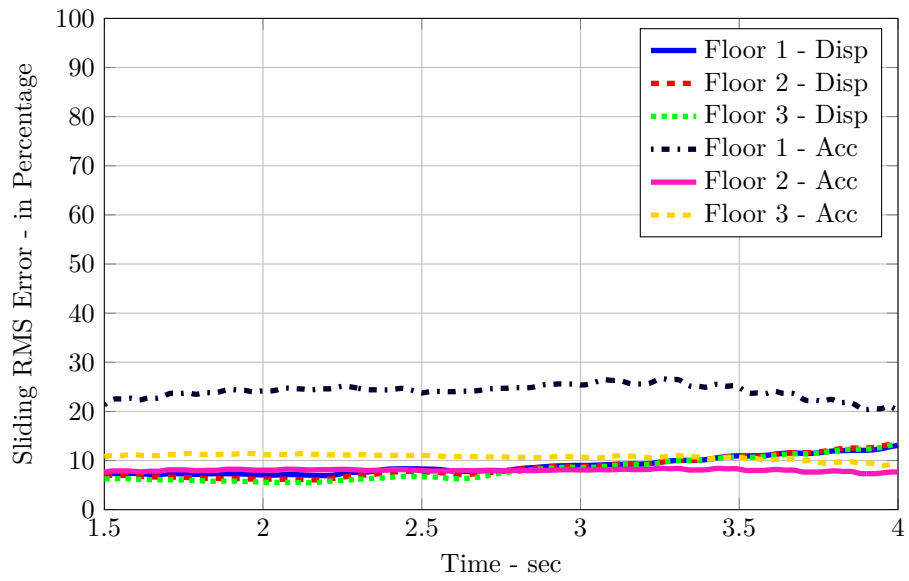


Figure 5.24: Moving RMS Error for Morgan Hill Earthquake POFF Case

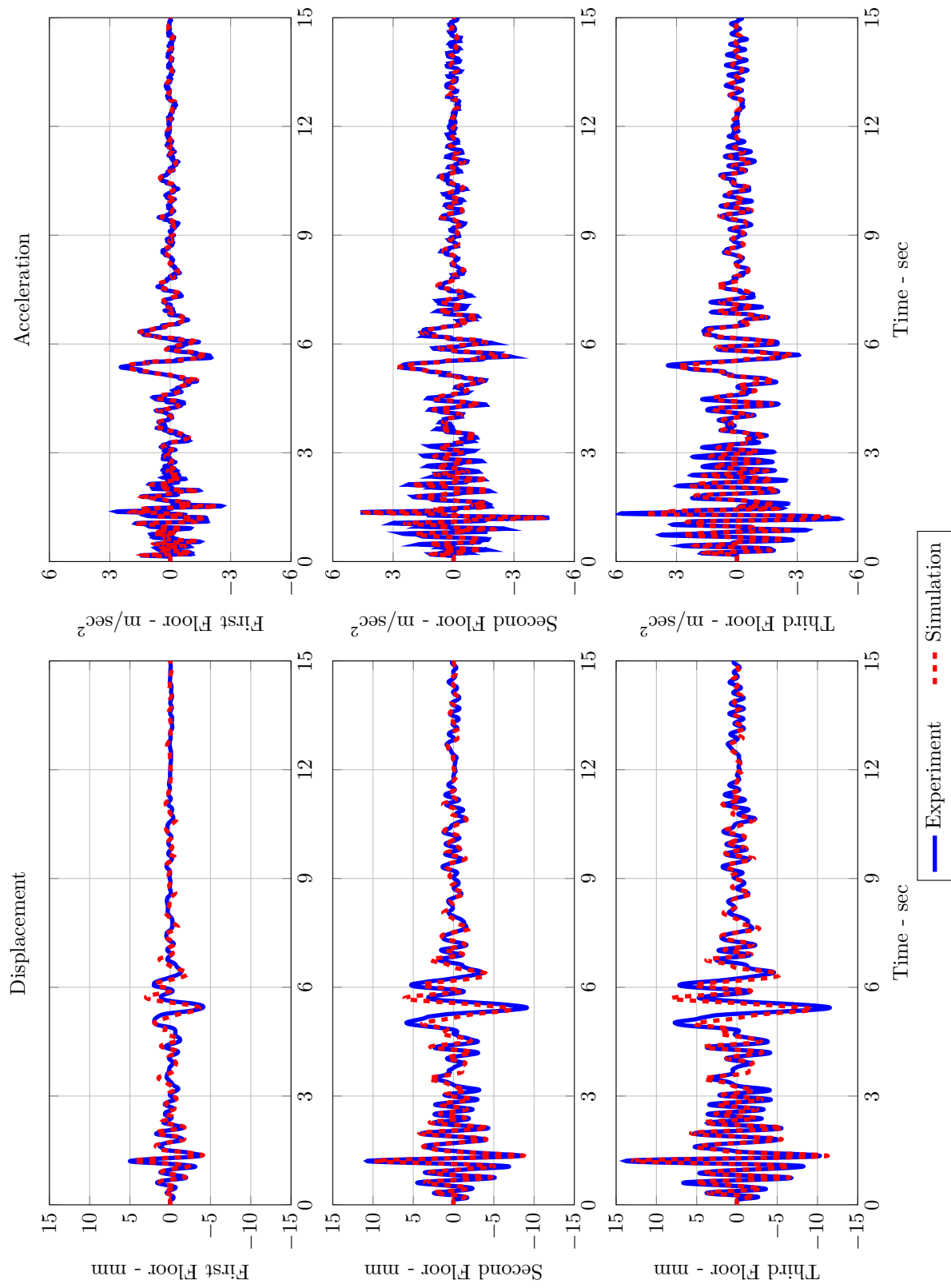


Figure 5.25: Morgan Hill Earthquake Comparison in Time Domain for PON Case

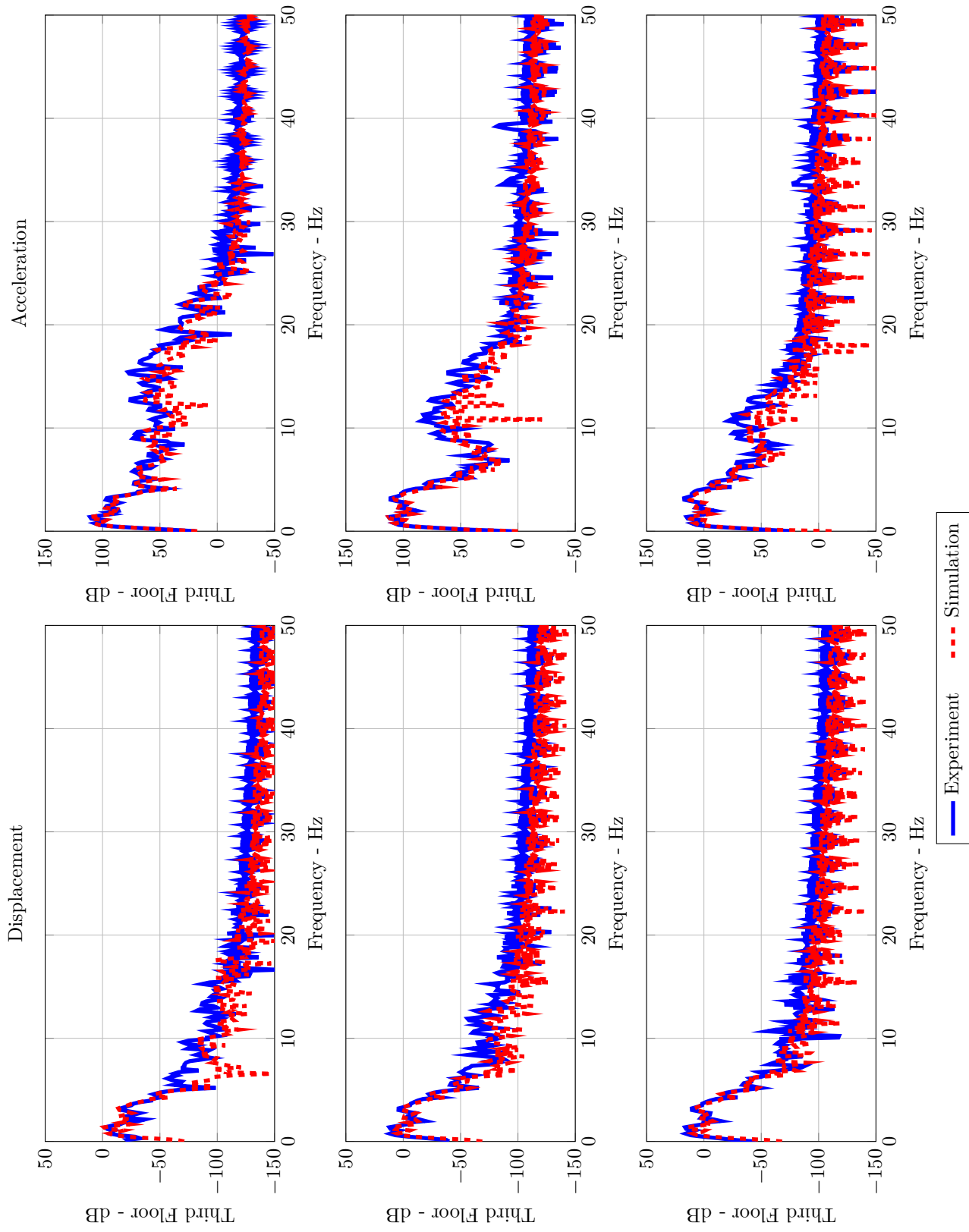


Figure 5.26: Morgan Hill Earthquake Comparison in Frequency Domain for PON Case

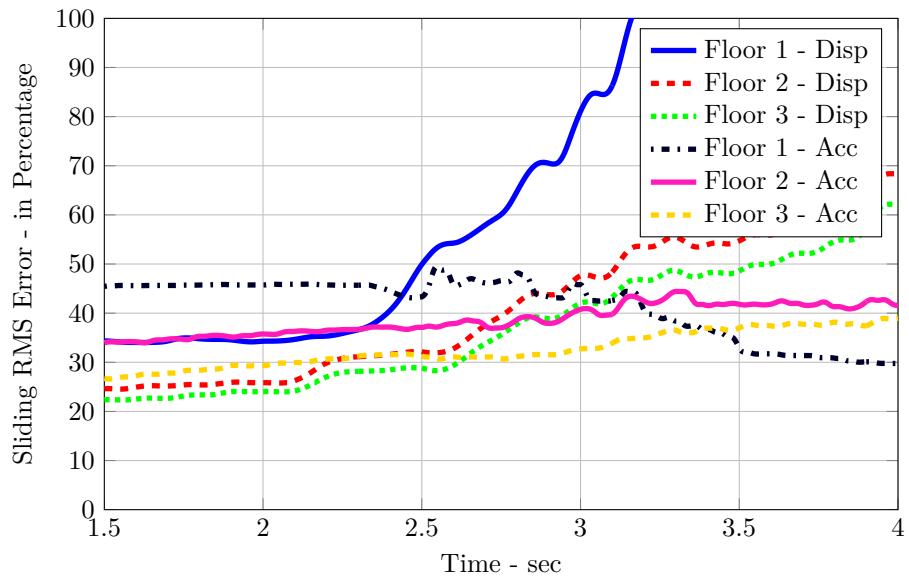


Figure 5.27: Moving RMS Error for Morgan Hill Earthquake PON Case

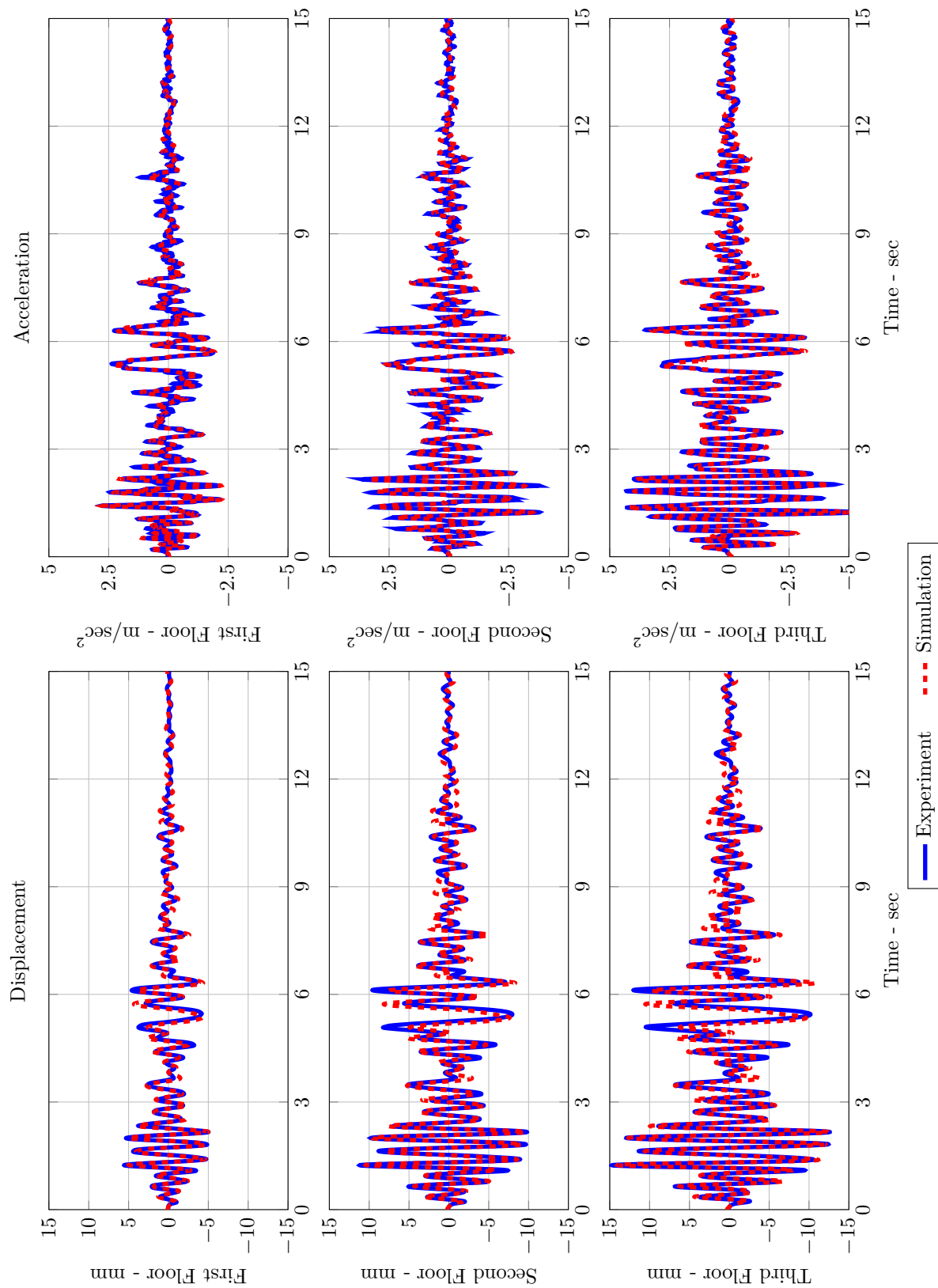


Figure 5.28: Morgan Hill Earthquake Comparison in Time Domain for SA Case

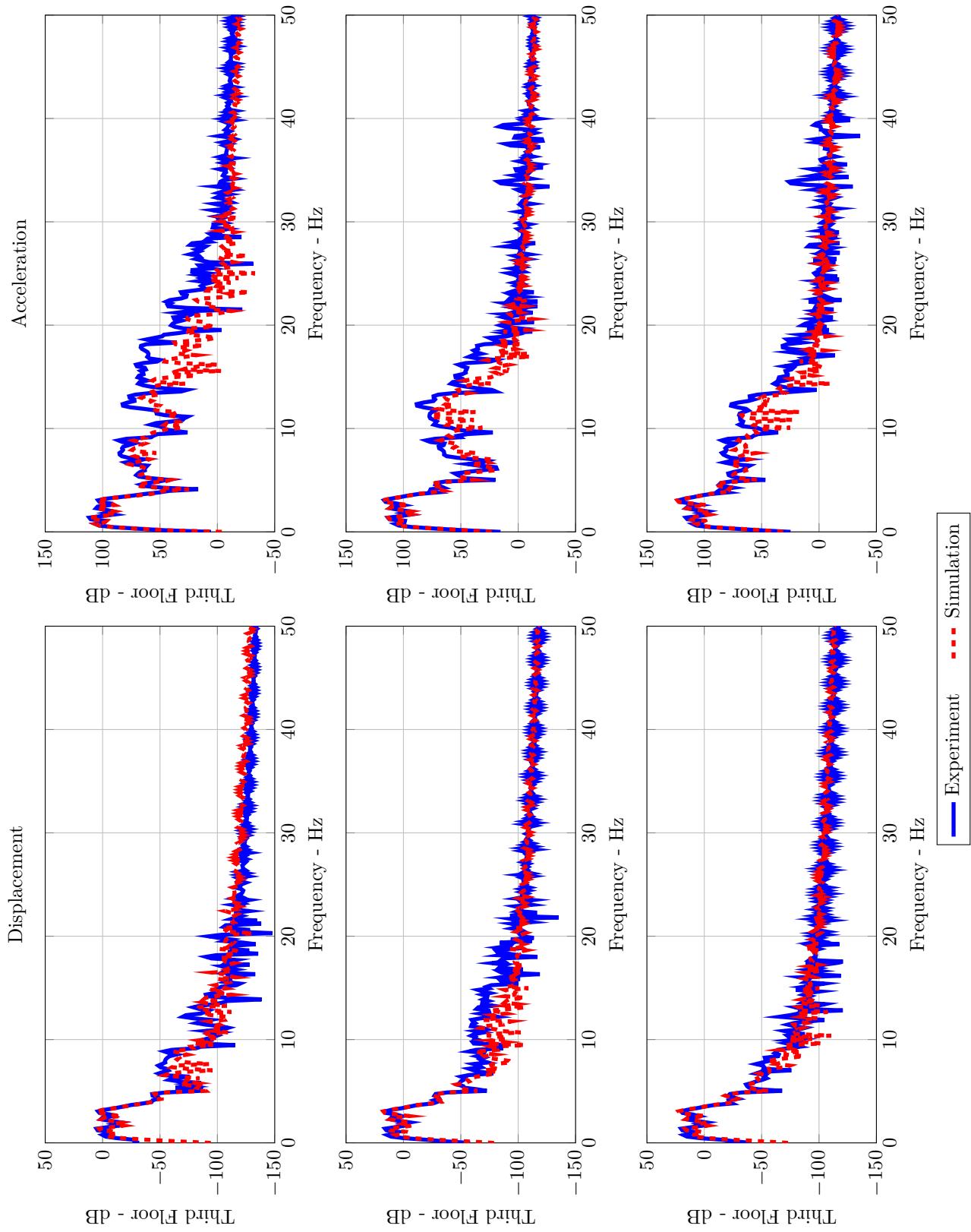


Figure 5.29: Morgan Hill Earthquake Comparison in Frequency Domain for SA Case

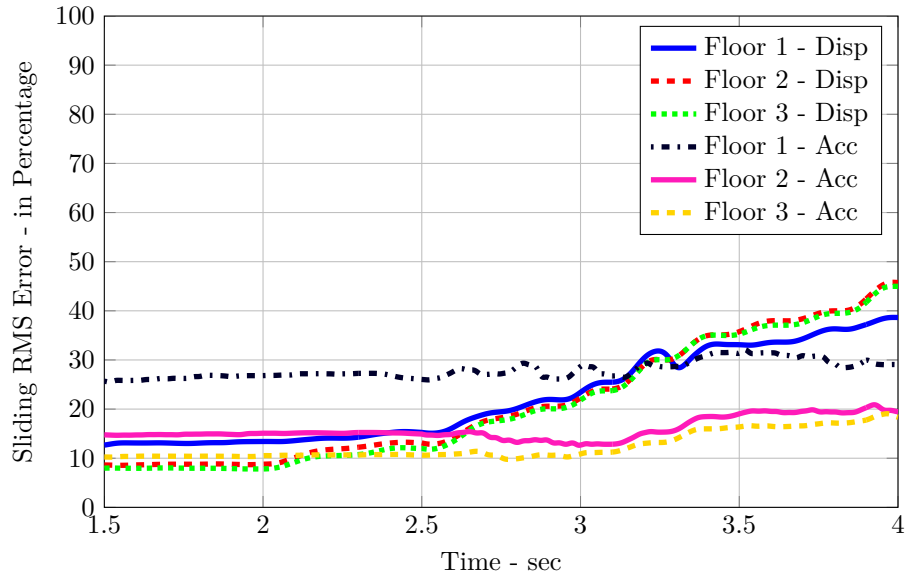


Figure 5.30: Moving RMS Error for Morgan Hill Earthquake POFF Case

5.3.4 Discussions

Considering POFF cases for all earthquakes, the average errors are found below 20%. However, for the PON cases, the errors elevated up to 60% for the first floor and 50% for the second and third floors. Three reasons can be related to the increased errors:

- i. In Chapter 4, it has been stated that the MR damper model has up to 18% of standard deviation error, both for POFF and PON cases. The force generated by the damper in POFF mode is small enough, it doesn't have a considerable impact in distorting structural responses. On the other hand, large PON forces are affecting structural responses notably. Consequently, it is justifiable to observe relatively large errors for PON case comparisons due to damper modeling error. Furthermore, the lessened error for SA case comparisons, where the level of force are between POFF and PON case,

Table 5.1: Evaluation Criteria for Pure Simulation Verification

Ground Motion	Controller	Location	Evaluation Criteria						Criteria Average
			J1	J2	J3	J4	J5	J6	
El Centro	POFF	First Floor	19.25	12.74	22.38	14.60	4.76	4.54	14.75
		Second Floor	19.12	10.28	14.35	5.70	4.61	3.32	10.81
		Third Floor	20.31	8.46	13.29	4.18	4.86	3.20	10.22
	PON	First Floor	43.25	43.35	37.19	24.62	8.44	6.39	31.37
		Second Floor	34.47	9.92	27.31	4.78	6.66	4.49	16.63
		Third Floor	34.51	13.61	21.89	16.02	6.77	4.23	18.56
	SA	First Floor	24.21	14.99	24.77	4.62	5.31	4.77	14.78
		Second Floor	20.36	4.32	17.11	12.90	4.31	3.17	11.80
		Third Floor	21.50	6.91	11.73	11.62	4.45	2.34	11.24
Kobe	POFF	First Floor	5.64	3.63	14.73	1.39	1.82	3.85	5.44
		Second Floor	6.25	6.00	5.87	7.67	2.01	1.83	5.56
		Third Floor	5.65	5.69	8.07	6.60	1.83	2.71	5.57
	PON	First Floor	62.47	27.22	38.44	10.18	13.25	6.12	30.31
		Second Floor	48.68	17.33	37.04	12.08	10.37	6.22	25.10
		Third Floor	46.17	16.36	26.86	25.98	10.13	4.64	25.10
	SA	First Floor	26.49	11.28	25.45	13.80	6.58	4.80	16.72
		Second Floor	27.28	7.90	16.85	3.54	6.78	3.82	12.47
		Third Floor	27.81	10.65	11.01	5.57	6.78	2.46	12.36
Morgan Hill	POFF	First Floor	9.26	3.38	23.24	7.14	2.59	5.98	9.12
		Second Floor	9.05	4.31	8.00	5.63	2.50	2.14	5.90
		Third Floor	8.69	1.96	10.73	4.40	2.38	2.98	5.63
	PON	First Floor	60.22	13.58	40.05	10.91	12.61	5.66	27.47
		Second Floor	37.92	4.87	36.44	6.96	8.86	8.02	19.01
		Third Floor	34.35	7.25	31.25	23.59	8.53	7.19	21.00
	SA	First Floor	18.46	6.07	25.16	5.35	4.03	4.90	11.81
		Second Floor	17.76	1.99	14.91	15.38	3.96	2.88	10.80
		Third Floor	17.26	2.15	11.52	7.25	3.75	2.51	8.39
EQ Average	POFF	First Floor	11.38	6.58	20.12	7.71	3.06	4.79	9.77
		Second Floor	11.47	6.86	9.40	6.33	3.04	2.43	7.42
		Third Floor	11.55	5.37	10.70	5.06	3.03	2.96	7.14
	PON	First Floor	55.31	28.05	38.56	15.23	11.43	6.06	29.72
		Second Floor	40.35	10.71	33.60	7.94	8.63	6.24	20.25
		Third Floor	38.35	12.41	26.67	21.86	8.48	5.35	21.55
	SA	First Floor	23.05	10.78	25.12	7.93	5.31	4.82	14.44
		Second Floor	21.80	4.74	16.29	10.61	5.02	3.29	11.69
		Third Floor	22.19	6.57	11.42	8.15	4.99	2.44	10.66

supports this claim.

- ii. It is observable from PSD comparisons that around the third mode of the structure, the curves are deviating from each other. MR damper is characterized specifically with a sine wave displacement of an amplitude of 5 mm at 2.9 Hz. It is possible that the damper model may not be successful in capturing force levels at higher frequencies.
- iii. In PON mode, the structural responses are diminished due to increased damping. However, it appears that for very small displacements, the first floor LVDT tends to stick, eventually causing faulty readings. This behavior is especially noticeable in the sliding RMS error plots.

The overall averaged errors reported in Table 5.1 are 7% to 10% and 10% to 15% for POFF and SA cases, respectively. For PON case, the first floor error is close to 30%, whereas for second and third floors, it is about 20%.

5.4 Conclusions

To compare and validate shake table responses with pure simulation results, the three story structure located at HIT with a MR damper attached to its first floor is tested. To perform the comparison successfully, system identification of the structure, characterization and modeling of the MR damper, integration of COC and selection of control parameters are carried out.

The global responses of the system to several ground motions such as relative displacements and absolute accelerations at each level are compared to pure simulation results for POFF, PON and SA cases. For the evaluation of the comparisons, peak, RMS, and sliding RMS errors are computed. In addition, PSD of the shake table and simulations responses are also presented.

In general, the pure simulations predicted shake table results. Further, in terms of displacements and accelerations, strong correlation is found between results. Tracking of the first floor displacements displayed elevated errors due to a hardware error, however, PSDs showed a good match in frequency domain. Overall, pure simulation results has proven to be successful in predicting shake table responses.

CHAPTER 6

VERIFICATION OF RTHS WITH SHAKE TABLE TESTS

In this chapter, a description of the experimental study to validate RTHS with shake table test is given. First, an accurate dynamic model of the actuator and an efficient control algorithm to compensate actuator dynamics, both of which are essential elements of successful RTHS, are introduced in Section 6.1. In Section 6.2, a general implementation of the RTHS is discussed. Next, in Section 6.3, results of RTHS are compared to shake table results. For all cases, error in relative displacement, absolute acceleration in the global sense of the structure is examined including other evaluation criteria discussed in Section 3.5. Finally, a summary of the chapter that interprets and concludes main findings in the comparisons is given in Section 6.4.

A successful comparison between shake table experiments and RTHS depends on the following tasks: (i) modeling of the existing test structure that will serve as the analytical substructure in the RTHS scheme, (ii) characterization of the MR damper which will be used as the physical substructure of RTHS, and

(iii) actuator tracking controller design, particularly to ensure stable and high performance RTHS. Steps (i) and (ii) were already introduced in the previous chapters. In the following sections, system modeling and actuator tracking are also discussed. Later, in the subsequent sections, results of RTHS implemented based on these previously introduced concepts are studied.

6.1 Design of Tracking Controller to Compensate Actuator Dynamics

The transfer function system of a hydraulic actuator, G_{x_m, x_c} can be idealized by servo-hydraulic system, including servo-valve and servo-valve controller, as well as the actuator and specimen. The system can be represented in block diagram as in Fig. 6.1. In this diagram, x_c is the command input, x_m is the measured output and f is the force applied by the actuator to the specimen. An inner loop PID control is often provided within the servo-valve controller that promises basic tracking of command. Although this inner loop control is adequate for slow-rate tests and non-real-time hybrid simulations, strict requirements of RTHS, such as low time delay between desired input and measured output, make the PID control meager. To improve the performance of the actuator control, actuator dynamics should be compensated via a proper control scheme.

In the following subsections, modeling of actuator and development of a novel *Robust Integrated Actuator Control* (RIAC) algorithm is briefly discussed.

The performance of servo-hydraulic system can be extended by introducing an outer loop control algorithm that ensures tracking of desired response as simplified in Fig. 6.2. In this diagram, x_d is the desired input, and in a RTHS setting, it can be considered as a response of numerical substructure to be imparted to the physical substructure through actuator.

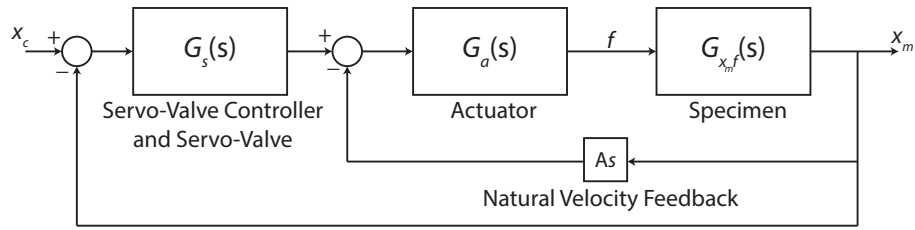


Figure 6.1: Servo-Hydraulic System Diagram

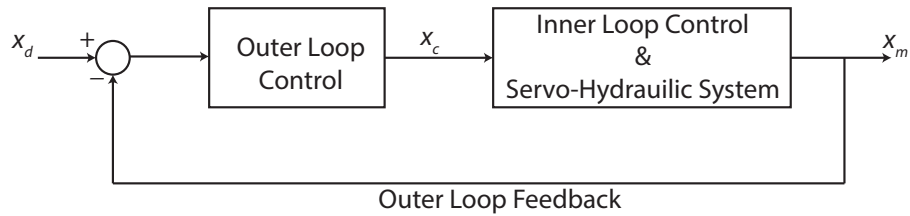


Figure 6.2: Introduction of Outer Loop Control

6.1.1 Modeling of Servo-hydraulic Actuator

The actuator dynamics often manifest as a drop in frequency response magnitude and as lag in phase, undesirable for conducting successful RTHS. Developing an effective compensation control system depends on an accurate model that describes such dynamics over the operational frequency content of the target structure. For the purpose stated above, system identification for the HIT and Purdue setups are discussed.

HIT Setup

The hydraulic system at HIT is identified with MR damper attached using a 0–100 Hz band-limited white noise input signal in open loop control setting. The resulting response of the actuator system is stored as the measurement data. The time domain response of the system is shown in Fig. 6.3.

Since the loading capacity of the actuator is very large compared to the MR damper maximum force, the resulting transfer functions for passive-off and

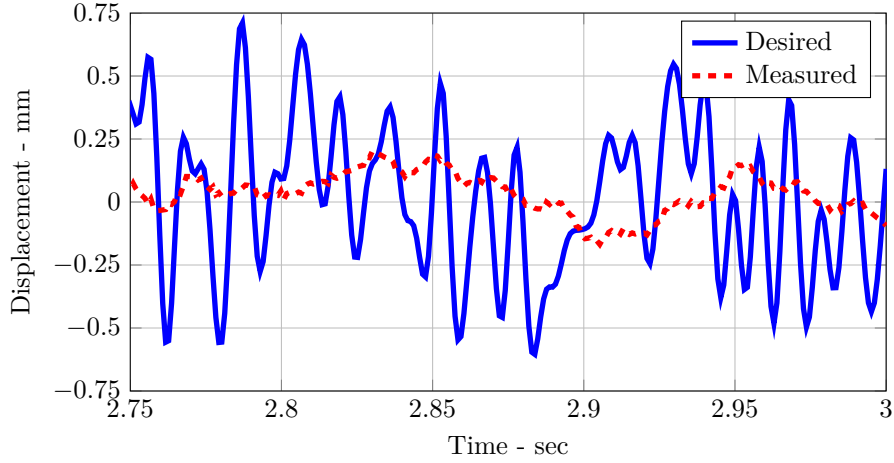


Figure 6.3: Open Loop System Input and Output in Time Domain for HIT Setup

-on control cases for the damper are assumed to be same. The plant model is determined using *invfreqz* command in MATLAB. The zero-pole system is written as a fourth order transfer function as given Eq. (6.1):

$$G_{x_m, x_c, HIT} = \frac{1.5091 \times 10^8}{s^4 + 281.795s^3 + 6.6017 \times 10^4 s^2 + 6.0044 \times 10^6 s + 1.4966 \times 10^8} \quad (6.1)$$

The frequency domain response including identified transfer function of the open loop system is shown in Fig. 6.4. It is observed that there is drop in gain (~ -0.5 dB/Hz) and lag in the phase (~ -6.75 dB/deg) as the frequencies increase.

Purdue Setup

Purdue actuator is identified with MR damper attached using a 0–100Hz band-limited white noise signal when damper is at passive-on and -off mode. The time domain response of the system is shown in Fig. 6.5.

Two transfer functions are developed from desired input to measurement

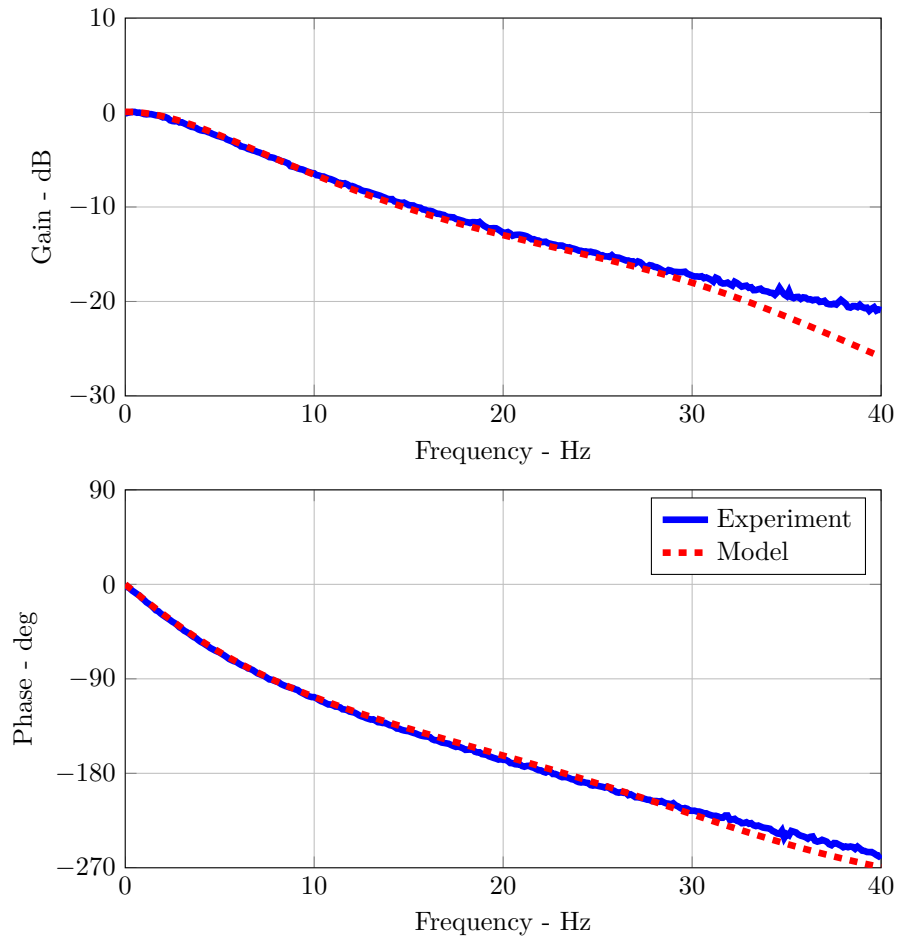


Figure 6.4: Frequency Response and Identified Model of the Open Loop System for HIT Setup

output for each case. Since the Purdue damper is relatively small, the effect of the damper mode on the transfer functions are noticeable. To minimize uncertainties due to this behavior, a new transfer function by averaging passive- on and -off results are taken as the final transfer function to be modeled. The

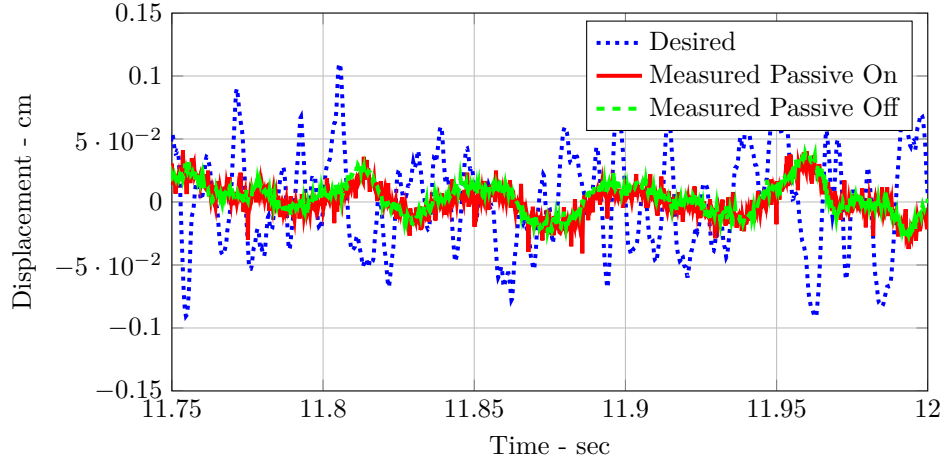


Figure 6.5: Open Loop System Input and Output in Time Domain for Purdue Setup

resulting zero-pole systems are written as given in Eq. (6.2):

$$G_{x_m, x_c, OFF, Purdue} = \frac{3.12 \times 10^9}{s^4 + 517.47s^3 + 3.008 \times 10^5 s^2 + 5.49 \times 10^7 s + 3.17 \times 10^9} \quad (6.2a)$$

$$G_{x_m, x_c, ON, Purdue} = \frac{4.70 \times 10^9}{s^4 + 639.55s^3 + 3.50 \times 10^5 s^2 + 7.51 \times 10^7 s + 4.79 \times 10^9} \quad (6.2b)$$

$$G_{x_m, x_c, AVG, Purdue} = \frac{3.91 \times 10^9}{s^4 + 578.51s^3 + 3.25 \times 10^5 s^2 + 6.50 \times 10^7 s + 3.98 \times 10^9} \quad (6.2c)$$

The frequency domain response including identified transfer functions of the open loop system is shown in Fig. 6.6. The average transfer function shows a drop in gain (~ -0.3 dB/Hz) and lag in the phase (~ -4.5 dB/deg) for the actuator.

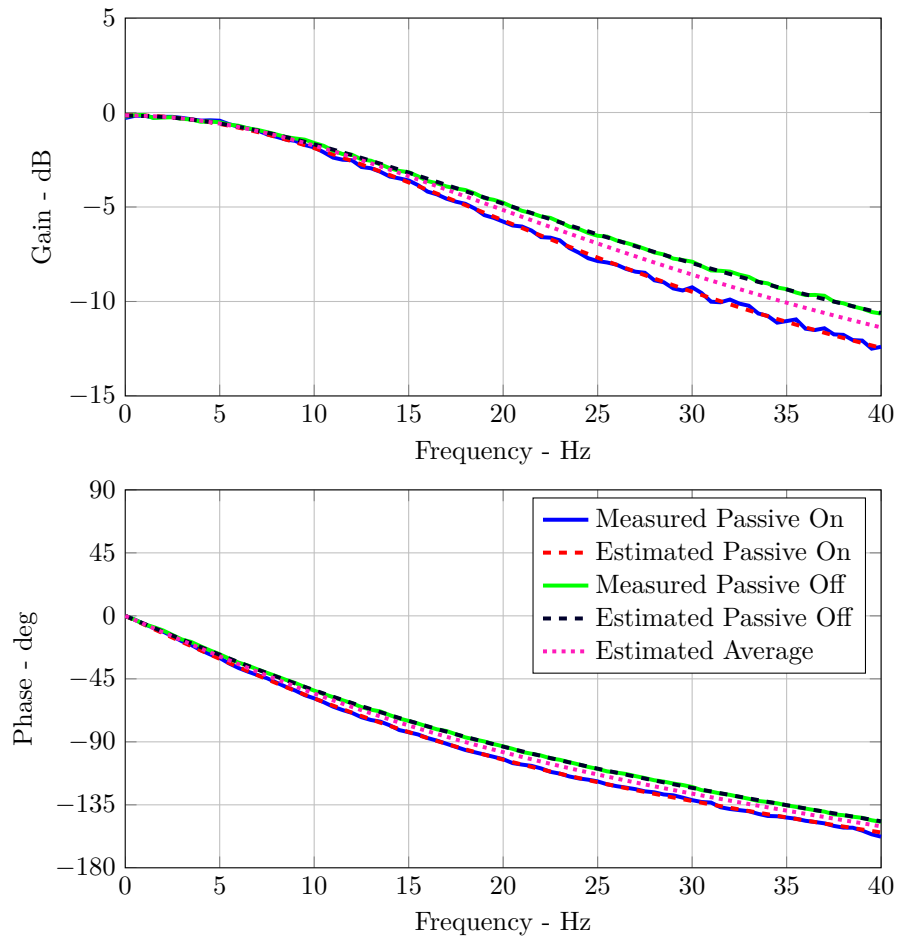


Figure 6.6: Frequency Response and Identified Model of the Open Loop System for Purdue Setup

6.1.2 Control Scheme for Actuator Tracking

As stated before, a novel compensation method, RIAC is used as the outer loop control to track desired displacement. RIAC integrates three key components: (i) loop shaping feedback control based on H_∞ optimization, (ii) a Linear Quadratic Estimator (LQE) block for minimizing noise effect and (iii) a feed-forward block for reducing small delay. The combination of these components provides

flexibility in controller design to accommodate setup limits while preserving the stability. A block diagram of the controller is illustrated in Fig. 6.7. RIAC is described in detail by [Ou et al. \(2014\)](#).

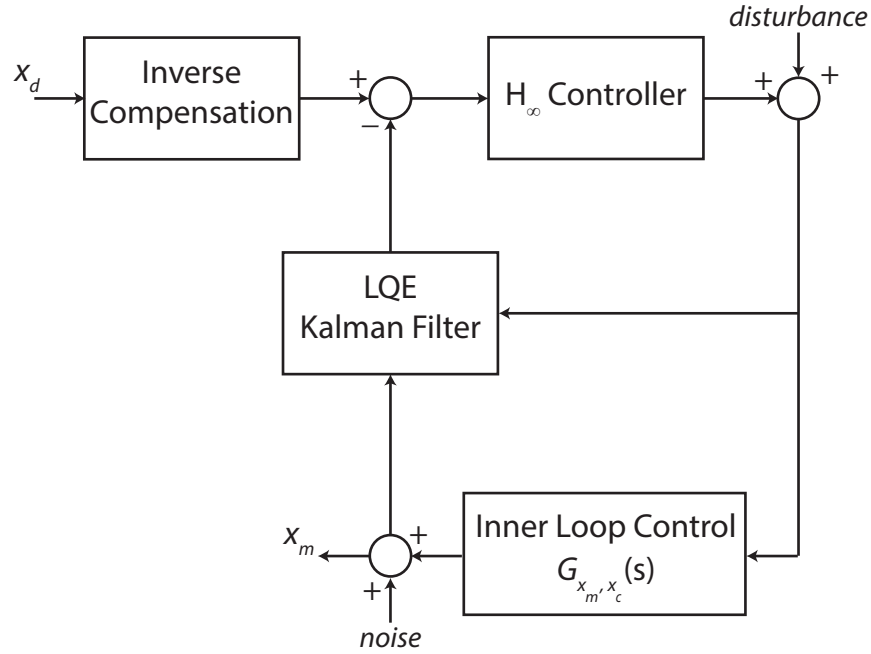


Figure 6.7: RIAC Control Block Diagram

Loop shaping feedback control was first introduced by [Gao et al. \(2013a\)](#). By nature, H_∞ controller has a trade off between performance and sensitivity. The controller has limitations in performing perfect tracking while attenuating high frequency noise. A deterioration in performance can manifest when the noise/signal ratio in the system is high. To reduce the impact of noise and improve phase response efficiently, a Kalman filter is integrated into RIAC. Considering the small residual delay may still exist, to further enhance the efficiency of the RIAC, an inverse compensation algorithm proposed by [Chen and Ricles \(2009\)](#) is implemented.

RIAC can be applied to any servo-hydraulic system regardless the size or

flow limitation of the actuator. In the following section, performance of the controller for HIT and Purdue setups is presented.

6.1.3 Verification of Controller

The performance of the actuator motion controller can be assessed by deriving the closed-loop system transfer function from desired and measured signals. Furthermore, the effect of the size and speed of the actuator on the controller efficiency, both large-size HIT and small-size Purdue actuators are tested. To obtain the transfer function, a band limited white noise bounded with 0-20 Hz is given to the actuators for 30 seconds in RIAC controlled closed loop setting. The transfer function is then compared to unity gain. In Figs. 6.8 and 6.9, HIT and Purdue closed loop transfer functions are presented. For both actuators, an optimal performance close to unity gain is obtained. Ultimately, it is shown that RIAC can be used for two completely different actuators.

In time domain, RMS errors between desired and measured signals for both actuators varied in the range of 3% to 10%.

6.2 RTHS Implementation

Experimental RTHS setup at IISL has been previously discussed in Section 2.5. In this section, the RTHS implementations is explained thoroughly.

As shown in Fig. 6.10, based on the given ground excitation, analytical substructure simulated in real-time by MATLAB/xPC generates global responses. Only the first floor displacement, which is compensated with RIAC, is sent to the actuator to engage the MR damper. Eventually, MR damper produces a force response to the given displacement which is fed back to the analytical substructure for the next time step.

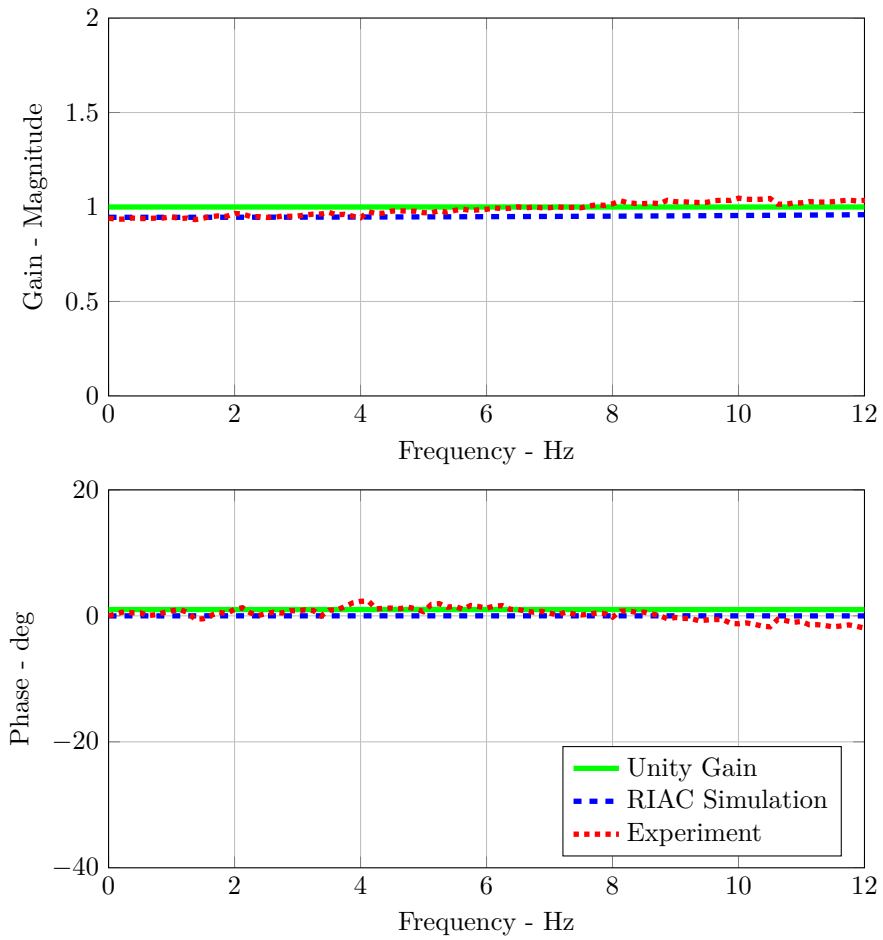


Figure 6.8: Performance of RIAC for HIT Actuator

A simplified implementation of RTHS configuration in MATLAB/Simulink is provided in Fig. 6.11.

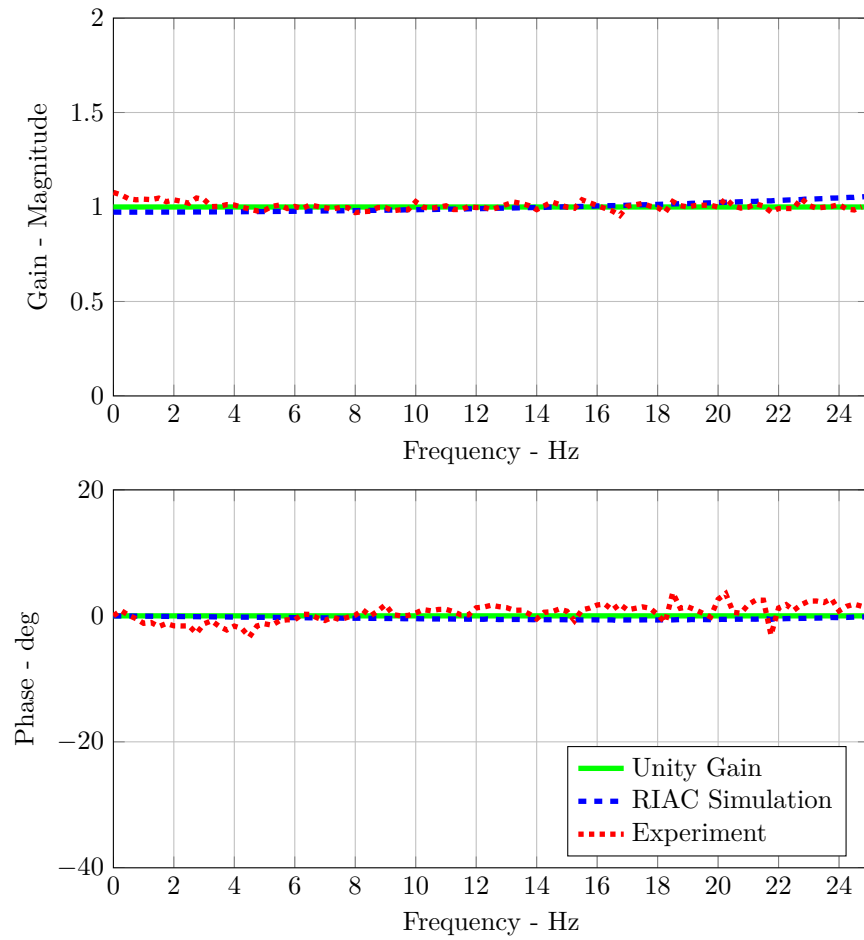


Figure 6.9: Performance of RIAC for Purdue Actuator

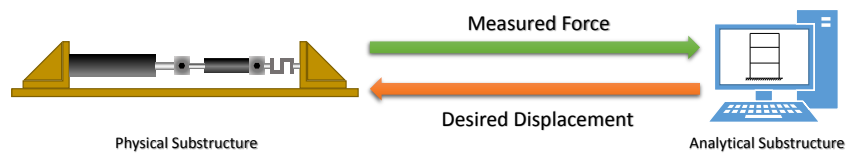


Figure 6.10: Communication between Physical and Analytical Substructure in a RTHS Frame

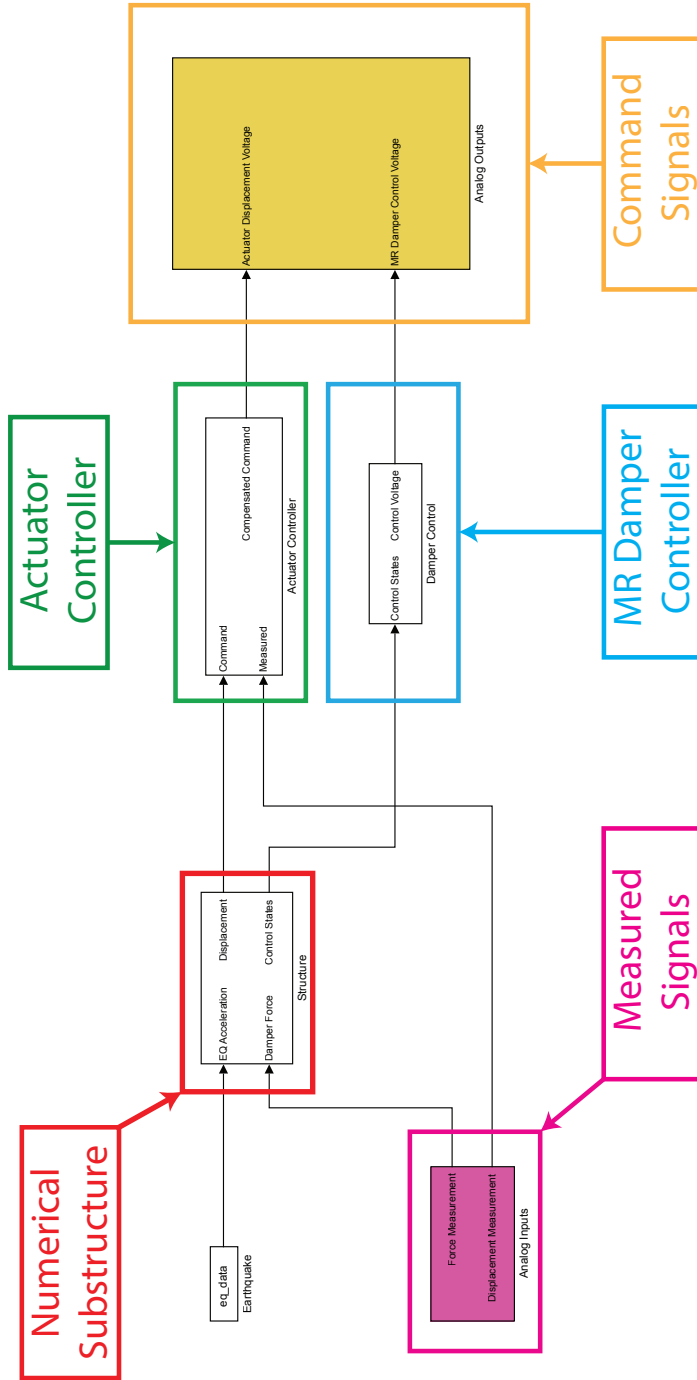


Figure 6.11: A Representative Simulink Model of the RTHS Simulation

6.3 Comparison of Shake Table Test Responses with RTHS Results

In this section, RTHS conducted at Purdue is compared to the shake table tests performed at HIT. The experimental plan for the validation of the RTHS is focused on simulating the seismically-excited three story structure while testing the damper device physically at passive on/off and semi-active control modes. Results obtained from RTHS are compared to shake table responses and accuracy of the RTHS configuration is assessed with evaluation criteria proposed in Chapter 3.

As in Chapter 5, passive on/off and semi-active control cases are considered for the comparison. Excitation input to the structure in RTHS setup is selected as El Centro, Kobe and Morgan Hill earthquakes measured by two accelerometers placed on the shake table. No filtering is applied to the ground accelerations. A sampling and integration rate of 5000 Hz is selected for the RTHS for a fair comparison.

6.3.1 El Centro

In this section, results between shake table and RTHS are compared for El Centro earthquake. Passive-off (POFF), -on (POFF) and semi-active (SA) cases are considered for the comparisons.

Passive-off

Displacement and acceleration comparisons are given in Figs. 6.12 and 6.13. RMS and peak response errors are tabulated in Table 6.1 in percentage. In addition, moving RMS errors are illustrated in Fig. 6.14.

Compared to shake table-pure simulation comparisons, the reported peak

errors for floor accelerations and displacements are slightly large and ranging from 10 % to 30 %. On the other hand, the RMS error are lower and varying from 4 % to 15 %. Range-normalized RMS errors for RTHS and pure simulations are close to each other.

Passive-on

For PON case, displacement and acceleration comparisons are given in Figs. 6.15 and 6.16. Related errors are tabulated in Fig. 6.17 and Table 6.1.

As observed in shake table-pure simulation results, there is a deviation in the first floor displacement responses concentrated at around 6–9 seconds.

RMS and peak response errors for floor accelerations and displacements are lower than pure simulation errors and are ranging from 2 % to 35 %. The criteria-averaged RMS error is varying from 14 % to 20 %. It has been noted that the first floor errors are smaller than those of pure simulation case, possibly due to the fact that physical MR damper is showing better performance than its analytical model despite the difference in the force levels between HIT and Purdue dampers.

Semi-active

The comparisons for SA case are given in Figs. 6.18 to 6.20 and Table 6.1.

As observed in the previous chapter, the reported averaged errors for SA case are between PON and POFF cases. RMS and peak response errors vary from 3 % to 238 % and the criteria-averaged RMS error is around 10 %.

6.3.2 Kobe

In this section, results between shake table and pure simulations are compared for Kobe earthquake. POFF, PON and SA cases are considered for the comparisons.

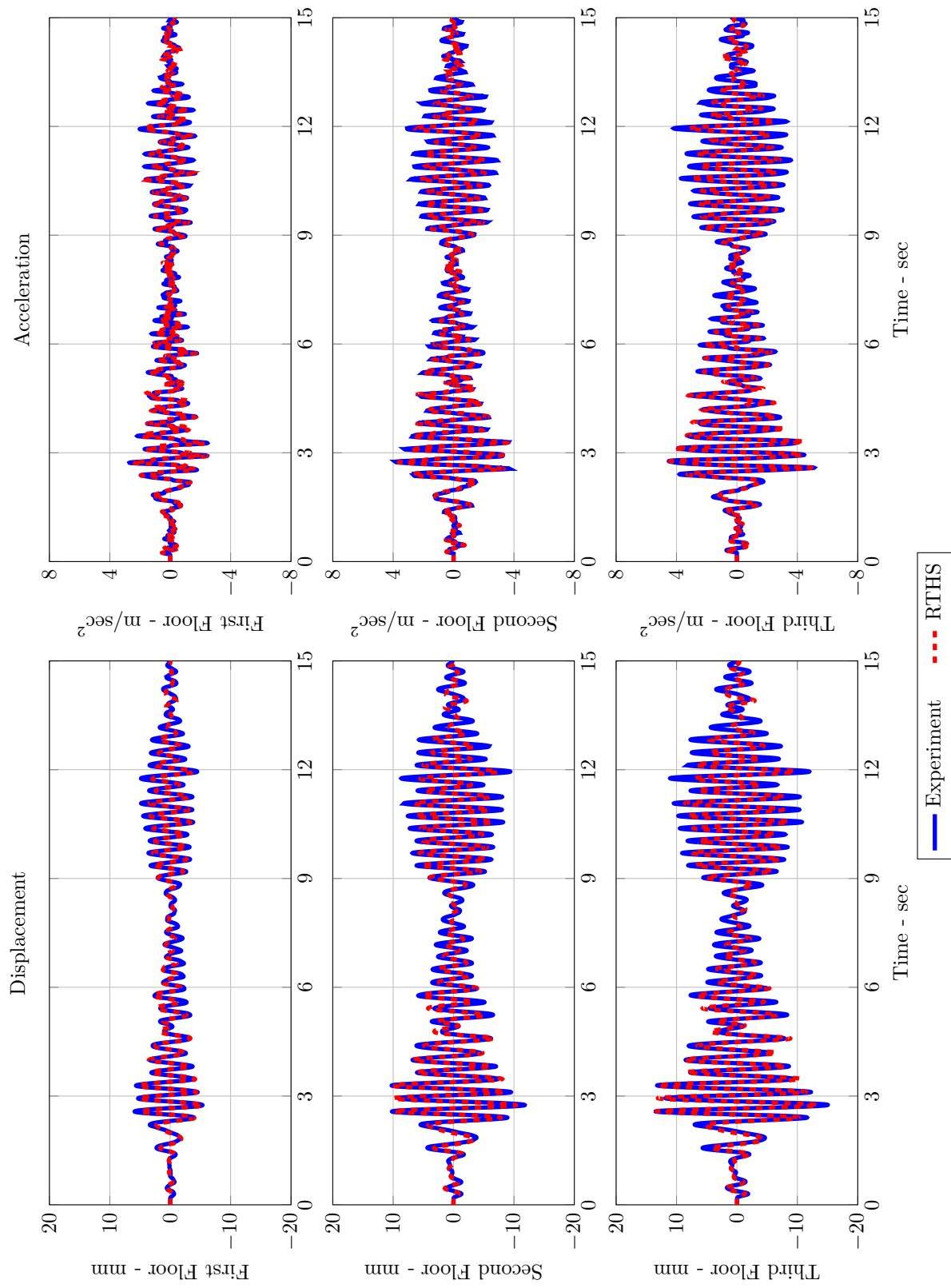


Figure 6.12: El Centro Earthquake Comparison in Time Domain for POFF Case

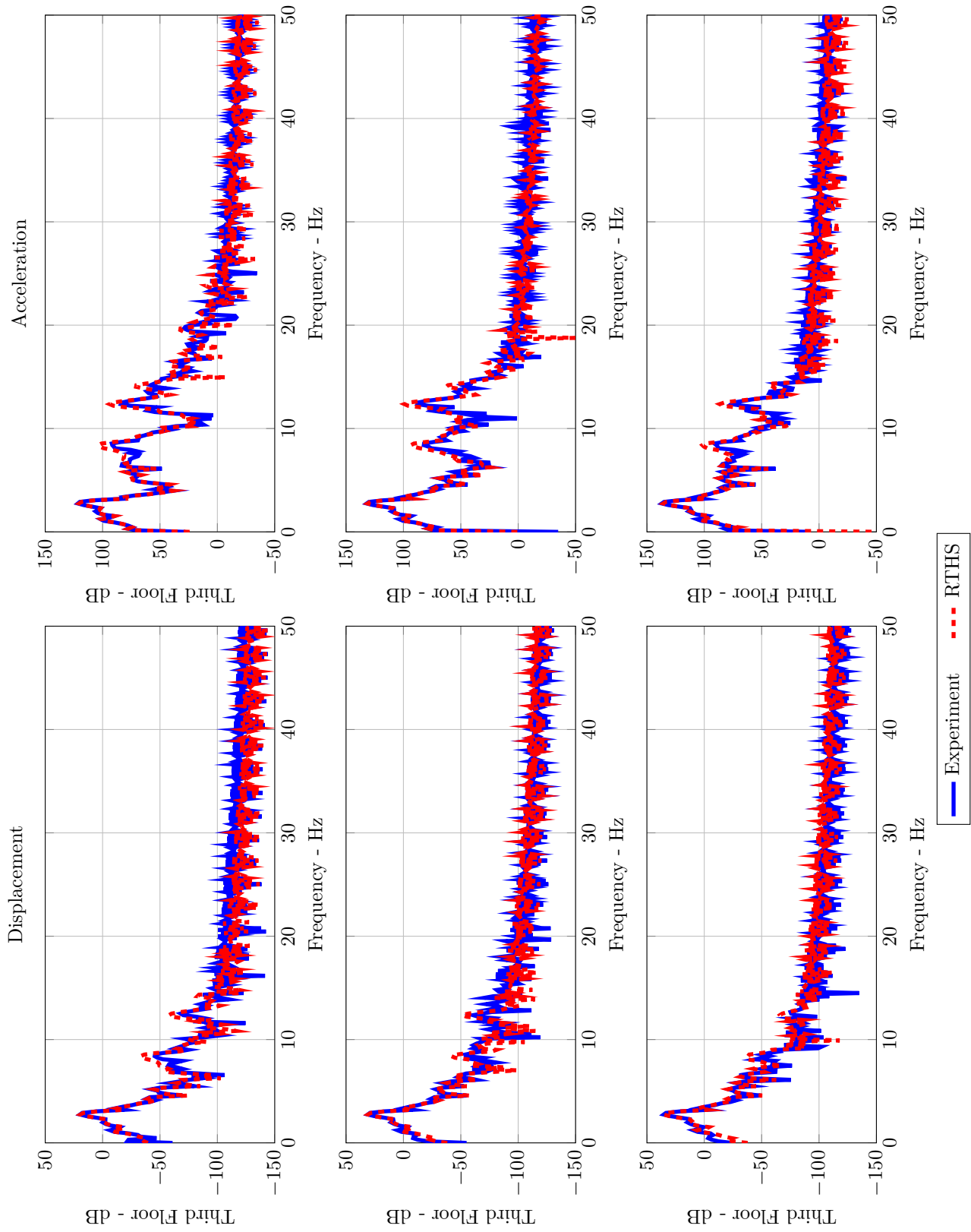


Figure 6.13: El Centro Earthquake Comparison in Frequency Domain for POFF Case

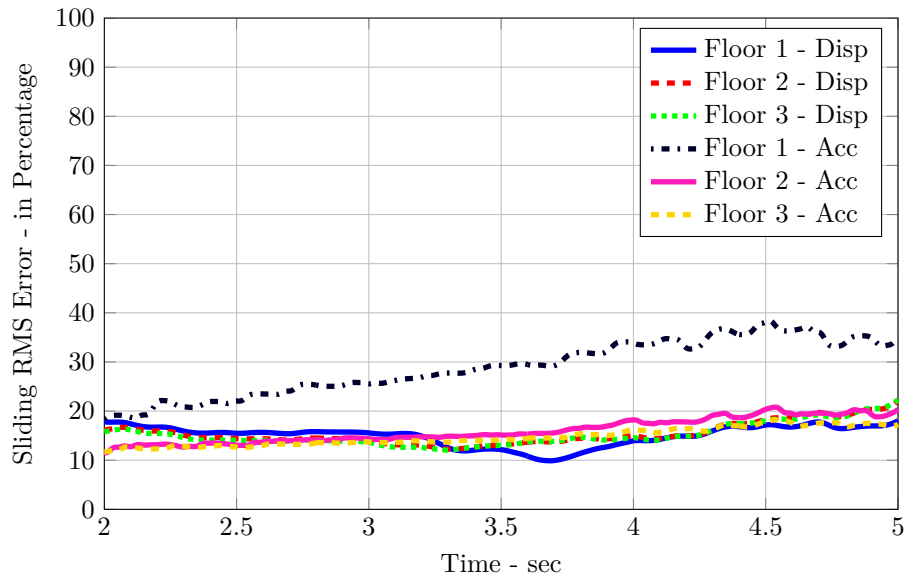


Figure 6.14: Moving RMS Error for El Centro Earthquake POFF Case

Passive-off

The related response comparisons are given in Figs. 6.21 and 6.22. The errors observed for this case are higher than pure-simulation results. The differences between Purdue and HIT damper POFF forces can be held accountable for this elevated disturbances.

Passive-on

PON case comparisons, error tables and moving RMS error plot are given in Figs. 6.17, 6.24 and 6.25 and Table 6.1.

For this case, RMS and peak response errors range from 5% to 50% which are lower than pure simulation comparisons. Likewise, the criteria-averaged errors are concentrated around 20%, which are also smaller compared to pure simulation errors.

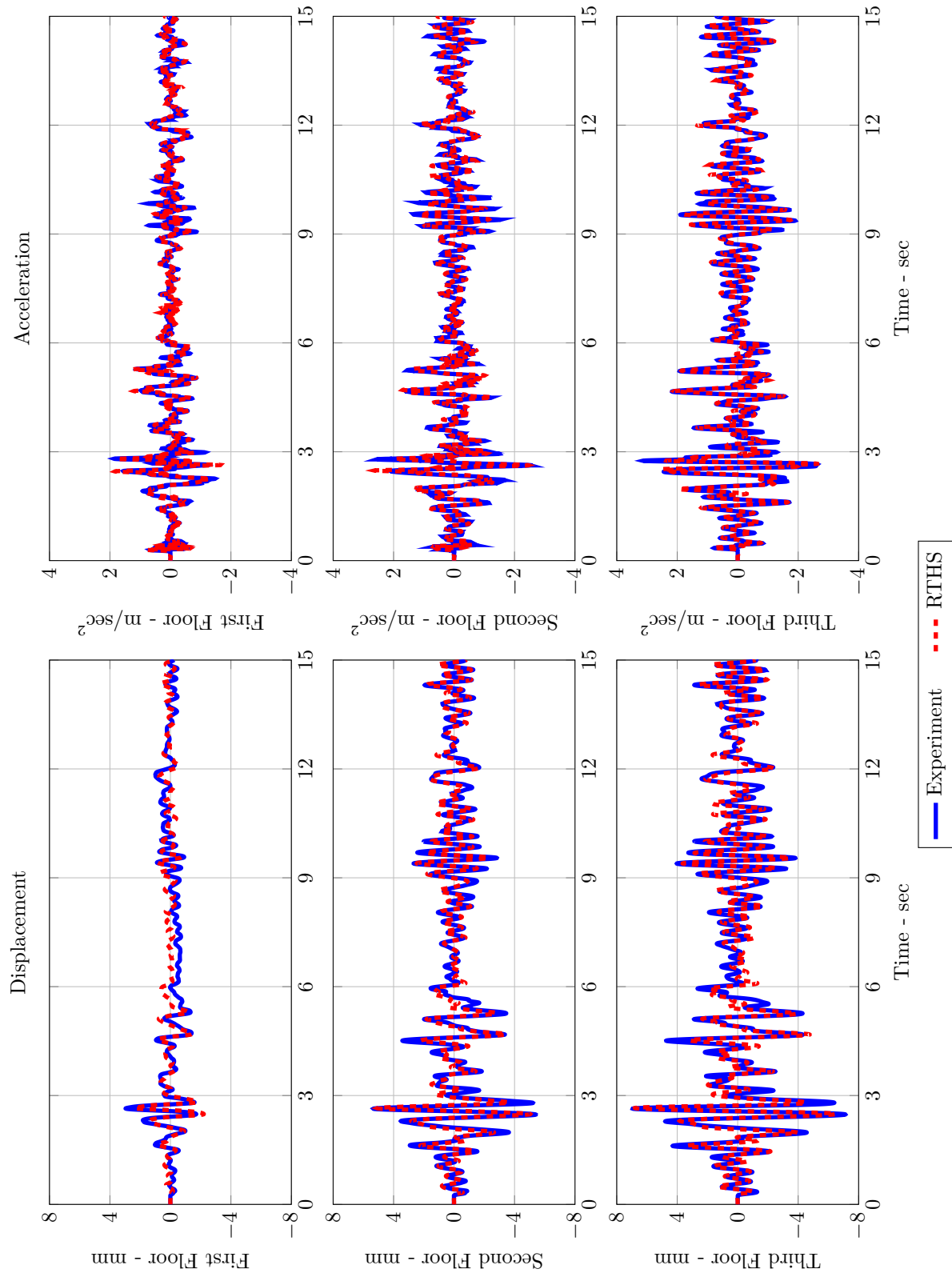


Figure 6.15: El Centro Earthquake Comparison in Time Domain for PON Case

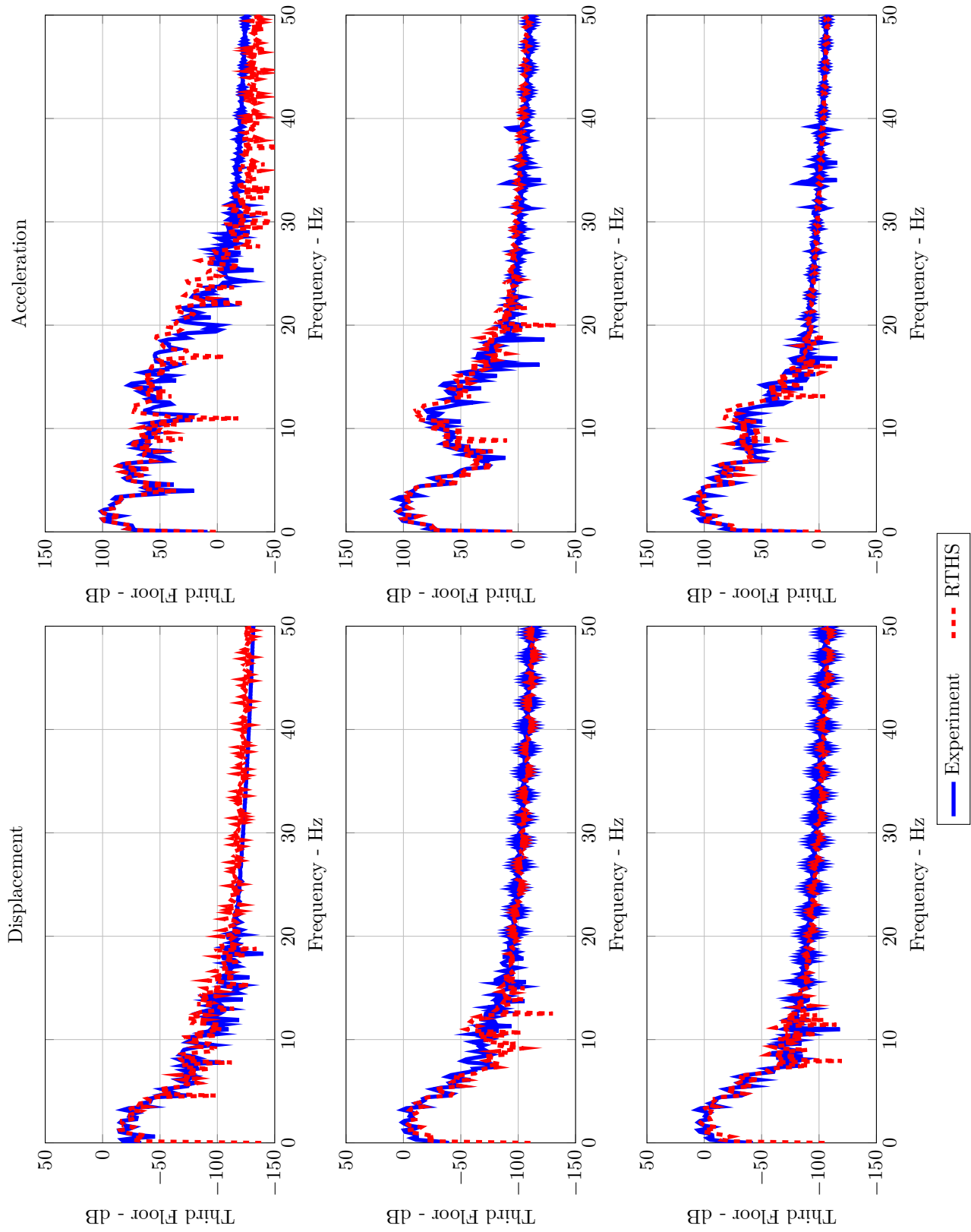


Figure 6.16: El Centro Earthquake Comparison in Frequency Domain for PON Case

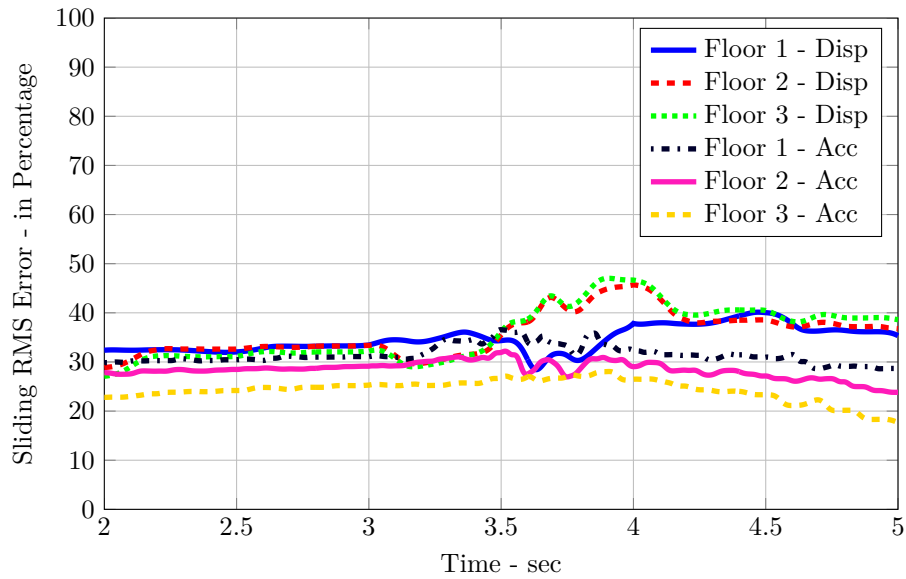


Figure 6.17: Moving RMS Error for El Centro Earthquake PON Case

Semi-active

In Fig. 6.27 and Fig. 6.28, SA case comparisons are presented. The reported errors and criteria-averaged errors are similar to pure simulation comparisons and in the range 4% to 27% and 12% to 16%, respectively.

6.3.3 Morgan Hill

In this section, results between shake table and pure simulations are compared for Morgan Hill earthquake. POFF, PON and SA cases are considered for the comparisons.

Passive-off

Time- and frequency-domain comparisons for POFF case are provided in Figs. 6.21 and 6.22. The reported errors and moving RMS errors are in the range of 5% to 14%. The averaged errors are nearly 10% for all criteria.

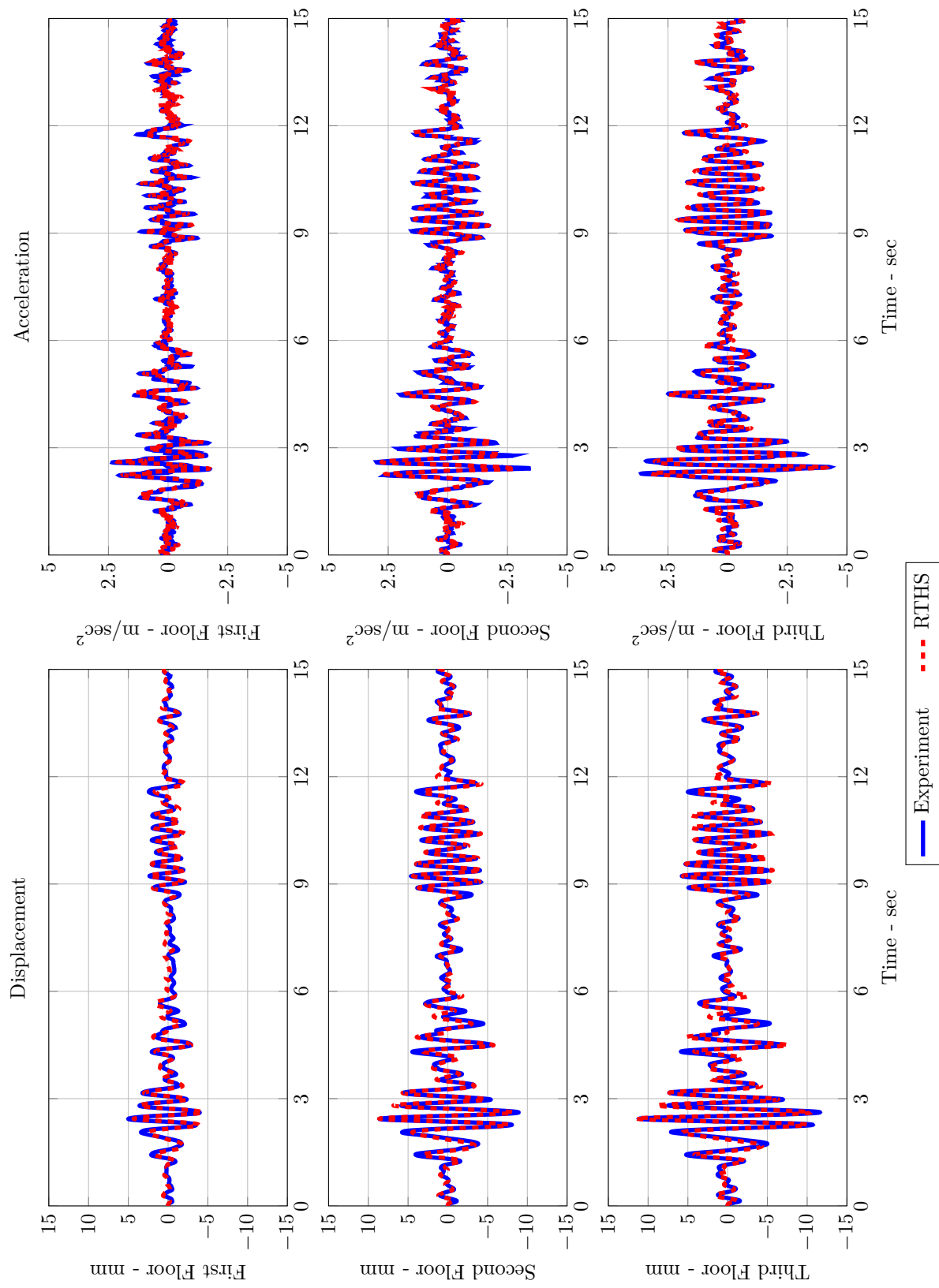


Figure 6.18: El Centro Earthquake Comparison in Time Domain for SA Case

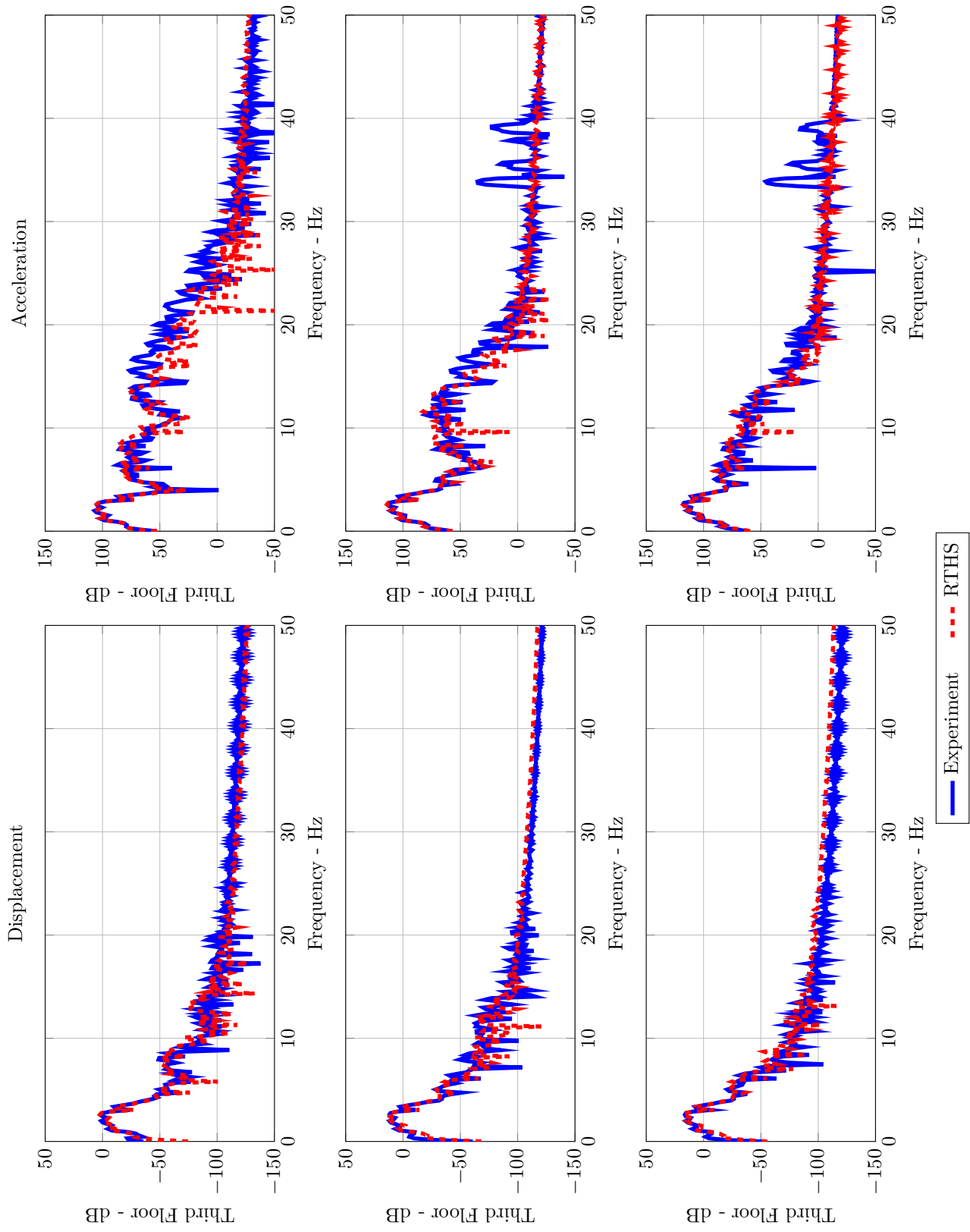


Figure 6.19: El Centro Earthquake Comparison in Frequency Domain for SA Case

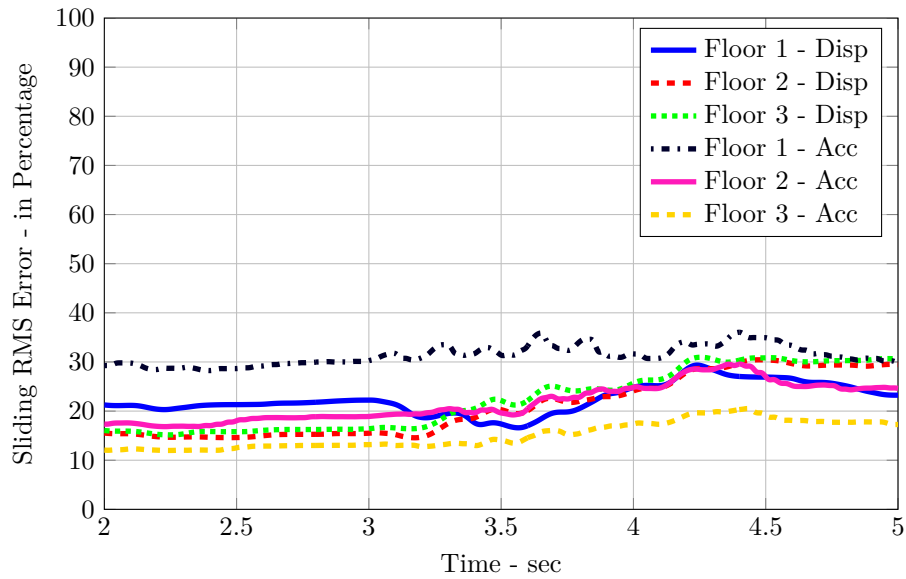


Figure 6.20: Moving RMS Error for El Centro Earthquake SA Case

Passive-on

Displacement and acceleration comparisons are given in Figs. 6.33 and 6.34. RMS and peak response errors for accelerations and displacements are ranging from 7% to 40% and are lower than pure simulation errors. The criteria-averaged error is varying from 16% to 21%.

Semi-active

SA case comparisons are presented in Figs. 6.27 and 6.28. The RMS and peak response errors are confined within 3% to 18%. The criteria-averaged errors are around 10%.

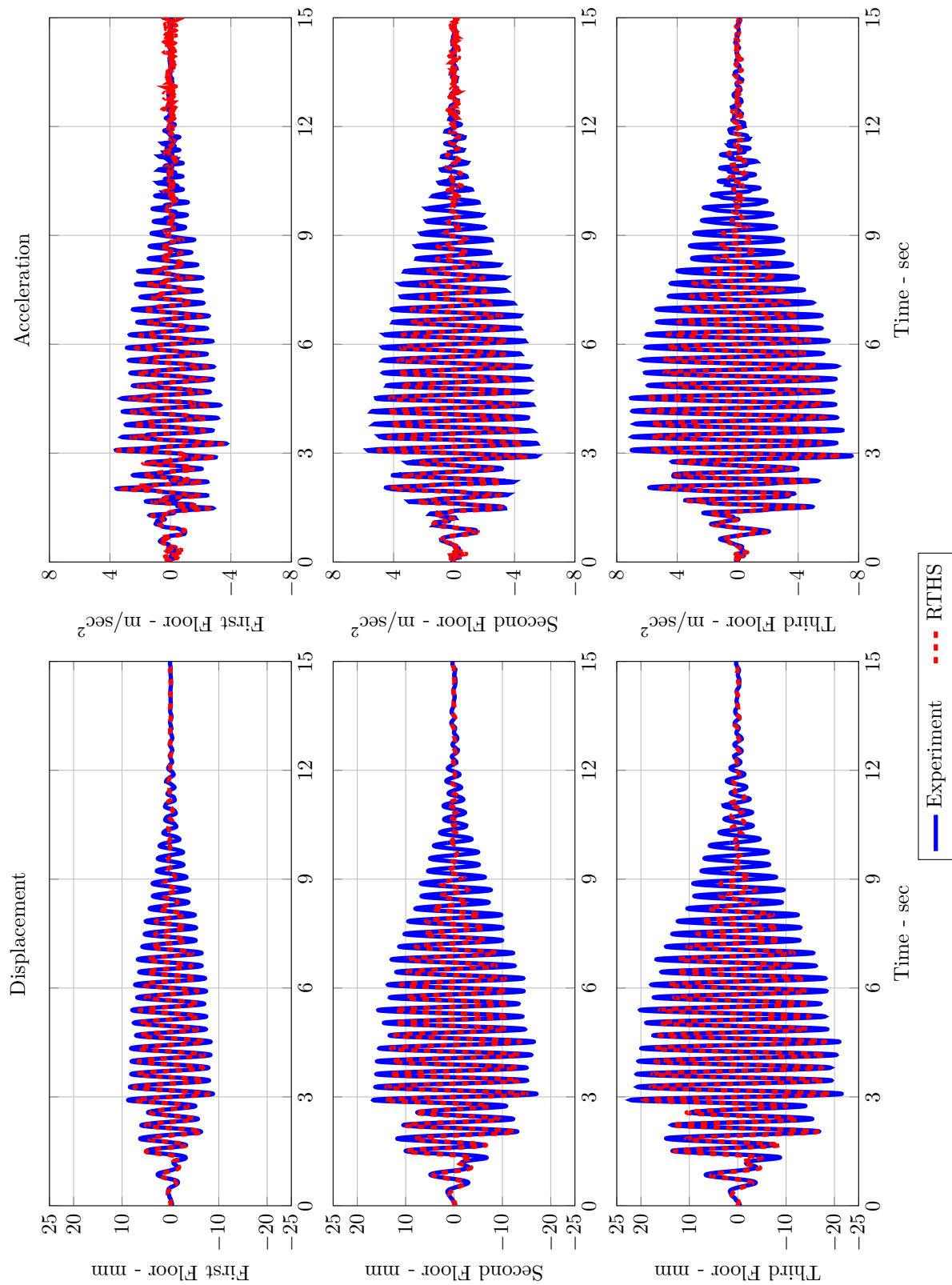


Figure 6.21: Kobe Earthquake Comparison in Time Domain for POFF Case

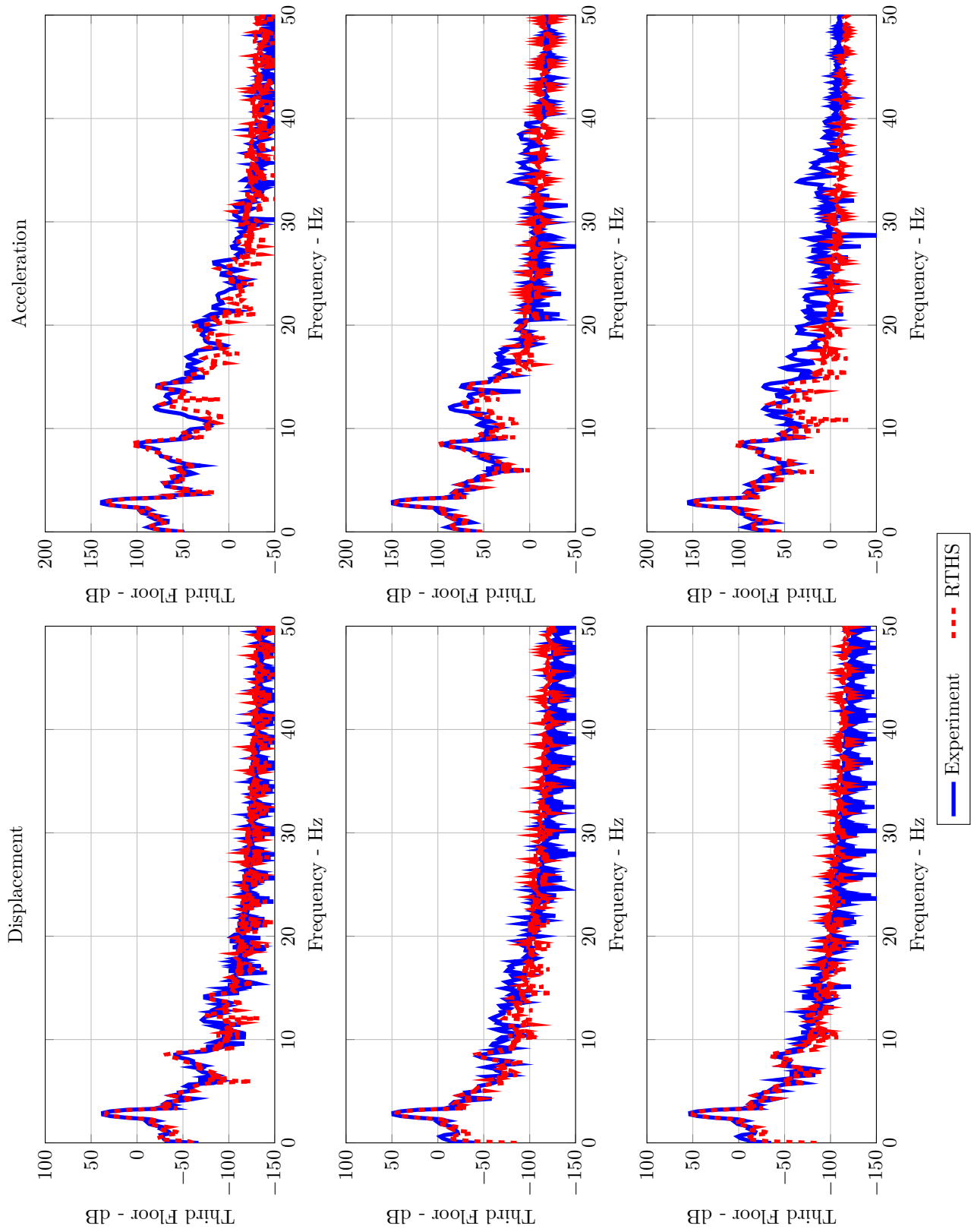


Figure 6.22: Kobe Earthquake Comparison in Frequency Domain for POFF Case

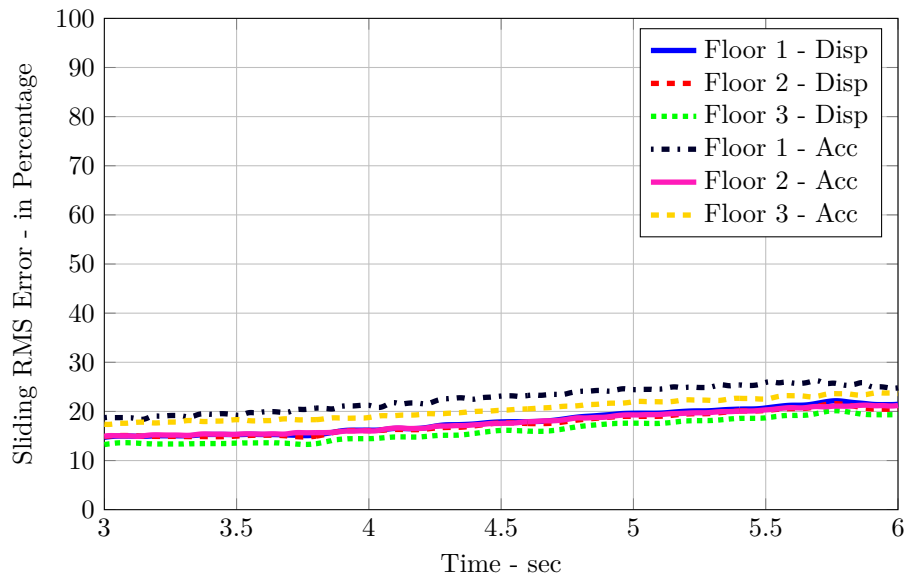


Figure 6.23: Moving RMS Error for Kobe Earthquake POFF Case

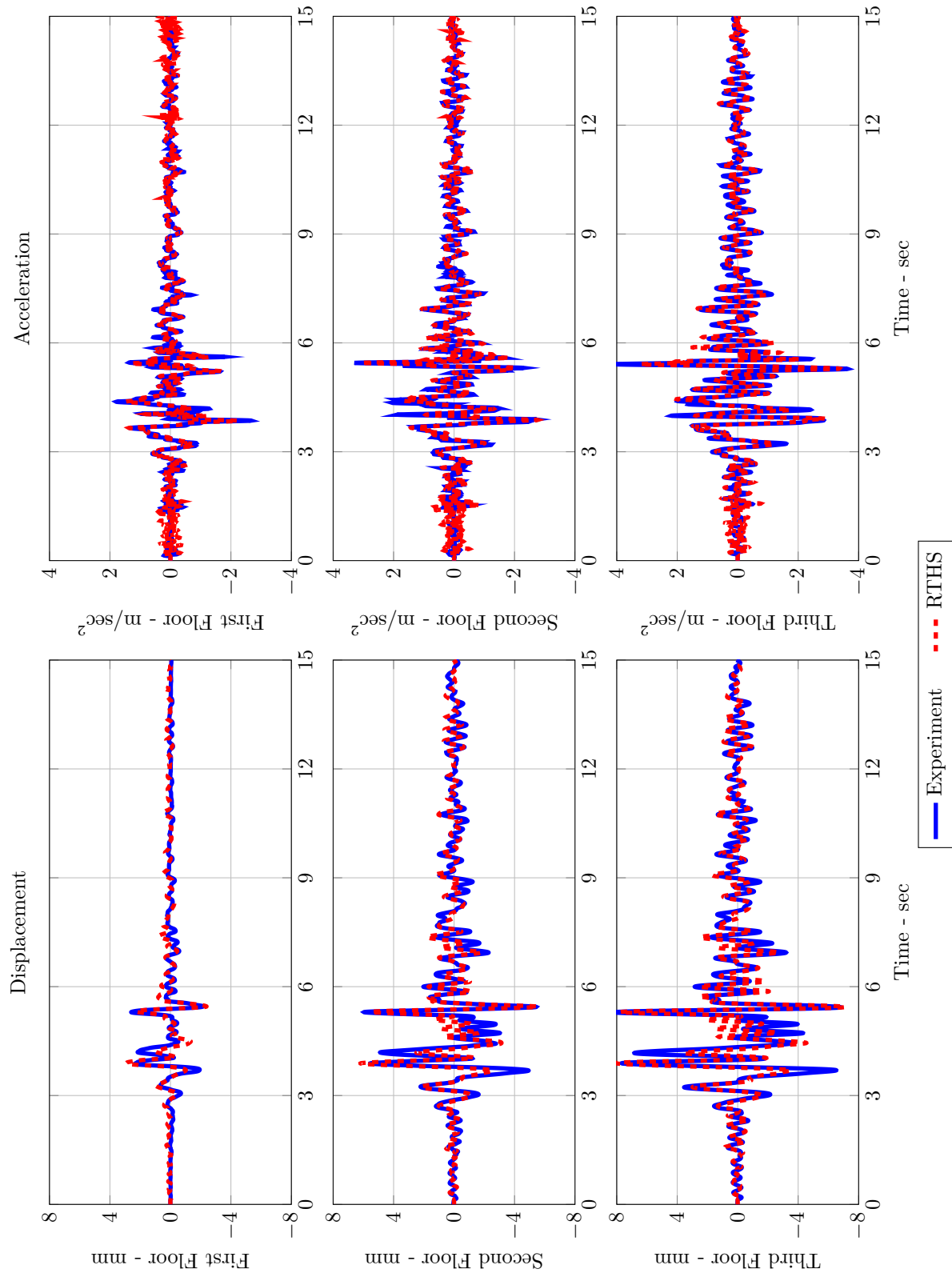


Figure 6.24: Kobe Earthquake Comparison in Time Domain for PON Case

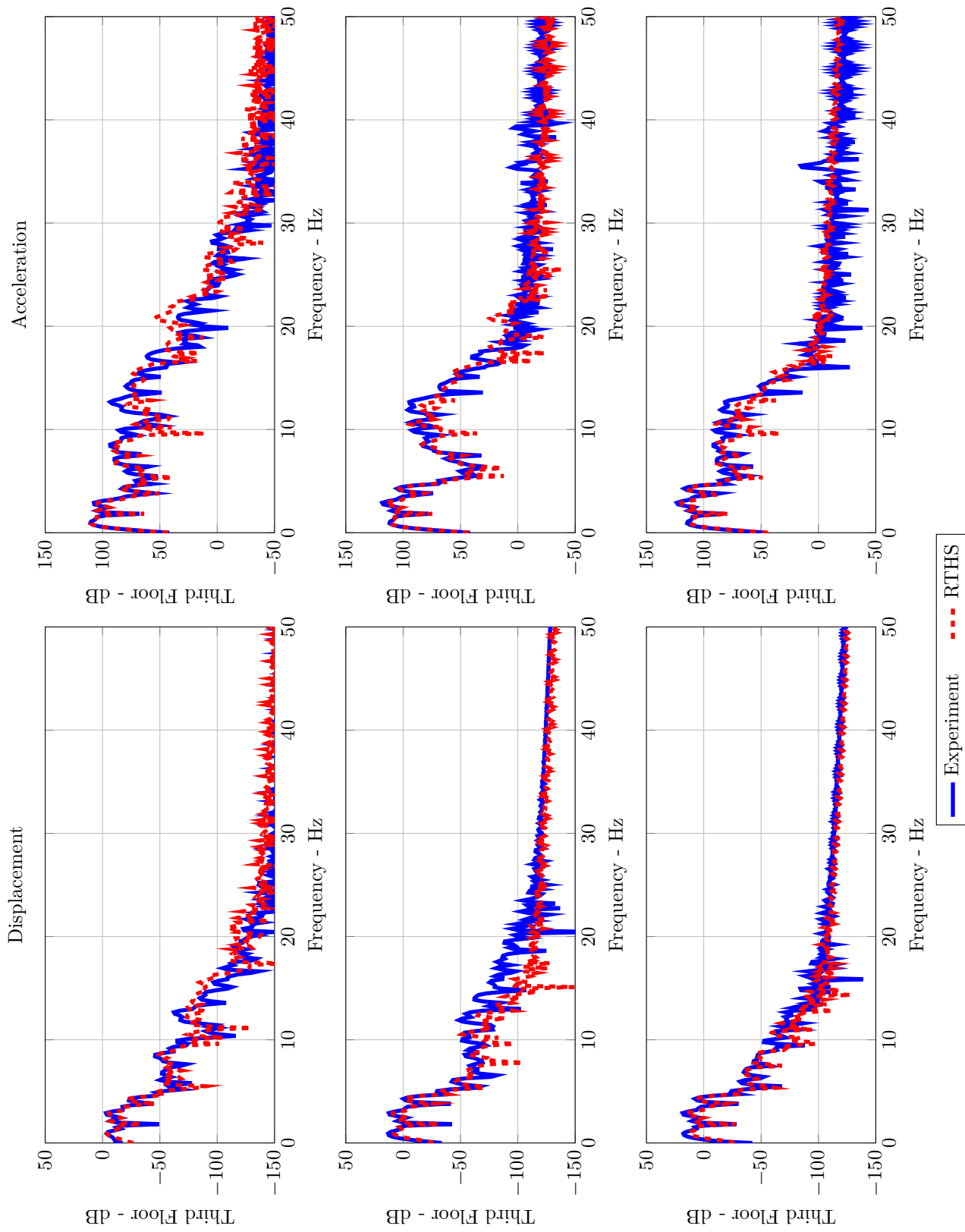


Figure 6.25: Kobe Earthquake Comparison in Frequency Domain for PON Case

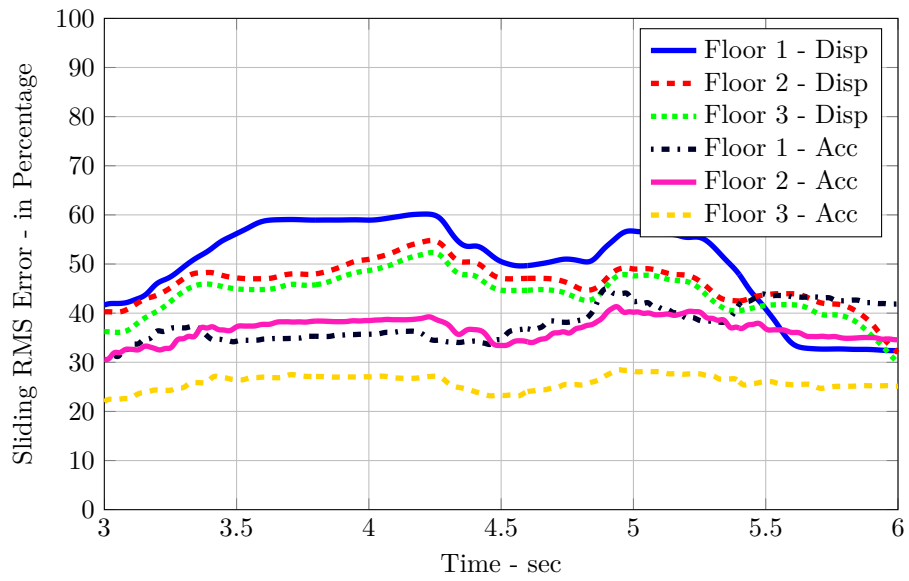


Figure 6.26: Moving RMS Error for Kobe Earthquake PON Case

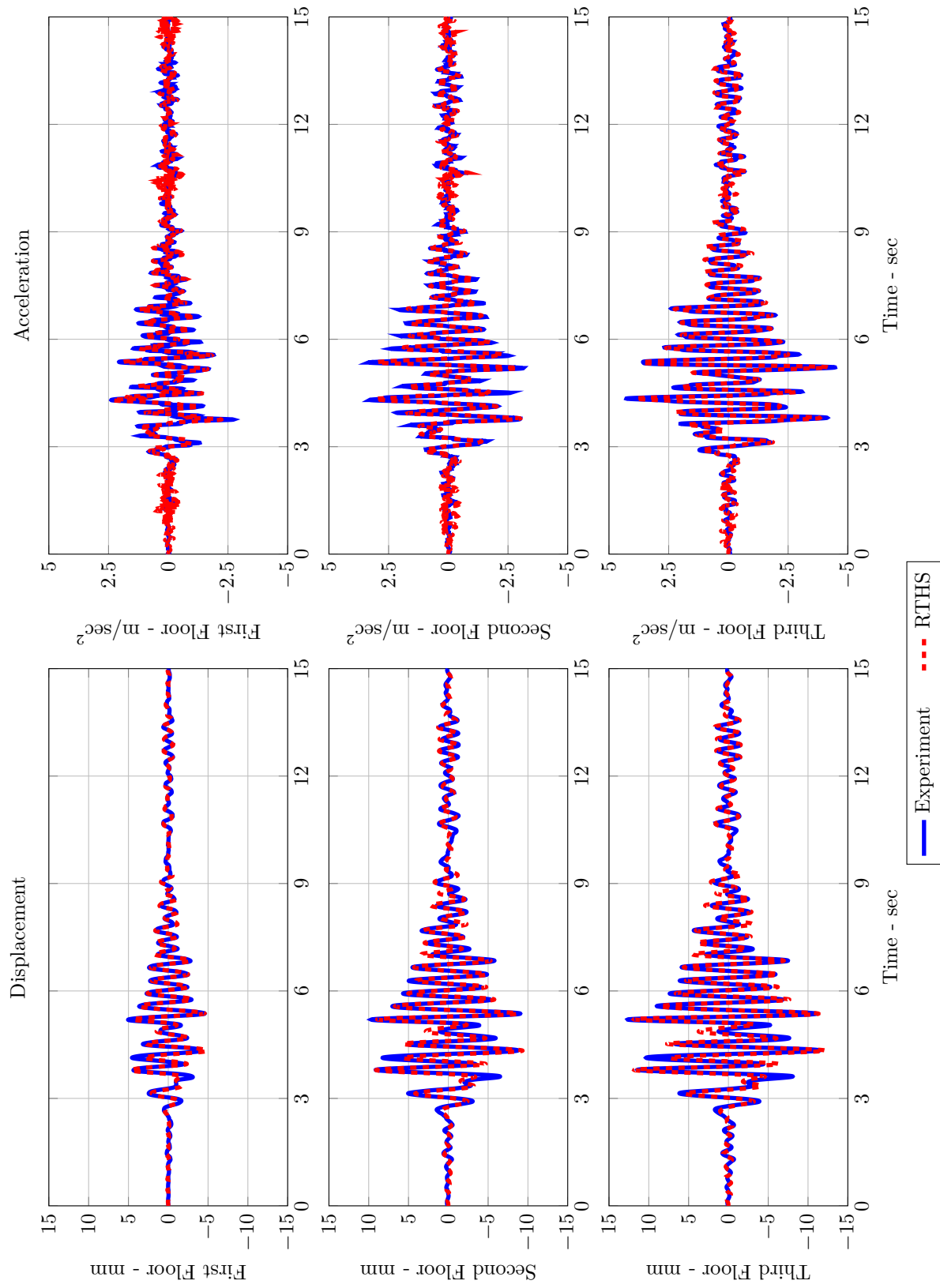


Figure 6.27: Kobe Earthquake Comparison in Time Domain for SA Case

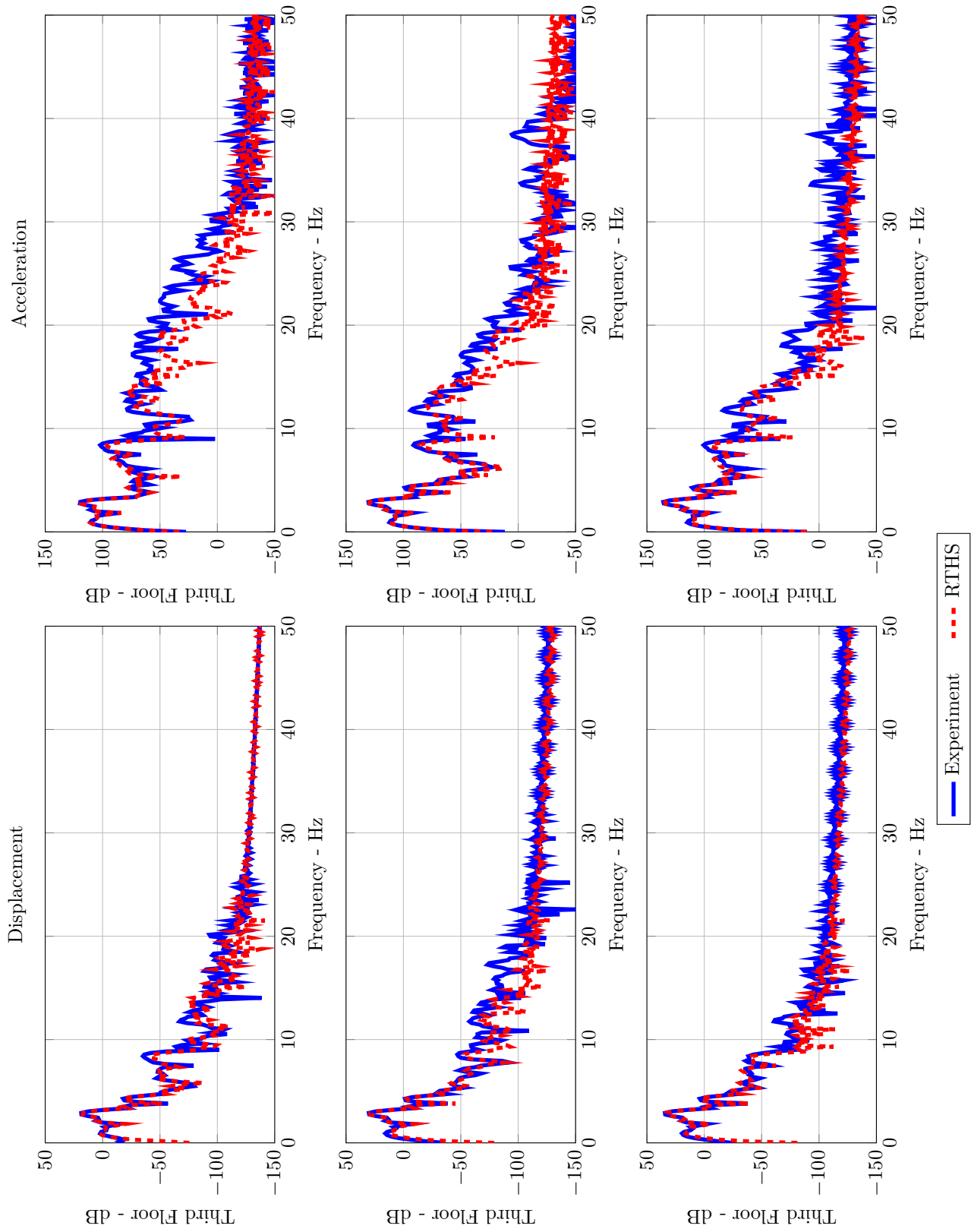


Figure 6.28: Kobe Earthquake Comparison in Frequency Domain for SA Case

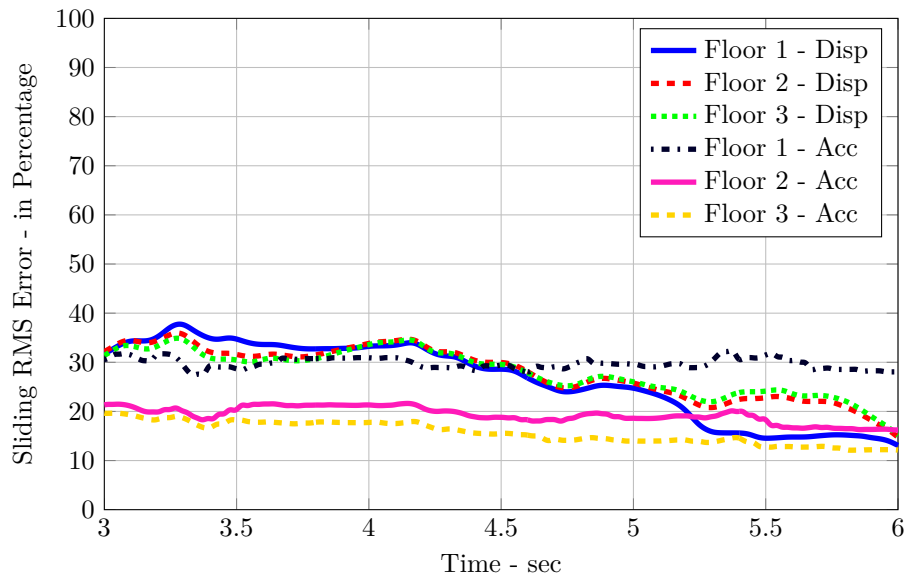


Figure 6.29: Moving RMS Error for Kobe Earthquake SA Case

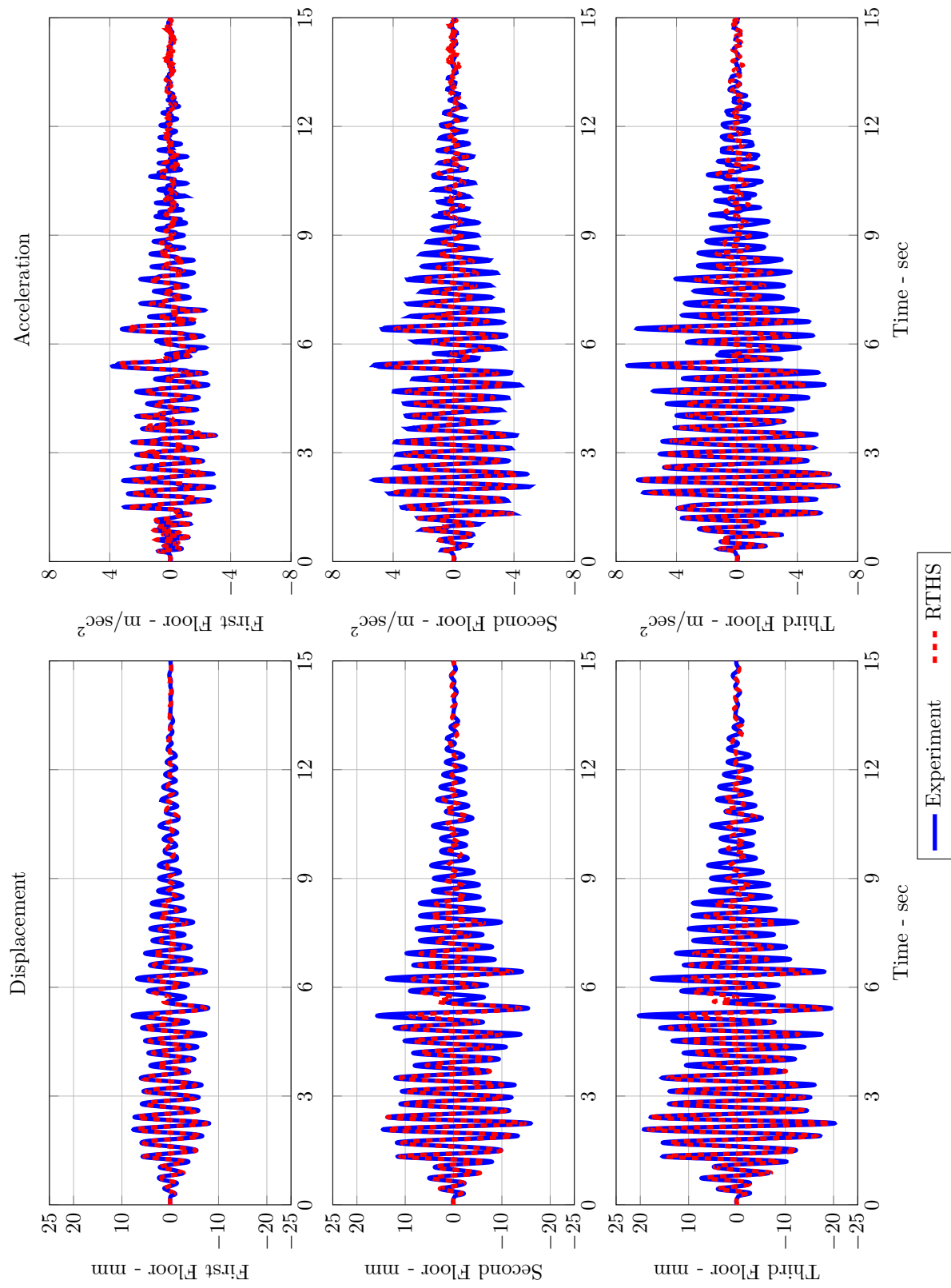


Figure 6.30: Morgan Hill Earthquake Comparison in Time Domain for POFF Case

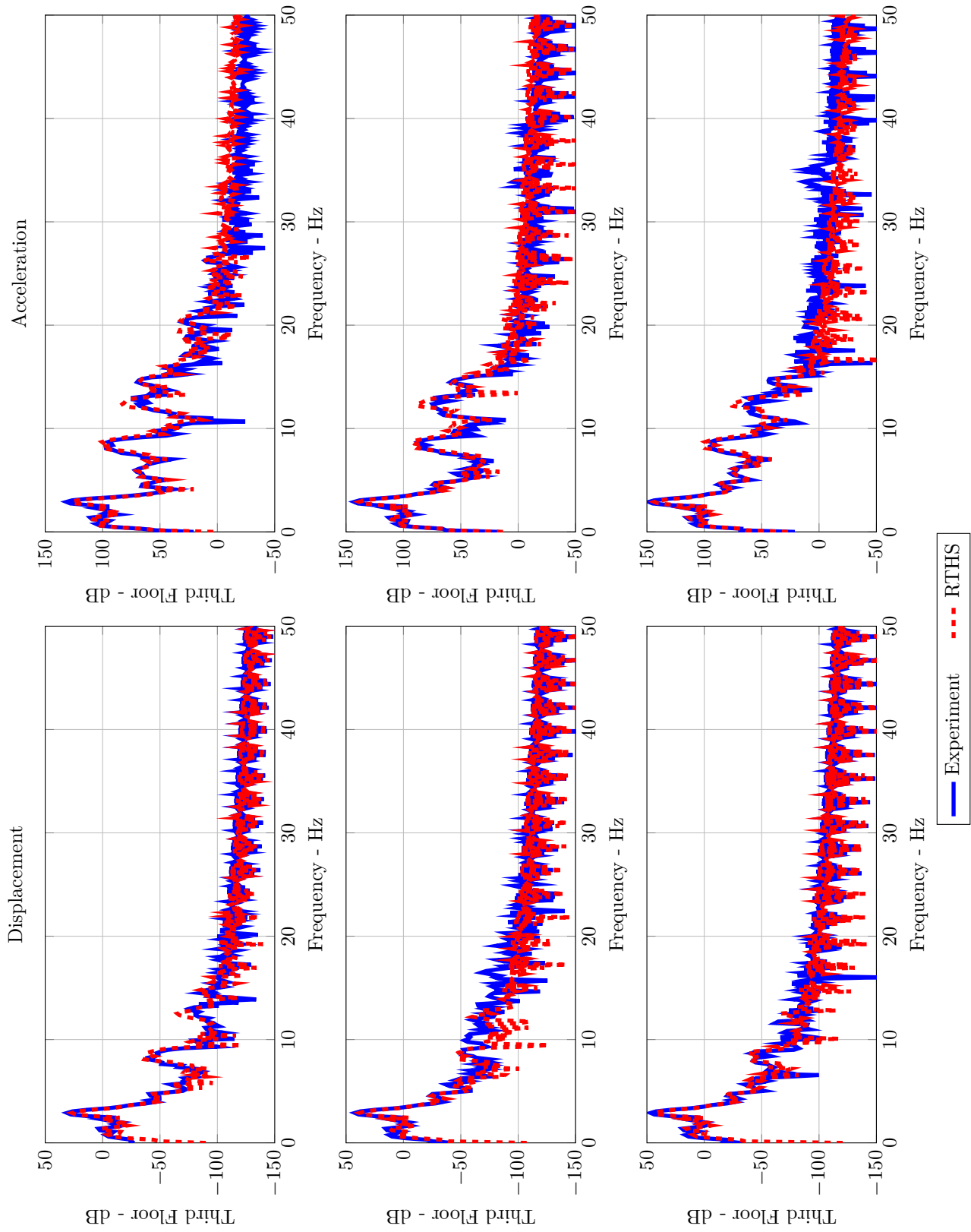


Figure 6.31: Morgan Hill Earthquake Comparison in Frequency Domain for POF Case

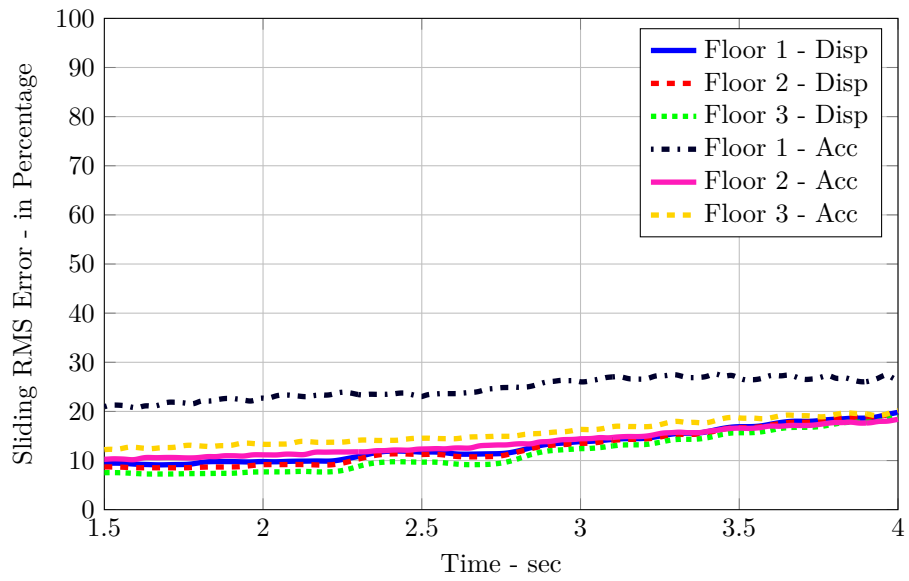


Figure 6.32: Moving RMS Error for Morgan Hill Earthquake POFF Case

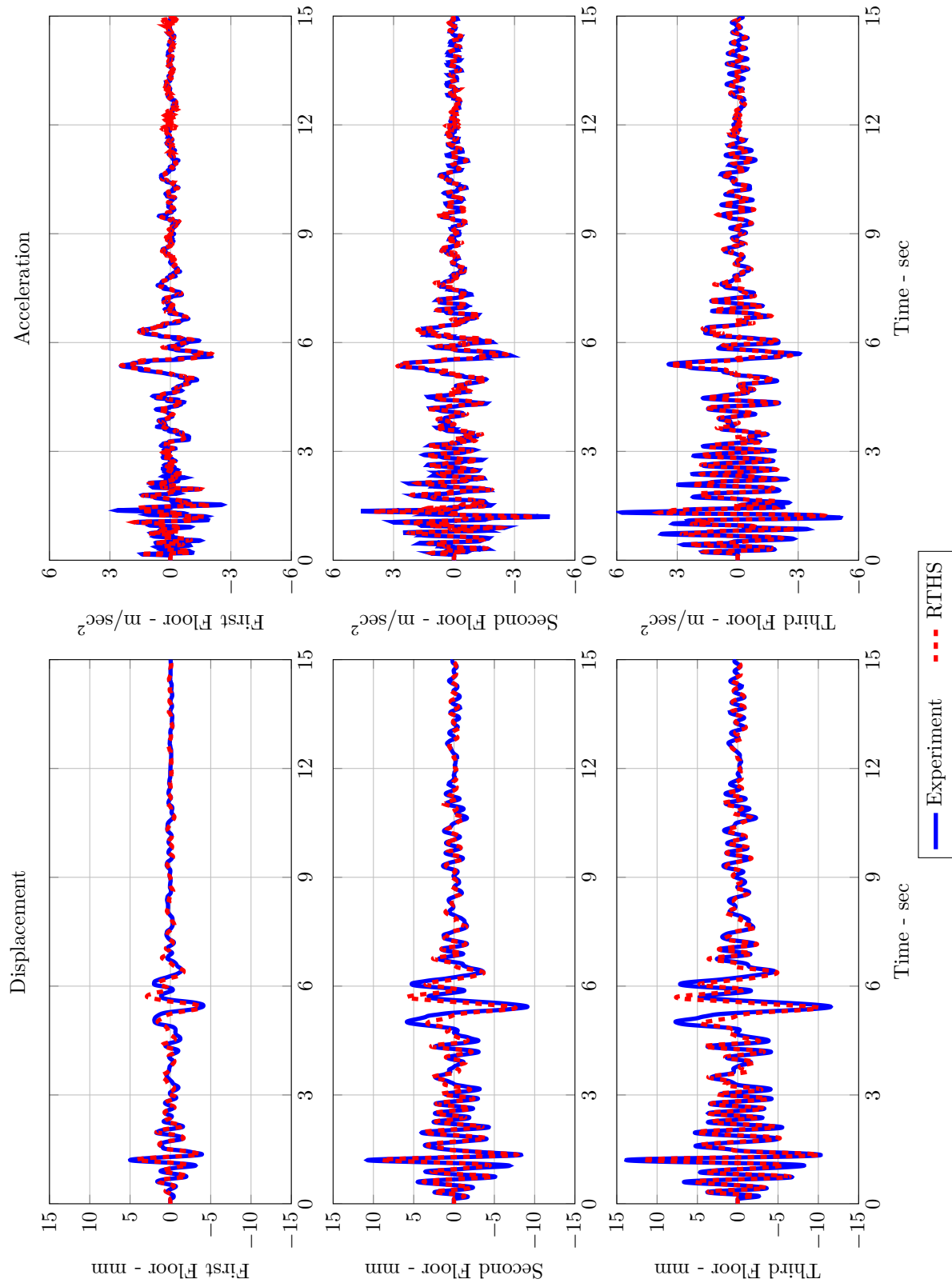


Figure 6.33: Morgan Hill Earthquake Comparison in Time Domain for PON Case

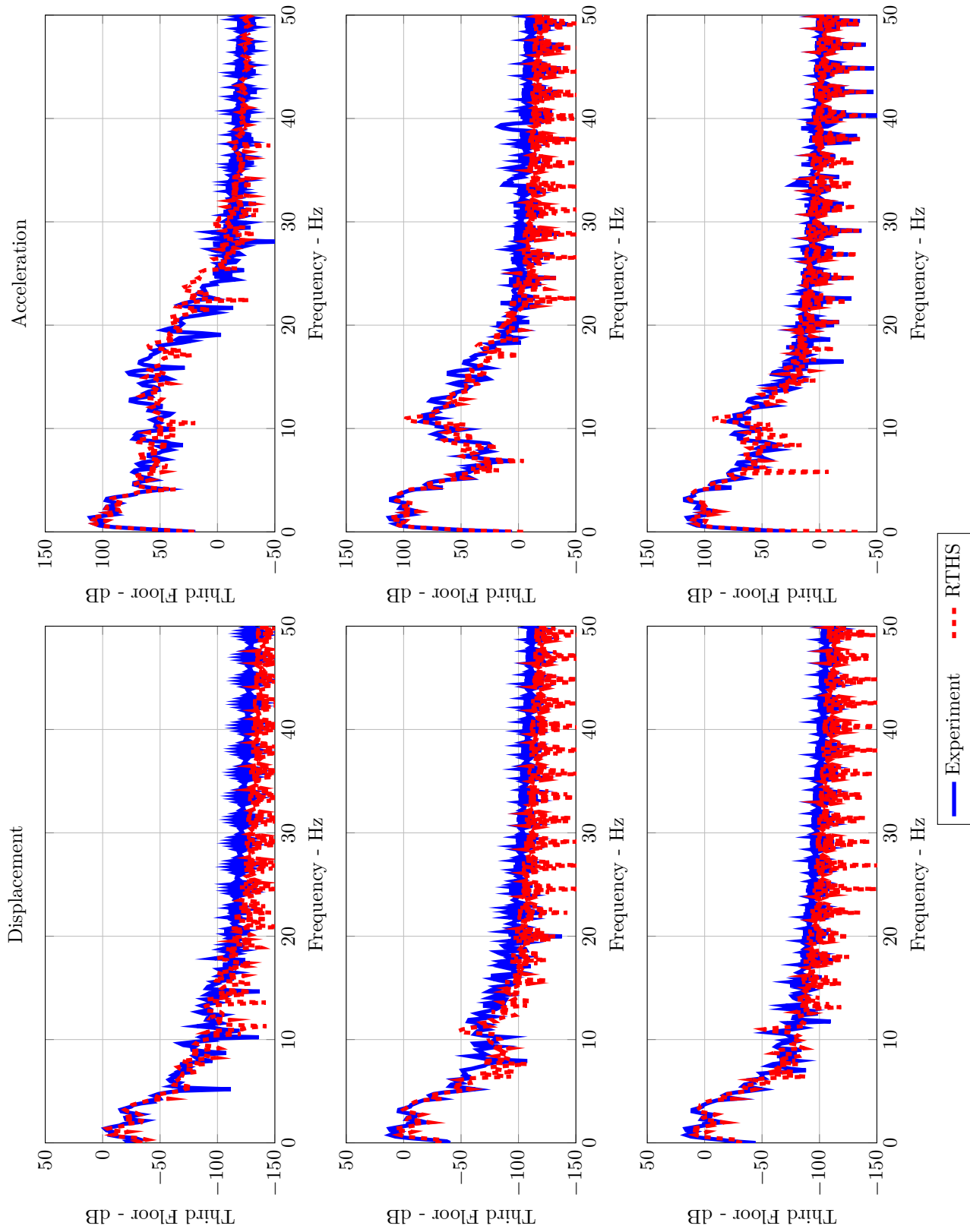


Figure 6.34: Morgan Hill Earthquake Comparison in Frequency Domain for PON Case

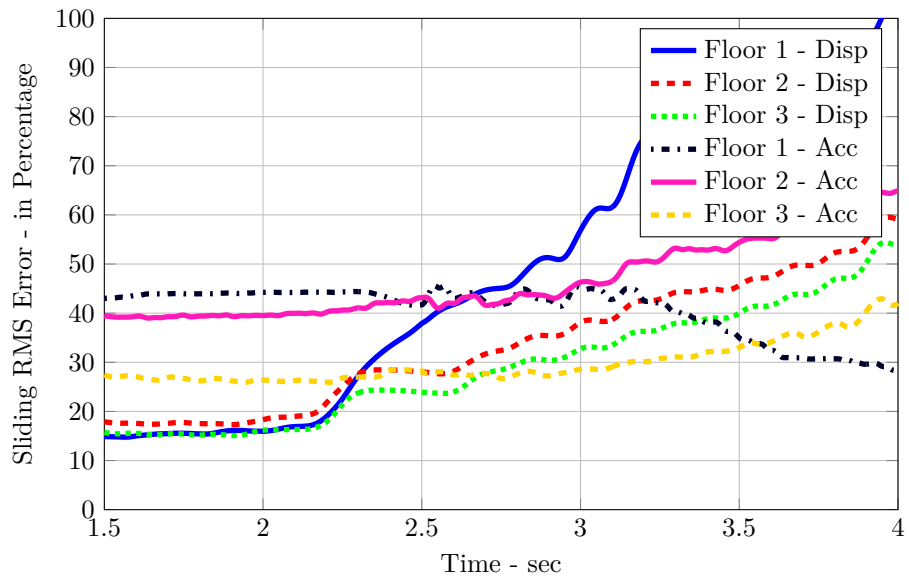


Figure 6.35: Moving RMS Error for Morgan Hill Earthquake PON Case

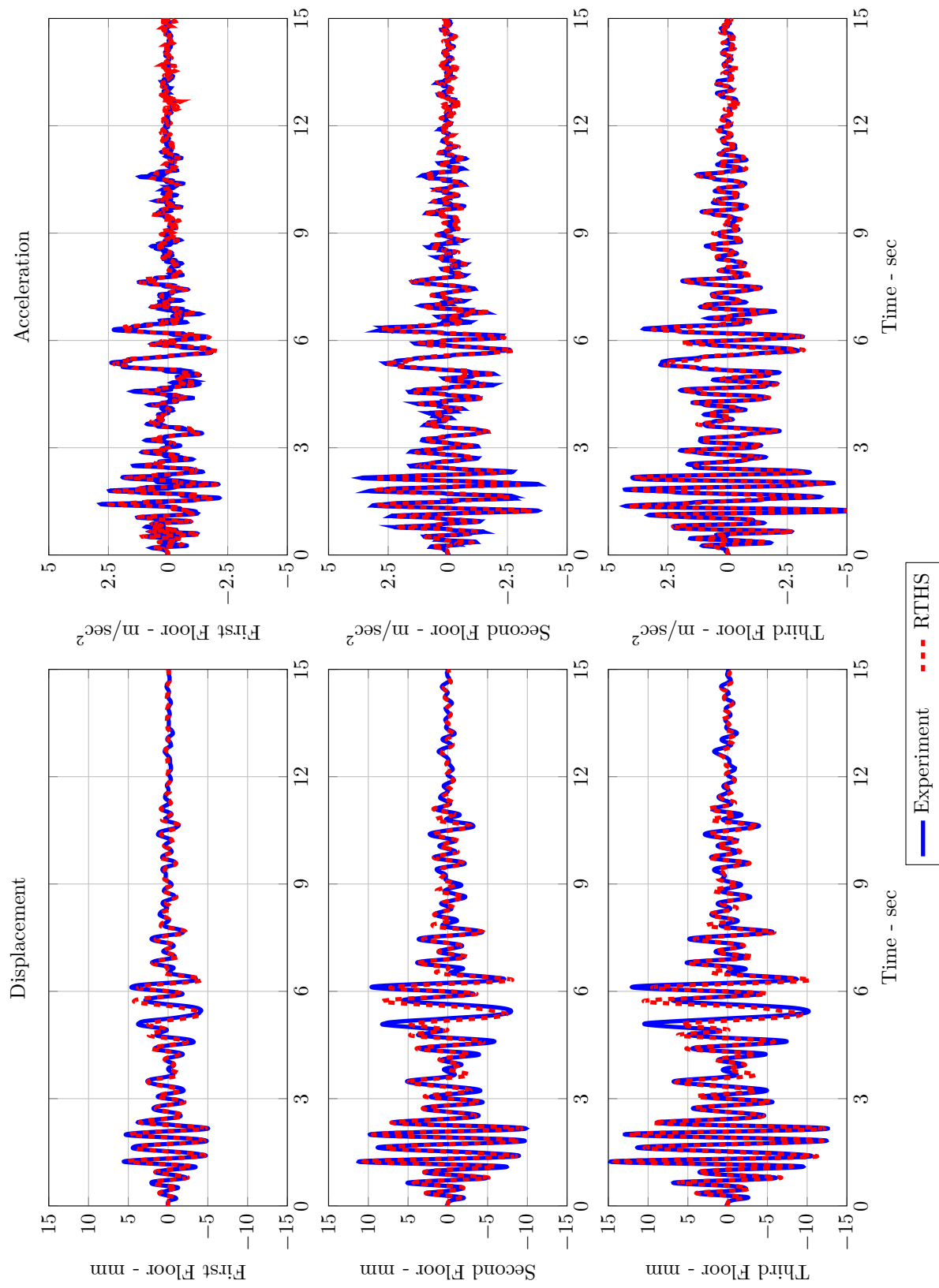


Figure 6.36: Morgan Hill Earthquake Comparison in Time Domain for SA Case

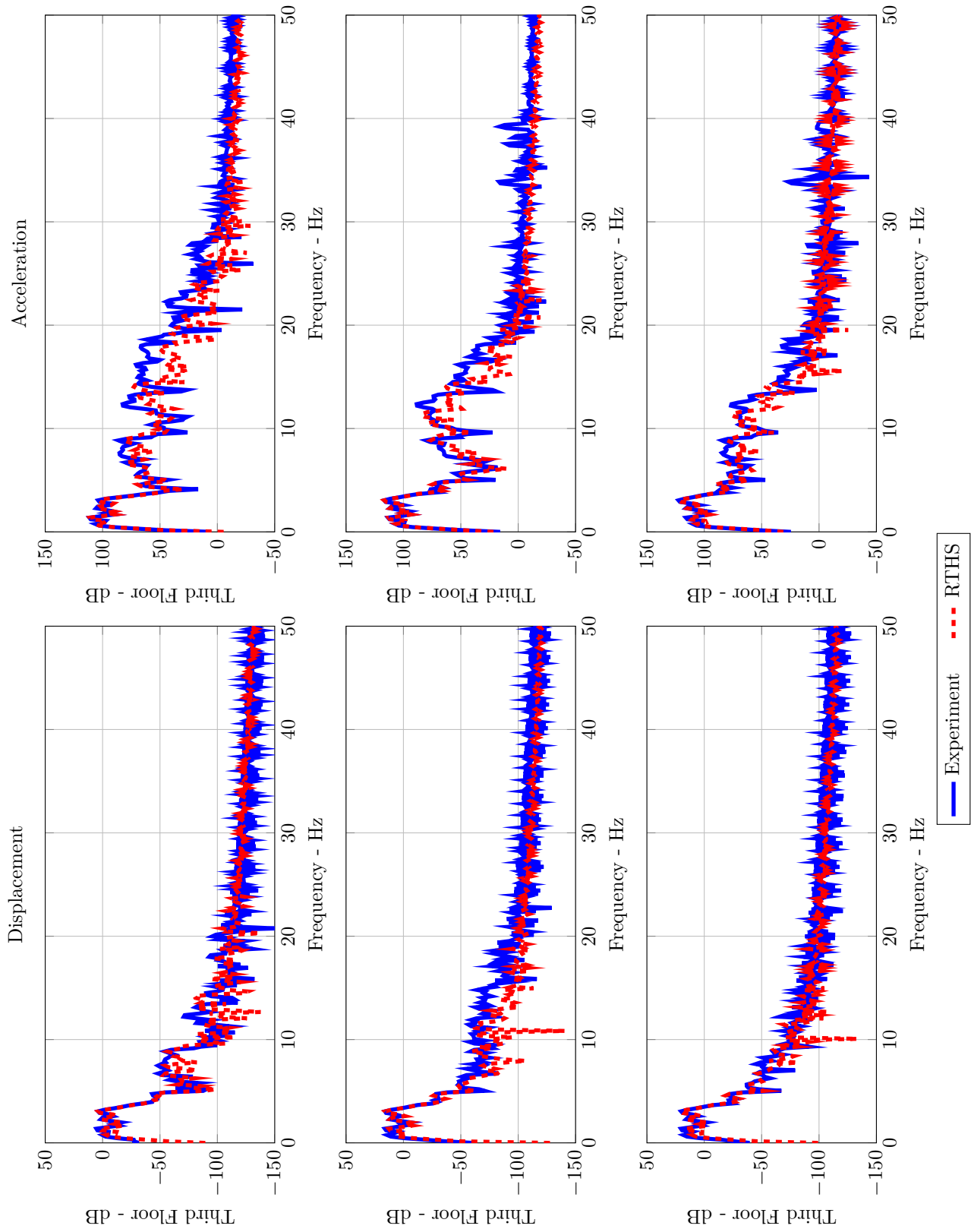


Figure 6.37: Morgan Hill Earthquake Comparison in Frequency Domain for SA Case

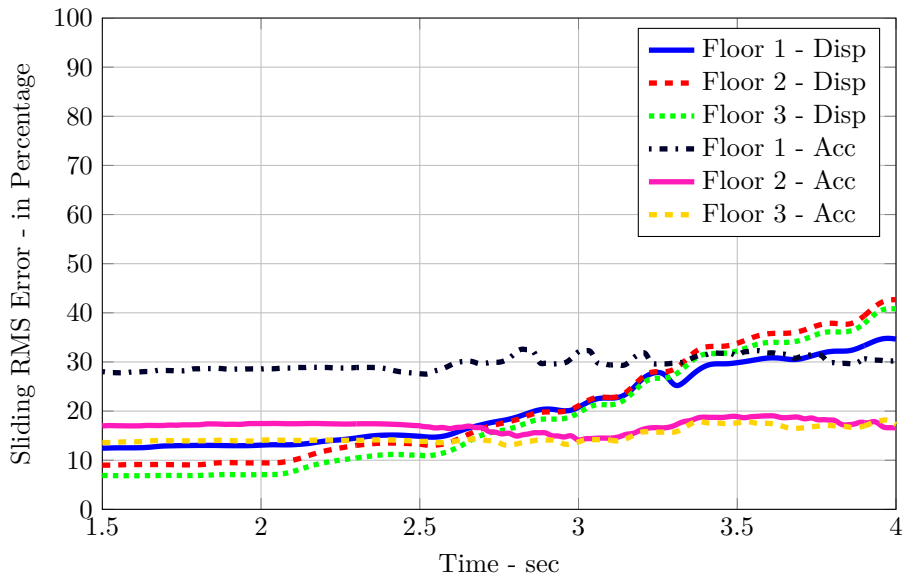


Figure 6.38: Moving RMS Error for Morgan Hill Earthquake POFF Case

6.3.4 Discussions

Considering POFF cases, El Centro for RTHS case yielded a maximum average error of 16% which is lower than the pure simulation comparison. On the other hand, RTHS errors for Kobe and Morgan Hill are around 15%, relatively and slightly larger than the pure simulation errors. The differences between force-displacement behavior of Purdue and HIT dampers at POFF mode can be accounted for the elevated errors. Despite these discrepancies, PSDs of shake table and RTHS responses demonstrate strong correlation.

RTHS and pure simulation comparisons for SA cases present similar level of averaged errors. For the PON cases, the RTHS averaged errors, particularly, errors for the first floor responses are reduced.

The overall averaged errors reported in Table 6.1 are near 18% and 20% for POFF and SA cases, respectively. The PON case averaged errors are in the

Table 6.1: Evaluation Criteria for RTHS Verification

Ground Motion	Controller	Location	Evaluation Criteria						Criteria Average
			J1	J2	J3	J4	J5	J6	
El Centro	POFF	First Floor	15.95	11.62	27.59	7.31	3.94	5.59	12.00
		Second Floor	15.56	12.34	15.43	5.78	3.75	3.57	9.41
		Third Floor	15.22	10.96	14.28	3.88	3.64	3.44	8.57
	PON	First Floor	33.78	29.50	30.60	10.37	6.60	5.26	19.35
		Second Floor	34.05	6.88	28.18	2.11	6.57	4.62	13.74
		Third Floor	33.56	8.93	23.98	21.48	6.57	4.63	16.52
	SA	First Floor	22.40	13.36	30.13	10.37	4.91	5.80	14.50
		Second Floor	18.51	7.67	19.88	17.29	3.92	3.69	11.83
		Third Floor	19.36	9.54	13.84	11.30	4.01	2.77	10.14
Kobe	POFF	First Floor	17.96	11.19	22.35	7.90	5.79	5.84	11.84
		Second Floor	17.56	13.84	17.78	16.68	5.65	5.55	12.84
		Third Floor	16.13	13.71	20.39	16.93	5.23	6.85	13.21
	PON	First Floor	51.12	12.29	37.71	16.02	10.85	6.01	22.33
		Second Floor	45.81	4.19	37.06	6.93	9.76	6.23	18.33
		Third Floor	43.59	4.04	26.26	20.95	9.57	4.54	18.16
	SA	First Floor	26.68	7.38	29.93	17.59	6.63	5.67	15.65
		Second Floor	27.59	6.32	19.34	9.01	6.86	4.37	12.25
		Third Floor	27.45	6.23	15.54	8.87	6.69	3.47	11.37
Morgan	POFF	First Floor	13.53	9.01	23.89	9.81	3.78	6.15	11.03
		Second Floor	13.19	7.83	13.72	14.06	3.65	3.67	9.35
		Third Floor	12.14	5.28	15.69	4.23	3.33	4.36	7.50
	PON	First Floor	41.45	5.56	41.03	23.84	8.68	5.79	21.06
		Second Floor	30.65	7.56	45.25	7.61	7.16	9.94	18.03
		Third Floor	27.26	5.56	29.73	24.13	6.77	6.83	16.72
	SA	First Floor	17.25	9.89	28.86	9.31	3.76	5.61	12.45
		Second Floor	17.13	5.89	17.36	21.10	3.82	3.35	11.44
		Third Floor	15.64	4.23	14.44	8.42	3.39	3.14	8.21
EQ Average	POFF	First Floor	15.81	10.61	24.61	8.34	4.51	5.86	11.62
		Second Floor	15.44	11.34	15.64	12.17	4.35	4.26	10.53
		Third Floor	14.49	9.98	16.79	8.35	4.07	4.88	9.76
	PON	First Floor	42.12	15.78	36.45	16.74	8.71	5.68	20.91
		Second Floor	36.84	6.21	36.83	5.55	7.83	6.93	16.70
		Third Floor	34.81	6.18	26.66	22.19	7.64	5.33	17.13
	SA	First Floor	22.11	10.21	29.64	12.42	5.10	5.70	14.20
		Second Floor	21.08	6.63	18.86	15.80	4.87	3.80	11.84
		Third Floor	20.82	6.67	14.60	9.53	4.70	3.13	9.91

range of 24 % to 36 %.

6.4 Conclusions

In this chapter, shake table responses of MR damper controlled three story structure located at HIT are compared to RTHS responses. In RTHS configuration, the system is partitioned into physical substructure represented by the Purdue MR damper, and analytical substructure simulated by the model of the test structure.

For the RTHS configuration, ground motions recorded by the accelerometers are used as the excitation input, while MR damper is driven in POFF, PON, and SA mode. Resulting relative displacements and absolute accelerations of each floor are compared to shake table responses. To assess the performance and validate feasibility of RTHS, peak, RMS, and sliding RMS errors are computed. PSDs of the shake table and RTHS responses are also supplemented to show the RTHS efficiency in frequency domain.

In summary, RTHS was able to predict shake table test responses successfully. The results of evaluation criteria also validated that RTHS can be a valid alternative to shake table tests.

CHAPTER 7

CONCLUSIONS

This report presents results of a series of studies to explore validation of Real-time Hybrid Simulation conducted at Purdue University with shake table responses of an actual full-scale three story structure, equipped with MR damper, tested at Harbin Institute of Technology. RTHS configuration is partitioned into (i) numerical substructure represented by the analytical model of the test structure and (ii) physical substructure, a current controllable vibration control device, MR damper. Three historical earthquake ground motions, El Centro, Kobe and Morgan Hill are used as the excitation input while MR damper located between the first floor and the ground is controlled at passive-off, passive-on and semi-active mode. At least, the results of RTHS are compared to shake table responses.

To deliver the information in the most convenient way, first, a literature review emphasizing previous work on the validation RTHS is given. The shortcomings of the previous studies were explored to build up and deliver a concrete motivation for this study.

Second, an extensive review of the experimental setup, including test struc-

ture, equipment, sensors and software for shake table tests is presented. Furthermore, the hardware to perform RTHS, including inner and outer loop controllers and servo-hydraulic systems are also discussed.

Next, a novel modeling and system updating technique based on system identification results of Eigensystem Realization Algorithm is introduced. This modeling method is focused on eliminating the drawbacks of its predecessors. Using this proposed tool, a *MCK* matrix of the test structure is derived. Later, the performance of this model is validated using shake table responses. This analytical model is also used as the basis of the numerical substructure of the RTHS.

Since the damper used at HIT is different than the one of RTHS at Purdue, a characterization of the dampers are required. By comparing force-displacement and force-velocity curves of those two dampers, equivalent voltage levels for the Purdue damper is determined to imitate necessary HIT damper force at passive-off and -on mode. In addition, an analytical model of the HIT damper based on Bouc-Wen hysteresis model is utilized. This model is also used in the pure simulation - shake table comparisons which will be discussed next.

To develop a baseline for RTHS - shake table comparisons and understand main sources of error that may manifest during RTHS, an integrated simulation including analytical models of the test structure and MR damper is conducted. The pure simulations predicted the global responses of the shake table tests accurately. The source of errors are explored and the possible reasons are described.

Before the RTHS - shake table comparisons, first, a state-of-art controller, Robust Integrated Actuator Control to compensate actuator dynamics is introduced. Essentially, RIAC is a model based H_∞ type controller that integrates a loop-shaping filter to handle delay and magnitude dynamics of the actuator and

a Kalman filter to reject the noise in the measurements. To study the impact of the size and speed of the actuator on the tracking performance, the controller is verified by comparing desired and measured displacement of the actuator through band-limited white noises at HIT's large and Purdue's small actuators. After the controller validation, RTHS is employed at Purdue and the results of RTHS is compared to shake table responses. It has been found that the errors produced by RTHS are marginally lower than those of pure simulations. This observation leads to the conclusion that RTHS can be considered as a viable option to pure simulations, as well as, shake table tests for this particular test structure.

Bibliography

- A. E. Aktan and F. L. Moon. *ASCE-SEI performance of structures track technical committee: Structural identification of constructed Systems*. Drexel University, Philadelphia, PA, 2005.
- ASCE. *Seismic Rehabilitation of Existing Buildings*. American Society of Civil Engineers, Reston, VA, asce/sei 41-06 edition, 2007. doi: 10.1061/9780784408841. URL <http://ascelibrary.org/doi/abs/10.1061/9780784408841>.
- A. Ashasi-Sorkhabi, H. Malekghasemi, and O. Mercan. Implementation and verification of real-time hybrid simulation (RTHS) using a shake table for research and education. *Journal of Vibration and Control*, 2013. doi: 10.1177/1077546313498616. URL <http://jvc.sagepub.com/content/early/2013/08/08/1077546313498616.abstract>.
- R. Bouc. Mathematical model of hysteresis: Application to systems with a degree of freedom. *Acustica*, 24:16–25, 1971.
- J. M. Caicedo. Practical guidelines for the natural excitation technique (NExT) and the eigensystem realization algorithm (ERA) for modal identification using ambient vibration. *Experimental Techniques*, 35(4):52–58, 2011. ISSN

- 1747-1567. doi: 10.1111/j.1747-1567.2010.00643.x. URL <http://dx.doi.org/10.1111/j.1747-1567.2010.00643.x>.
- J. M. Caicedo, S. J. Dyke, and E. A. Johnson. Natural excitation technique and eigensystem realization algorithm for phase i of the iasc-asce benchmark problem: Simulated data. *Journal of Engineering Mechanics*, 130(1):49–60, 2004. doi: 10.1061/(ASCE)0733-9399(2004)130:1(49). URL <http://ascelibrary.org/doi/abs/10.1061/%28ASCE%290733-9399%282004%29130%3A1%2849%29>.
- J. D. Carlson and B. F. Spencer. Magneto-rheological fluid dampers for semi-active seismic control. In *Proc. of the 3rd Int. Conf. on Motion and Vibr. Control*, volume II, pages 35–40, 1996.
- J. D. Carlson, D. M. Catanzarite, and K. A. S. Clair. Commercial magnetorheological fluid devices. *INTERNATIONAL JOURNAL OF MODERN PHYSICS B*, 10:2857–2866, 1996. ISSN 0217-9792. 23/24.
- J. E. Carrion, B. F. Spencer, and B. M. Phillips. Real-time hybrid testing of a semi-actively controlled structure with an MR damper. In *American Control Conference, 2009. ACC'09.*, pages 5234–5240, 2009. ISBN 0743-1619.
- N. Castaneda, X. Gao, and S. J. Dyke. A computational tool for real-time hybrid simulation of seismically-excited steel frame structures. *Journal of Computing in Civil Engineering*, 2013. doi: 10.1061/(ASCE)CP.1943-5487.0000341. URL <http://ascelibrary.org/doi/abs/10.1061/%28ASCE%29CP.1943-5487.0000341>.
- F. N. Catbas, T. L. Kijewski-Correa, and A. E. Structural Engineering Institute Committee on Structural Identification of Constructed Systems Aktan. *Structural identification of constructed systems : approaches, methods, and technologies for effective practice of St-Id*. ASCE Publications, 2013.

- C. Chang, Z. Wang, and B. F. Spencer. Application of active base isolation control. In *SPIE Smart Structures and Materials Nondestructive Evaluation and Health Monitoring*, pages 729239–729239. International Society for Optics and Photonics, 2009.
- C. Chen and J. M. Ricles. Analysis of actuator delay compensation methods for real-time testing. *Engineering Structures*, 31(11):2643–2655, 2009.
- C. Chen, J. M. Ricles, T. M. Marullo, and O. Mercan. Real-time hybrid testing using the unconditionally stable explicit CR integration algorithm. *Earthquake Engineering & Structural Dynamics*, 38(1):23–44, 2009. ISSN 1096-9845. doi: 10.1002/eqe.838. URL <http://dx.doi.org/10.1002/eqe.838>.
- Z. Q. Chen, X. Y. Wang, J. M. Ko, Y. Q. Ni, B. F. Spencer, and G. Yang. Mr damping system on dongting lake cable-stayed bridge. In *Smart Structures and Materials*, pages 229–235. International Society for Optics and Photonics, 2003.
- A. K. Chopra. *Dynamics of structures*, volume 3. Prentice Hall New Jersey, 1995.
- R. E. Christenson, Y. Z. Lin, A. Emmons, and B. Bass. Large-scale experimental verification of semiaactive control through real-time hybrid simulation. *Journal of Structural Engineering*, 134:522–534, 2008. URL <http://link.aip.org/link/?QST/134/522/1>[http://dx.doi.org/10.1061/\(ASCE\)0733-9445\(2008\)134:4\(522\)](http://dx.doi.org/10.1061/(ASCE)0733-9445(2008)134:4(522)).
- M. C. Constantinou, Tsu T. Soong, and G. F. Dargush. *Passive energy dissipation systems for structural design and retrofit*. Multidisciplinary Center for Earthquake Engineering Research Buffalo, NY, 1998.

- R. R. Craig and A. J. Kurdila. *Fundamentals of structural dynamics*. John Wiley & Sons, 2006.
- G. G. Deierlein, A. M. Reinhorn, and M. R. Willford. Nonlinear structural analysis for seismic design. *NEHRP Seismic Design Technical Brief No, 4*, 2010.
- S. J. Dyke. *Acceleration feedback control strategies for active and semi-active control systems : modeling, algorithm development, and experimental verification*. PhD thesis, University of Notre Dame, 1996.
- S. J. Dyke, B. F. Spencer, M. K. Sain, and J. D. Carlson. Experimental verification of semi-active structural control strategies using acceleration feedback. In *Proc. 3rd Int. Conf. on Motion and Vibration Control*, Chiba, Japan, 1996a.
- S. J. Dyke, B. F. Spencer, M. K. Sain, and J. D. Carlson. Modeling and control of magnetorheological dampers for seismic response reduction. *Smart Materials and Structures*, 5:565, 1996b. ISSN 0964-1726. URL <http://stacks.iop.org/0964-1726/5/i=5/a=006>. 5.
- S. J. Dyke, B. Stojadinovic, P. Arduino, M. Garlock, N. Luco, J. A. A. Ramirez, and S. Yim. 2020 vision for earthquake engineering research. June 2010. URL http://nees.org/resources/1637/download/Vision_2020__Final_Report.pdf.
- B. Erkus and E. A. Johnson. Smart base-isolated benchmark building part III: a sample controller for bilinear isolation. *Structural Control and Health Monitoring*, 13:605–625, 2006. ISSN 1545-2263. doi: 10.1002/stc.101. URL <http://dx.doi.org/10.1002/stc.101>. 2-3.
- A. J. Friedman. *Development and experimental validation of a new control strategy considering device dynamics for large-scale MR dampers using real-*

- time hybrid simulation*. PhD thesis, Purdue University, West Lafayette, IN, 2012.
- A. J. Friedman, J. Zhang, B. M. Phillips, Z Jiang, A. Agrawal, S J Dyke, J. M. Ricles, B. F. Spencer, Richard Sause, and R. E. Christenson. Accommodating MR damper dynamics for control of large scale structural systems. In *Proceedings of the Fifth World Conference on Structural Control and Monitoring*, volume 5WCSCM- 10075, 2010.
- X. Gao, N. Castaneda, and S. J. Dyke. Real time hybrid simulation: from dynamic system, motion control to experimental error. *Earthquake Engineering & Structural Dynamics*, 42(6):815–832, 2013a.
- X. Gao, N. Castaneda, and S. J. Dyke. Experimental validation of a generalized procedure for mdof real-time hybrid simulation. *Journal of Engineering Mechanics*, 0(ja):null, 2013b. doi: 10.1061/(ASCE)EM.1943-7889.0000696. URL <http://ascelibrary.org/doi/abs/10.1061/%28ASCE%29EM.1943-7889.0000696>.
- Wassim M Ghannoum and Jack P Moehle. Shake-table tests of a concrete frame sustaining column axial failures. *ACI Structural Journal*, 109(3), 2012.
- D. Giraldo, O. Yoshida, S. J. Dyke, and L. Giacosa. Control-oriented system identification using ERA. *Structural Control and Health Monitoring*, 11:311–326, 2004. ISSN 1545-2263. doi: 10.1002/stc.46. URL <http://dx.doi.org/10.1002/stc.46>. 4.
- W. G. Halvorsen and D. L. Brown. Impulse technique for structural frequency response testing. *Journal of Basic Engineering*, 11(11):8–21, 1977.
- G. W. Housner, L. A. Bergman, T. K. Caughey, A. G. Chassiakos, R. O. Claus, S. F. Masri, R. E. Skelton, T. T. Soong, B. F. Spencer, and J. T. P.

- Yao. Structural control: Past, present, and future. *Journal of Engineering Mechanics*, 123:897–971, 1997. URL [http://dx.doi.org/10.1061/\(ASCE\)0733-9399\(1997\)123:9\(897\)](http://dx.doi.org/10.1061/(ASCE)0733-9399(1997)123:9(897)). 9.
- Z. Jiang and R. E. Christenson. A comparison of 200 kN magneto-rheological damper models for use in real-time hybrid simulation pretesting. *Smart Materials and Structures*, 20:065011, 2011. ISSN 0964-1726. URL <http://stacks.iop.org/0964-1726/20/i=6/a=065011>. 6.
- E. A. Johnson, J. C. Ramallo, B. F. Spencer, and M. K. Sain. Intelligent base isolation systems. In *Proceedings of the Second World Conference on Structural Control*, volume 1, pages 367–76, June 1998.
- J. N. Juang and R. S. Pappa. An eigensystem realization algorithm for modal parameter identification and model reduction. *Journal of Guidance, Control, and Dynamics*, 8(5):620–627, 1985a.
- J. N. Juang and R. S. Pappa. An eigensystem realization-algorithm for modal parameter-identification and model-reduction. *Journal of Guidance Control and Dynamics*, 8:620–627, 1985b. ISSN 0731-5090. doi: 10.2514/3.20031. URL <://WOS:A1985APZ0400012>. 5.
- R. E. Kalman. A new approach to linear filtering and prediction problems. *Journal of Basic Engineering*, 82(1):35–45, 1960. 10.1115/1.3662552.
- Dae Hung Kang. *An optimized computational environment for real-time hybrid simulation*. PhD thesis, UNIVERSITY OF COLORADO AT BOULDER, 2010.
- M. A. Karkoub and M. Zribi. Active/semi-active suspension control using magnetorheological actuators. *International Journal of Systems Science*, 37:35–44, 2006. ISSN 00207721. doi: 10.1080/00207720500436344.

- URL <http://search.ebscohost.com/login.aspx?direct=true&db=aph&AN=19606959&site=ehost-live>. 1.
- D. Karnopp, M. J. Crosby, and R. A. Harwood. Vibration control using semi-active force generators. *Journal of Engineering for Industry*, 96:619–626, 1974. URL <http://link.aip.org/link/?MSE/96/619/1http://dx.doi.org/10.1115/1.3438373>. 2.
- J. M. Kelly and D. Konstantinidis. *Mechanics of rubber bearings for seismic and vibration isolation*. Wiley, Chichester, West Sussex, U.K.; [Hoboken, N.J.], 2011. ISBN 9781119994015 1119994012.
- C.-P. Lamarche, R. Tremblay, P. Léger, M. Leclerc, and O. S. Bursi. Comparison between real-time dynamic substructuring and shake table testing techniques for nonlinear seismic applications. *Earthquake Engineering & Structural Dynamics*, 39(12):1299–1320, 2010. ISSN 1096-9845. doi: 10.1002/eqe.994. URL <http://dx.doi.org/10.1002/eqe.994>.
- Y. Z. Lin. *Real-time hybrid testing of an MR damper for response reduction*. PhD thesis, University of Connecticut, Storrs, CT, 2009. URL http://www.worldcat.org/title/real-time-hybrid-testing-of-an-mr-damper-for-response-reduction/oclc/436149449&referer=brief_results.
- Y. Z. Lin and R. E. Christenson. Comparison of real-time hybrid testing with shake table tests for an MR damper controlled structure. In *American Control Conference, 2009. ACC '09.*, pages 5228–5233, 2009. doi: 10.1109/ACC.2009.5160643.
- Y. Z. Lin and R. E. Christenson. Real-time hybrid test validation of a MR damper controlled building with shake table tests. *Adv. Struct. Eng. Advances in Structural Engineering*, 14:79–92, 2011. ISSN 1369-4332. 1.

- C. H. Loh, J. P. Lynch, K. C. Lu, Y. Wang, C. M. Chang, P. Y. Lin, and T. H. Yeh. Experimental verification of a wireless sensing and control system for structural control using MR dampers. *Earthquake Engineering & Structural Dynamics*, 36(10):1303–1328, 2007. ISSN 1096-9845. doi: 10.1002/eqe.682. URL <http://dx.doi.org/10.1002/eqe.682>.
- J. P. Lynch, Y. Wang, R. A. Swartz, K. C. Lu, and C. H. Loh. Implementation of a closed-loop structural control system using wireless sensor networks. *Structural Control and Health Monitoring*, 15(4):518–539, 2008.
- MATLAB. *version 7.11.0 (R2011a)*. The MathWorks Inc., Natick, Massachusetts, 2011.
- K. G. McConnell and P. S. Varoto. *Vibration testing: theory and practice*. John Wiley & Sons Seoul, 1995.
- Narutoshi Nakata. Effective force testing using a robust loop shaping controller. *Earthquake Engineering & Structural Dynamics*, 42(2):261–275, 2013. ISSN 1096-9845. doi: 10.1002/eqe.2207. URL <http://dx.doi.org/10.1002/eqe.2207>.
- G. Ou, A. I. Ozdagli, S. J. Dyke, and B. Wu. Robust integrated actuator control: Experimental verification and real time hybrid simulation implementation. *Earthquake Engng Struct. Dyn. (in review)*, 2014.
- A. I. Ozdagli, W. Xi, B. Li, S. J. Dyke, B. Wu, and J. Zhang. Actual hammer test on 3dof structure after structural modification. *Network for Earthquake Engineering Simulation*, 2013a. doi: 10.4231/D3QZ22H32. URL <http://nees.org/warehouse/experiment/4485/project/1076>.
- A. I. Ozdagli, W. Xi, B. Li, S. J. Dyke, B. Wu, J. Zhang, and Y. Ding. Preliminary hammer test on 3dof structure after structural *Network for*

- Earthquake Engineering Simulation*, 2013b. doi: 10.4231/D3R785N6W. URL <http://nees.org/warehouse/experiment/4217/project/1076>.
- V. Panichacarn. *A Structural Health Monitoring Approach Using ERA, Real Numbered Mode Shape Transformation, and Basis Mode Screening*. ProQuest, 2006.
- R. S. Pappa. *Eigensystem realization algorithm user's guide for VAX/VMS computers: Version 931216*. National Aeronautics and Space Administration, Langley Research Center, Hampton, VA, 1994.
- B. Phillips and B. F. Spencer. Model-based feedforward-feedback actuator control for real-time hybrid simulation. *Journal of Structural Engineering*, 139(7):1205–1214, 2013. doi: 10.1061/(ASCE)ST.1943-541X.0000606. URL <http://ascelibrary.org/doi/abs/10.1061/%28ASCE%29ST.1943-541X.0000606>.
- J. C. Ramallo, E. A. Johnson, and Spencer B. F. Smart base isolation systems. *Journal of Engineering Mechanics*, 128(10):1088–1099, 2002.
- I. Sahin, T. Engin, and S. Cesmeci. Comparison of some existing parametric models for magnetorheological fluid dampers. *Smart Materials and Structures*, 19(3):035012, 2010. URL <http://stacks.iop.org/0964-1726/19/i=3/a=035012>.
- V. Saouma, G. Haussmann, D. Kang, and W. Ghannoum. Real-time hybrid simulation of a nonductile reinforced concrete frame. *Journal of Structural Engineering*, 140(2):04013059, 2014. doi: 10.1061/(ASCE)ST.1943-541X.0000813. URL [http://dx.doi.org/10.1061/\(ASCE\)ST.1943-541X.0000813](http://dx.doi.org/10.1061/(ASCE)ST.1943-541X.0000813).
- X. Shao and G. Enyart. Development of a versatile hybrid testing system for seismic experimentation. *Experimental Techniques*, pages no–no, 2012. ISSN

- 1747-1567. doi: 10.1111/j.1747-1567.2012.00837.x. URL <http://dx.doi.org/10.1111/j.1747-1567.2012.00837.x>.
- T. T. Soong and B. F. Spencer. Supplemental energy dissipation: state-of-the-art and state-of-the-practice. *Engineering Structures*, 24:243–259, 2002. ISSN 0141-0296. doi: 10.1016/s0141-0296(01)00092-x. URL <http://www.sciencedirect.com/science/article/pii/S014102960100092X>. 3.
- B. F. Spencer and S. Nagarajaiah. State of the art of structural control. *Journal of Structural Engineering*, 129:845–856, 2003. URL [http://dx.doi.org/10.1061/\(ASCE\)0733-9445\(2003\)129:7\(845\)](http://dx.doi.org/10.1061/(ASCE)0733-9445(2003)129:7(845)). 7.
- B. F. Spencer, S. J. Dyke, M. K. Sain, and J. D. Carlson. Phenomenological model for magnetorheological dampers. *Journal of Engineering Mechanics*, 123:230–238, 1997. URL [http://link.aip.org/link/?QEM/123/230/1http://dx.doi.org/10.1061/\(ASCE\)0733-9399\(1997\)123:3\(230\)](http://link.aip.org/link/?QEM/123/230/1http://dx.doi.org/10.1061/(ASCE)0733-9399(1997)123:3(230)). 3.
- Andrew Taylor, David Swanson, Mark Pierepiekarz, Yao Cui, Paul Brallier, Tom Xia, King Chin, Greg Hess, Jonathan Siu, Doug Lindquist, and Erik Bishop. Implications of the great east japan earthquake for the pacific northwest region of the united states. In *Proceedings of the International Symposium on Engineering Lessons Learned from the 2011 Great East Japan Earthquake*, March 2012.
- M. W. Trethewey and J. A. Cafeo. Tutorial: signal processing aspects of structural impact testing. *The International Journal of Analytical and Experimental Modal Analysis*, 7:129–149, 1992. 2.
- United Nations Centre for Regional Development. Report on the 2008 great sichuan earthquake. 2009.
- Q. Wang, J. Wang, J. Feng, F. Chi, and C. Zhang. Real-time dynamic hybrid

- testing for soil–structure interaction analysis. *Soil Dynamics and Earthquake Engineering*, 31(12):1690 – 1702, 2011. ISSN 0267-7261. doi: <http://dx.doi.org/10.1016/j.soildyn.2011.07.004>. URL <http://www.sciencedirect.com/science/article/pii/S0267726111002120>.
- V. Wen. Method for random vibration of hysteretics systems. *Journal of the engineering mechanics division*, 2:249–263, 1976. URL <http://ci.nii.ac.jp/naid/10004543354/en/>.
- J. T. P. Yao. Concept of structural control. *Journal of the Structural Division*, 98:1567–1574, 1972. 7.
- M. F. Zapateiro de la Hoz. *Semiactive control strategies for vibration mitigation in adaptronic structures equipped with magnetorheological dampers*. PhD thesis, Universitat de Girona, 2009. URL <http://www.tesisenxarxa.net/TDX-0811109-130639/>. Gi-976-2009.